國立臺灣大學理學院地理環境資源學系

碩士論文

Department of Geography

College of Science

National Taiwan University

Master's Thesis

台灣西南部淺層活動斷層潛移速率變化：利用 InSAR 與 GNSS 進行分析

Creep Rate Changes of Shallow Active Faults in Southwestern Taiwan: Insights from InSAR and GNSS Analysis

陳立學

Li-Shiue Chen

指導教授：莊昀叡 博士

Advisor: Ray Y. Chuang, Ph.D.

中華民國 114 年 1 月

January, 2025

doi: 10.6342/NTU202500538

doi: 10.6342/NTU202500538

國立臺灣大學碩士學位論文
口試委員會審定書
MASTER'S THESIS ACCEPTANCE CERTIFICATE
NATIONAL TAIWAN UNIVERSITY

台灣西南部淺層活動斷層潛移速率變化：利用 InSAR 與 GNSS 進行分析

Creep Rate Changes of Shallow Active Faults in Southwestern Taiwan:

Insights from InSAR and GNSS Analysis

本論文係 陳立學 （學號）在國立臺灣大學地理環境資源學系(系/所/學位學程)完成之碩士學位論文，於民國 114 年 01 月 14 日承下列考試委員審查通過及口試及格，特此證明。

The undersigned, appointed by the Department/ Institute of Geography on 14 (date) 01 (month) 2025 (year) have examined a Master's thesis entitled above presented by Lishiue (name) R11228030 (student ID) candidate and hereby certify that it is worthy of acceptance.

口試委員 Oral examination committee:

莊昀叡　　姜國輝　　張午龍

（指導教授 Advisor）

林朝億

系主任/所長 Director:

doi: 10.6342/NTU202500538

摘要

活動構造在地震周期中透過潛移釋放應力，其變形速率可能會因為地震觸發或泥貫入體的活動而有所改變。這樣的潛移斷層可能對基礎建設造成破壞，也會影響區域地震災害潛勢的評估。台灣西南部位於歐亞板塊和菲律賓海板塊之間的碰撞帶造山前緣，構造活動頻繁，對包括台南與高雄在內的數百萬居民構成威脅。該地區擁有眾多活動斷層，其中有些在 2010 年 Mw 6.3 的甲仙地震和 2016 年 Mw 6.4 的美濃地震中受到了顯著影響。這些地震觸發了一些先前未充分瞭解的淺層構造活動，分析這些構造在不同時期的滑移速率是一個相當重要的研究課題。

合成孔徑雷達干涉測量技術（InSAR）具有高空間解析度的優勢，近年來在測地領域中相當具有影響力。在本研究中，我使用 ALOS 與 ALOS-2 兩組 L 波段合成孔徑雷達衛星影像，產製台灣西南部的地表變形速度場，這些波長較長的雷達影像即使在植被茂密的台灣南部丘陵地區也能得到良好的成果。本研究建立了 2007-2010 年和 2015-2022 年兩個時段的地表間震變形速度場，以及 2016 美濃地震的同震地表變形場，這些結果都與連續 GNSS 測站的觀察成果有良好的相關性。

研究結果顯示，在新化斷層與屏東平原之間存在 15 條具有顯著變形量差異的速率邊界，其中部分與後甲里斷層、小崗山斷層、右昌斷層、龍船背斜等前人熟知的淺部活動構造相符；此外，還在過去研究較少涉及的區域發現了一些新的線狀構造，顯示台灣西南部的淺層活動構造仍有許多尚未充分瞭解之處。透過 InSAR 和水準測量資料的剖面分析，本研究成功辨識出一些構造在不同的觀測時間段內潛移速率有明顯變化，本研究取得的成果不僅有助於評估台灣西南部的地震災害潛勢，還為研究活動構造在地震週期中的潛移變形現象提供了重要線索，突顯了持續監測與深入研究的必要性。

關鍵詞：斷層潛移、合成孔徑雷達、活動構造、斷層、台灣西南部

doi: 10.6342/NTU202500538

Abstract

The creeping behavior of active faults play a critical role in stress release during the seismic cycle, with their deformation rates potentially influenced by earthquake triggering or the activity of mud diapir. Such creeping faults not only pose a risk to infrastructure but also significantly impact the assessment of regional seismic hazard potential. Southwestern Taiwan is located at the orogenic front formed by the arc-continent collision between the Eurasian Plate and the Philippine Sea Plate, many active structures in this area pose significant threats to the lives and property of millions of residents in Tainan and Kaohsiung. Two large earthquakes, the 2010 Mw 6.3 Jiashian earthquake, and the 2016 Mw 6.4 Meinong earthquake, occurred in Southwestern Taiwan. These earthquakes triggered shallow fault activity and some of them was not well understood in the previous studies. One important question is how surface deformation changes in response to the earthquakes during the interseismic period.

Recently, the Interferometric Synthetic Aperture Radar (InSAR) technique has become a more influential geodetic method for accessing high spatial resolution deformation patterns. In this study, I used L-band SAR images from the ALOS and ALOS-2 satellites to generate ground deformation velocity fields for Southwestern Taiwan. The longer wavelength of these radar images enabled effective monitoring even in the densely vegetated hill regions of southern Taiwan. I constructed interseismic surface deformation velocity fields for the periods of 2007-2010 and 2015-2022, as well as coseismic deformation fields for the 2016 Meinong earthquake, all of which showed strong correlation with continuous GNSS station data.

The results revealed 15 velocity boundaries with clear deformation gradient in the region between the Hsinhua Fault and the Pingtung Plain. Some of which correspond to previously known shallow active structures such as the Houchiali Fault, Hsiaokangshan

doi: 10.6342/NTU202500538

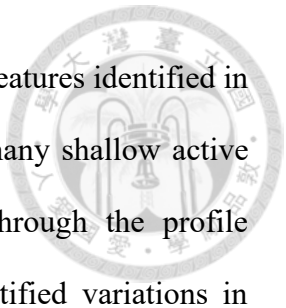

Fault, Youchang Fault, and Lungchuan Anticline, while other linear features identified in regions with less addressed in previous studies, highlighting that many shallow active structures in Southwestern Taiwan remain poorly understood. Through the profile analysis of InSAR and leveling data, this study successfully identified variations in interseismic slip rates across different time periods. The findings not only contribute to the assessment of seismic hazard potential in Southwestern Taiwan, but also provide critical insights into the creeping behavior of active structures throughout the seismic cycle, emphasizing the need for continuous monitoring and further investigation.

Key words: fault creep, synthetic aperture radar, active structure, fault, Southwestern Taiwan

doi: 10.6342/NTU202500538

致謝

謹此向指導教授莊昀叡老師表達誠摯的感謝，感謝老師在研究過程中的悉心指導，讓本研究得以順利完成；也感謝口試委員張午龍老師、景國恩老師、林玉儂老師的寶貴建議，使論文內容更加嚴謹與完善。在此也特別感謝徐澔德老師、葉恩肇老師、王昱老師、盧志恆老師對本研究提供的指導與建議，使論文內容更加充實。

本研究受到 NSTC（計畫編號 110-2116-M-002-009、112-2119-M-008-009、112-2811-M-002-123）、GSMMA（計畫編號 B113011）、及 JAXA（計畫編號 EO-RA3）的支持。也感謝 ISCE、Mintpy 等開源程式協助衛星影像處理，Matlab 與 QGIS 等軟體在數據分析與視覺化方面的應用，以及 ChatGPT 在程式撰寫與論文寫作過程中的輔助。

本研究的階段性成果曾於 2023 年台日地殼變形研討會（JTWCD6）、2024 年中華民國地球物理學會與中華民國地質學會 112 年年會暨學術研討會、2024 年地理學年會、及 2024 年台日紐地震災害研討會（The 2024 Japan-New Zealand-Taiwan Seismic Hazard Workshop）中發表，並在各種場合獲得寶貴的回饋與建議。依照學術慣例，本研究的成果也預計發表於國際期刊。

台大理學院每年有三百多篇碩士論文發表，今年我有幸成為其中一份子，為人類科學發展盡一份心力。在上國小之前，我就在聖誕樹的許願卡上寫了想成為科學家，如今碩士畢業，也算在這條路上踏出第一步。能在最感興趣的地球科學領域持續精進，最首先要感謝家人的無條件支持；而莊昀叡老師這幾年所提供的研究資源與寶貴指導，不僅拓展了我的學術視野，也深刻影響了我的生涯規劃。完成論文的過程比想像中還要充滿挑戰，感謝耕霈、荃敏、勝煒、昭蓉、Neha、子昕、靜儀、友維、豐傑、劭方、耀萱、聿修、佑璇、奕婷、心瑜、冠至、李旻、正標、皓媜、棋浚、立昀等同學的陪伴，度過在研究室的一千兩百多個日子。

doi: 10.6342/NTU202500538

List of Contents

doi: 10.6342/NTU202500538

doi: 10.6342/NTU202500538

doi: 10.6342/NTU202500538

List of Figures

doi: 10.6342/NTU202500538

doi: 10.6342/NTU202500538

doi: 10.6342/NTU202500538

doi: 10.6342/NTU202500538

Chapter 1 Introduction

1.1. Motivation

Interseismic creep is the key for understanding fault behavior throughout a seismic cycle (e.g., Thatcher, 1983; Scholz, 1998; Harris, 2017). Advances in geodetic and data analysis techniques have recently enabled the detection of various deformation events across diverse tectonic boundaries, such as post-seismic deformation, slow slip events, and pre-seismic transient deformation (e.g. Dragert et al., 2001; Thomas et al., 2014; Nishimura et al., 2023). These processes not only influence earthquake recurrence but also impact the stability of critical infrastructure. For instance, interseismic creep along shallow active structures can lead to ground displacement that threatens railways, tunnels, and urban developments (e.g. Lu et al., 2025). Unlike abrupt seismic events, interseismic creeping often occurs over longer timescales and is challenging to detect without advanced observational techniques. Insights gained from studying these events enhance our understanding of active fault mechanics and contribute to geohazard assessment.

Numerous studies worldwide have documented interseismic creep deformation events using geodetic techniques, with some of the most notable examples highlighted in the map shown in Figure 01. For example, along the Haiyuan Fault in China, geodetic observations have revealed shallow fault creep with varying rates, providing insights into strain accumulation and release mechanisms (Zhang et al., 2024). Similarly, the North Anatolian Fault in Turkey exhibits episodic aseismic slip events detected through InSAR, which is controversial to the prior assumptions about steady fault behavior (Rousset et al., 2016). In Noto Peninsula, Japan, GNSS stations captured transient deformation driven by deep fluid migration and aseismic slip, which lead to an ongoing earthquake swarm (Nishimura et al., 2023).

These cases highlight the critical role of geodetic techniques, such as GNSS and

doi: 10.6342/NTU202500538

InSAR, in capturing high temporal and spatial deformation signals. Unlike traditional geological methods that focus on long-term fault behavior, geodetic observations enable the detection of short term deformation events. This capability is especially valuable for identifying young and active structures.

Taiwan, one of the most tectonically active regions in the world, serves as a prime example of the limitations of traditional methods. Figure 02 shows the active fault maps published by the Geological Survey and Mining Management Agency (GSMMA) (Lin et al., 2021) and seismogenic structure models from the Taiwan Earthquake Model (TEM) (Shyu et al., 2016, 2020, 2025) , which primarily rely on traditional geological approaches. These methods, including geomorphic analysis, borehole drilling, and stratigraphic interpretation, have provided valuable insights into fault activity over timescales of thousands to millions of years. However, they are often unable to detect young structures, which may lack significant geomorphic expressions but remain active on human timescales. Recent advances in geodetic techniques, such as GNSS and InSAR, have addressed these gaps. By detecting precise ground deformation, these measurements can

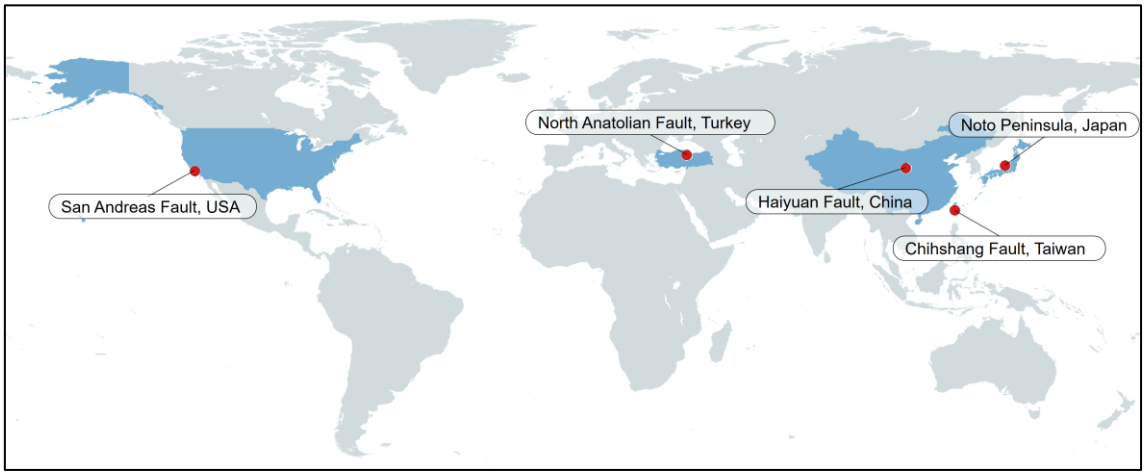

Figure 01. Map showing the locations of classic case studies on interseismic creep events referenced in this study.

doi: 10.6342/NTU202500538

not only reveal young active faults previously undetected by geological methods, but also uncover significant differences between the activity rates of the faults known before on human and geological timescales.

Southwestern Taiwan is home to over six million people and two major cities, Tainan and Kaohsiung, which host numerous historical sites and high-tech industrial parks. As a young accretionary wedge in front of the orogenic belt, this region is believed to be an area of high tectonic activity and rapid structural shortening. Recent geodetic studies have found ground deformation along some structures that differ from traditional geological findings. For example, InSAR detected unusual deformation on the eastern edge of the Tainan Tableland, hinting at previously unknown tectonic activity. Similarly, GPS near the Zhongliao Tunnel recorded unexpected uplift rates that are controversial compared to geological observations. From previous studies using geodetic methods, researchers also

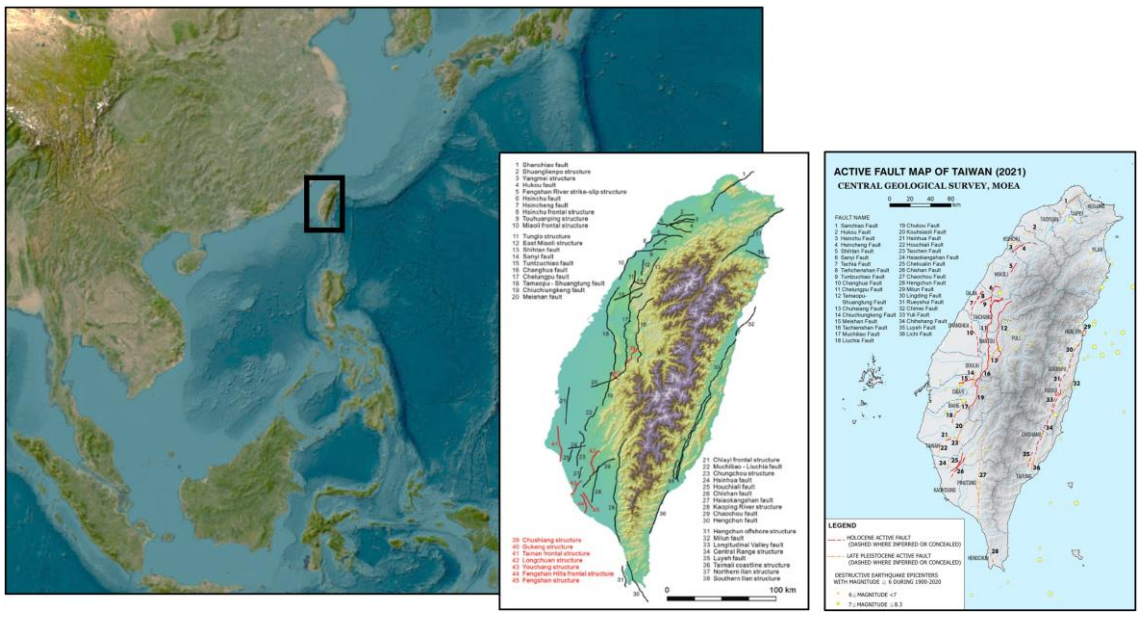

Figure 02. Location of Taiwan in East Asia (left), seismogenic structure map from TEM (Shyu et al., 2020) (middle), and active fault map from GSMMA (Lin et al., 2021) (Right). Basemap retrieved from Esri. "World Imagery" [basemap]. Scale Not Given.

doi: 10.6342/NTU202500538

found that many shallow active structures were altered by the 2010 Jiashian and 2016 Meinong earthquakes. As shown on the maps in Figure 03, GNSS stations can identify different surface deformation trends in this region during different time periods. Notably, some deformation patterns occurred in areas where no structures are mapped on existing active fault maps, suggesting previously undetected fault activity.

This study processes high-resolution deformation data from ALOS and ALOS-2 InSAR, integrated with GNSS and precise leveling measurements, to investigate creeping behavior in Southwestern Taiwan over the past two decades. By focusing on shallow active structures, this research aims to map the spatial distribution and temporal variability of interseismic creep, understanding the role of transient creep in the broader tectonic activity of the region. Furthermore, this study seeks to construct a geodetic-based active fault map for Southwestern Taiwan, providing a valuable resource for understanding deformation mechanisms and informing seismic hazard assessments.

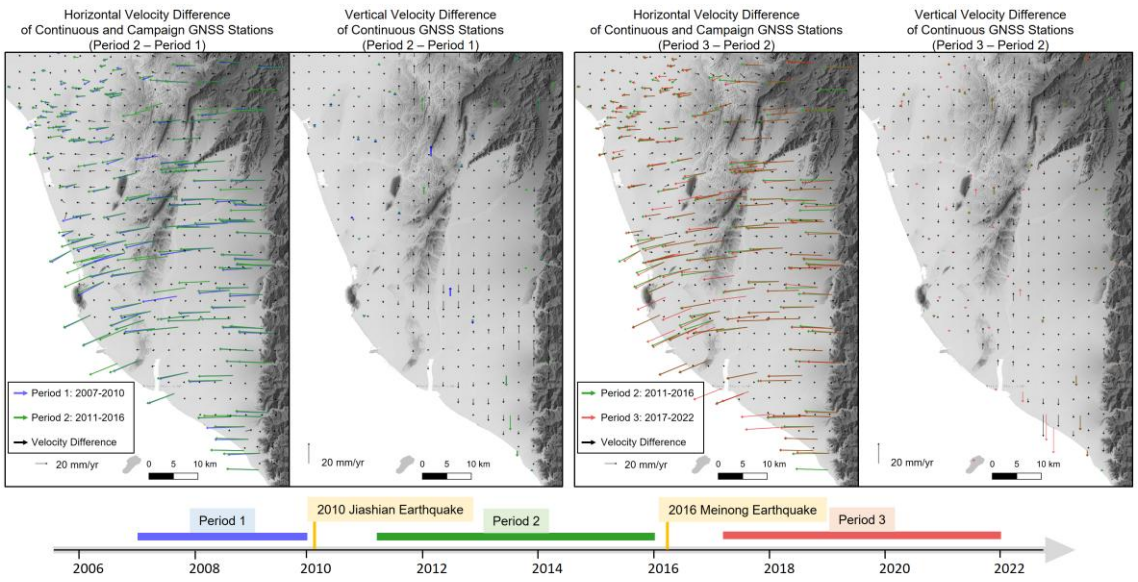

Figure 03. Horizontal (left) and vertical (right) velocity maps of continuous GNSS stations over different periods. Velocity changes stand out in the Tainan Tableland, the Chungchou Anticline, and near Mituo, suggesting potential structural activity.

doi: 10.6342/NTU202500538

1.2. Research Questions

Based on the motivation to better understand shallow creeping faults in Southwestern Taiwan, this research aims to answer the following key questions:

- How has the surface deformation in Southwestern Taiwan evolved over the past two decades, particularly in the periods between the two major earthquakes?
- What are the temporal and spatial characteristics of shallow active structures in Southwestern Taiwan, and how do these characteristics reflect variations in creep rate across different time periods?
- How can the integration of geodetic datasets in this study reshape our understanding of the active fault systems and improve our assessment of seismic hazards associated with these structures in Southwestern Taiwan?

doi: 10.6342/NTU202500538

Chapter 2 Literature Review

In the previous chapter, the importance of studying creeping faults was highlighted. And in Southwestern Taiwan, potential shallow creeping behaviors have been observed. These faults show signs of changing slip rates over the past two decades. To help understand these phenomena, this chapter reviews previous research on the seismic cycle and interseismic deformation, explains the significance of creeping events in Southwestern Taiwan, and explores the increasingly important role of InSAR technology for detecting shallow fault creep.

2.1. Seismic Cycle

The rapid development of crustal deformation observation techniques over the past century has enabled scientists to quantify the surface deformation patterns associated with stress accumulation and release during tectonic processes. The elastic rebound model was introduced in the early stage (Lawson & Reid, 1910), and the concept of the seismic cycle was developed based on theoretical models and geodetic observations (e.g., Thatcher,

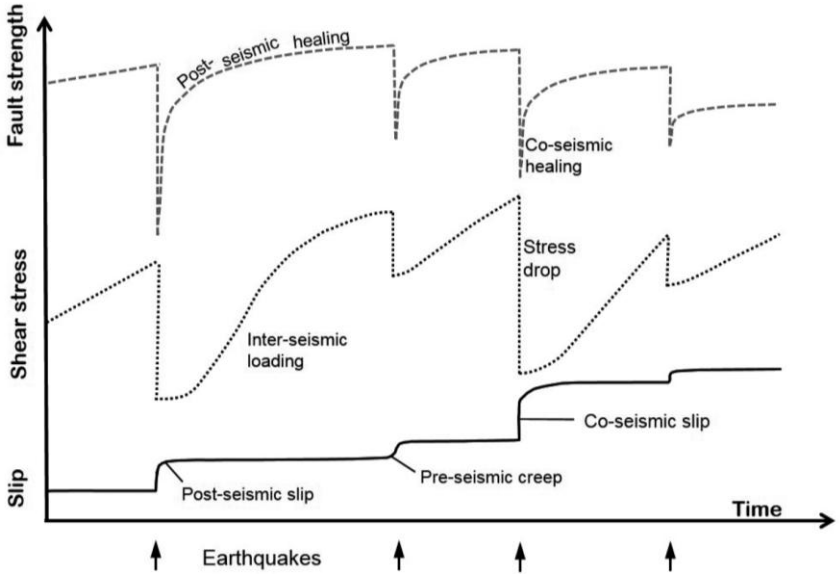

Figure 04. The model of fault slip, shear stress, and fault strength changes by time through the seismic cycles. Figure adapted from Tolomei et al. (2015) and was modified from Di Toro et al. (2012).

doi: 10.6342/NTU202500538

1983; Scholz, 1998; Kaneko et al., 2013). The seismic cycle model describes how stress is repeatedly accumulated and released over timescales ranging from hundreds to thousands of years. These studies deepen our understanding of seismogenic processes and provide a crucial theoretical framework for assessing seismic hazards.

In particular, the seismic cycle model focuses on how stress accumulates during the interseismic phase, how energy is released during coseismic slip, and how postseismic relaxation and slip recovery unfold thereafter. A key component in understanding these processes is the rate-and-state friction law (Dieterich, 1979; Rice, 2001), which explains fault frictional properties and clarifies the conditions that shift fault motion between stable and unstable slip. By combining field observations, geodetic data, and laboratory friction experiments, researchers have simulated fault behavior across various temporal and spatial scales, further clarifying the mechanisms governing earthquake recurrence and deformation (e.g. Wang, 2007; Di Toro et al., 2012). For example, Figure 04 from Di Toro et al. (2012) and Tolomei et al. (2015) illustrates the non-linear evolution of fault strength over time, separating it into distinct stages of fault behavior.

Instead of releasing the accumulated strain through an earthquake rupture, the velocity-strengthening parts of a fault creep seismically or aseismically, while the remaining section of it stays locked during the interseismic stage. The concept of frictional sliding on the pre-existing fault plane was developed by several laboratory experiments (e.g. Dieterich, 1978; Marone et al., 1991; Blanpied et al., 1995) and theoretical models (e.g. Tse & Rice, 1986; Scholz, 1998). Those aseismic patches of a fault contribute to the overall slip budget via steady creep during the interseismic phase (e.g., Murray et al., 2001; Titus et al., 2006), and can also experience transient events, such as post-seismic afterslip (e.g., Barbot et al., 2009; Copley, 2014; Floyd et al., 2016; Perfettini & Avouac, 2004; Zhou et al., 2018) and episodic transient creep (e.g., Murray

doi: 10.6342/NTU202500538

& Langbein, 2006; Rousset et al., 2016). These observations emphasize the complexity of fault behavior and the importance of integrating both seismic and aseismic processes into earthquake-cycle models. Ultimately, this comprehensive approach to studying fault mechanics helps us better understand seismic risks, gives us a clearer picture of how faults slip, and sheds light on how tectonic stress and strain evolve in the Earth's crust.

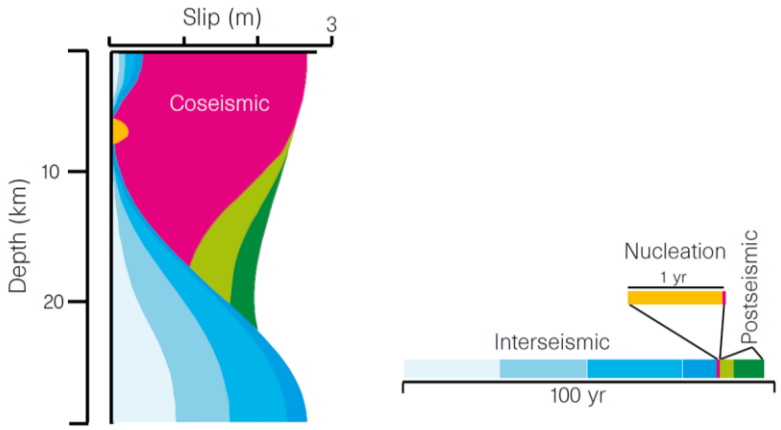

Figure 05. The model of fault slip in the San Andreas Fault in different stage of a seismic cycle. Figure adapted from Scolz (1998) and was modified from Tse & Rice (1986).

2.2. Interseismic Creep and Transient Deformation

Interseismic creep can be relatively steady, transient, or induced by postseismic relaxation. For example, the Chihshang segment of the Longitudinal Valley fault in eastern Taiwan is a zone of shallow interseismic aseismic creep. After the ML 6.4 Chengkung earthquake, this segment experienced significant afterslip, totaling nearly 35 cm over 5 years, while the coseismic slip was negligible (Thomas et al., 2014). Rousset et al. (2016) used X-band COSMO-SkyMed satellite acquisitions for InSAR analysis of the North Anatolian Fault and found that the fault's creeping rate was not stable between June 2013 and May 2014 (Figure 06). During this period, there was a rapid transient aseismic creep event lasting approximately one month. Before this event, no sudden

doi: 10.6342/NTU202500538

increase in shear stress or decrease in normal stress was observed, suggesting that other unknown factors may have contributed to this transient deformation phenomenon.

With a better understanding of transient slip events during the interseismic period, we can gain insight into the slip behavior of active faults which are capable of triggering major earthquakes. For instance, Harris & Segall (1987) used the trilateration network to estimate the interseismic slip rate of the southern part of the San Andreas fault near Parkfield, California, where a major earthquake happened in 1966. They reported that from 1966 to 1987, there existed a region characterized by a low slip rate, corresponding to the inferred rupture area of the 1966 earthquake. Murray and Segall (2002) utilized the trilateration network and the GPS measurements to calculate the interseismic slip distribution between 1966 and 1998 and reported that the strain released in the 1966 earthquake might have recovered by the interseismic slip deficit. To accurately assess the seismic hazards posed by active structures in a region, understanding transient creep events is indispensable.

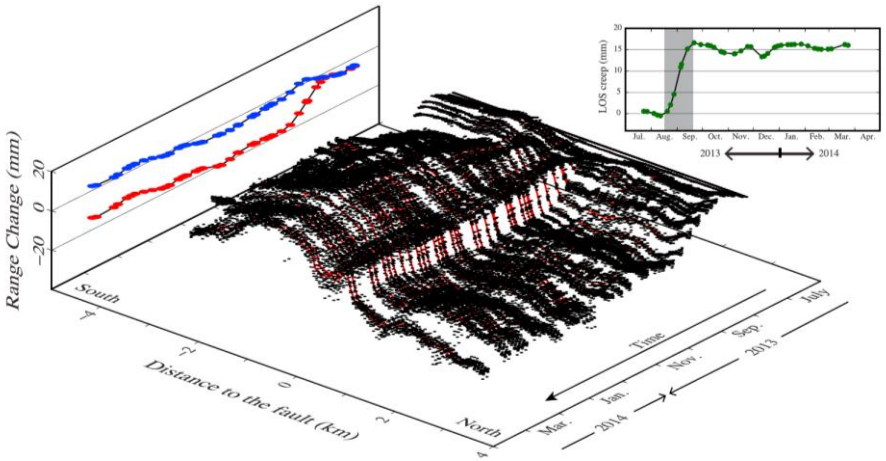

Figure 06. The plot from Rousset et al. (2016) shows surface displacement over time across a fault from July 2013 to April 2014. Blue (south) and red (north) dots represent displacement on each side of the fault, with the inset showing the difference between the two. The gray area highlights a period of transient creep from August to September 2013.

doi: 10.6342/NTU202500538

Many studies based on geodetic data have revealed changes in surface deformation trends over different periods in Southwestern Taiwan. For instance, previous InSAR research found significant variations in the creeping rate of the Houchiali Fault on the eastern side of the Tainan Tableland between 1996–1999 and 2005–2008 (Huang et al., 2006, 2009, 2016). In addition, integrating multiple geodetic datasets has shown changes in the deformation rates of the Tainan Tableland, Lungchuan Anticline, and Pitou Fault before and after the 2010 Jiashian and the 2016 Meinong earthquakes (See Figure 07) (Huang et al., 2013; Le Béon et al., 2017; Yang, 2024). These findings suggest that the shallow active structures in Southwestern Taiwan may exhibit different interseismic creep trends at different times, making this region an ideal case study for exploring creeping behavior in active structures.

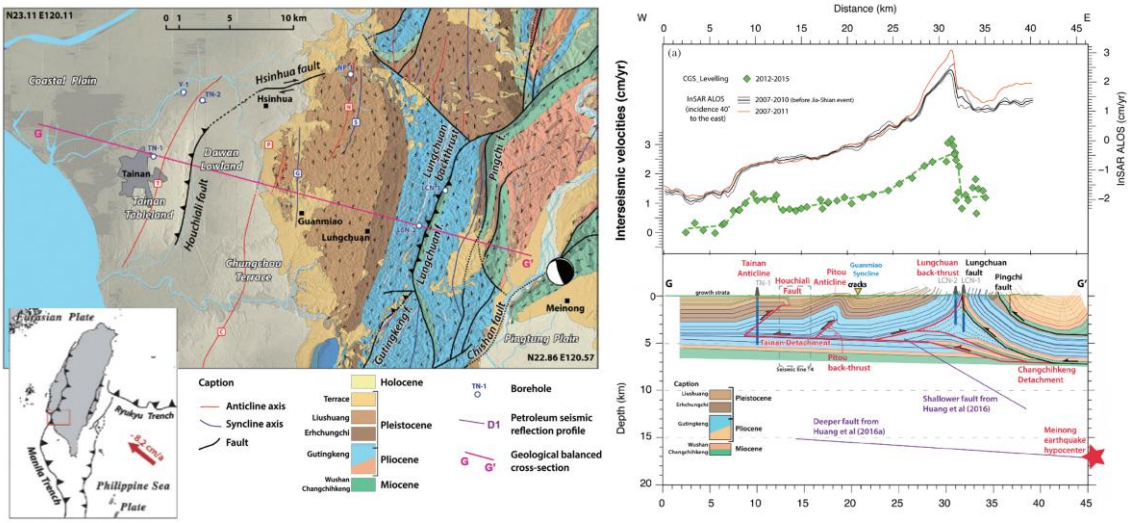

Figure 07. The profile from Le Béon et al. (2017) combines InSAR Line-of-Sight (LOS) velocities (2007–2011) with vertical leveling velocities (2012–2015), highlighting distinct creeping behaviors of the Houchiali Fault and Pitou Anticline during different time periods.

doi: 10.6342/NTU202500538

2.3. Multi-Temporal InSAR

2.3.1. Synthetic Aperture Radar

The SAR system is a type of satellite-borne active radar system, collecting both amplitude and phase information of each image pixels coherently. For a space-born radar system, the resolution on azimuth direction is limited by the size of the antenna. By combining the image data recorded by a continuous segment of the satellite orbit, SAR systems can construct a virtual antenna with a size of hundreds meters, forming a satellite image with high azimuth resolution. Radar systems using this technique are called Synthetic Aperture Radar systems. Conventional SAR systems actively emit the radiation with a wavelength of several tens centimeters, which can penetrate cloud and water vapor. So the SAR images can avoid most of the influence from weather and sunlight conditions.

Several SAR satellites with available acquisitions in Southwestern Taiwan, including those from the European Space Agency (ESA) such as ERS, Envisat, and Sentinel-1, as well as satellites from the Japan Aerospace Exploration Agency (JAXA) like ALOS and ALOS-2. The former 3 satellites employ C-band radar waves with a wavelength ranging from 37-75 mm, while the latter 2 satellites employ L-band radar with a longer wavelength ranging from 200-600 mm. The C-band radar is more sensitive to the ground deformation and is less influenced by the signal delay caused by the ionosphere. On the other hand, the longer wavelengths of L-band radar can provide more reliable signal in densely vegetated regions. However, mitigating ionospheric disruptions for L-band radar images poses a significant challenge.

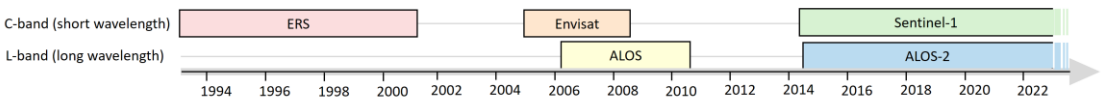

Figure 08. The time span of the major SAR satellites that captured imagery of Taiwan.

doi: 10.6342/NTU202500538

2.3.2. Differential SAR Interferometry

The concept of SAR interferometry was first reported by Graham (1974). The phase differences recorded in the interferogram include information on topography, orbit geometry, ground deformation, atmospheric delay, and other random noises. By combining the information from interferogram phases, topography, and orbit geometry, the ground displacement component in the satellite line-of-sight (hereafter LOS) direction can be extracted. This technique is known as differential SAR interferometry (DInSAR).

DInSAR was first used to observe tectonic activity during the 1992 Landers earthquake (Massonnet et al., 1993), marking an important milestone in geodetic research. However, the technique became more widely used and improved significantly after the European Space Agency (ESA) launched the free Sentinel-1 satellite. With its short revisit interval and easy access to data, Sentinel-1 made InSAR processing more precise and efficient, leading to major advancements in monitoring ground deformation. However, the capability of single-pair DInSAR commonly face limitations such as atmospheric delays, temporal decorrelation, and noise, all of which can degrade measurement accuracy, particularly in regions with vegetation or complex atmospheric conditions.

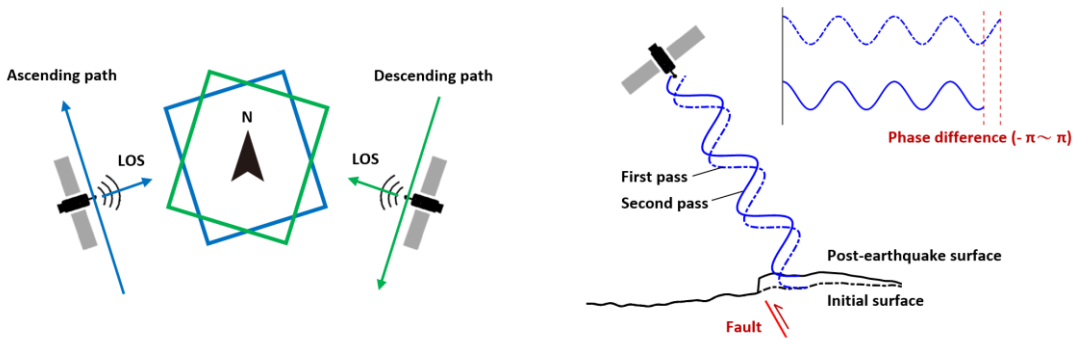

Figure 09. Principles of the InSAR technique. The figure on the left illustrates how variations in radar path can result in distinct image geometries. The figure on the right demonstrates how SAR imagery can detect ground displacement along the LOS by comparing images captured from two separate passes.

doi: 10.6342/NTU202500538

To mitigate these constraints, the Multi-Temporal InSAR (MT-InSAR) approach was developed to exploit multiple SAR images acquired over the same area at various dates (Ferretti et al., 2001; Berardino et al., 2002; Hooper, 2007). For a SAR interferogram, the temporal gap between the reference and secondary image is called the “temporal baseline”, while the spatial distance of the radar antenna is called the “spatial baseline”. By forming a network of interferograms with controlled temporal and spatial baselines, MT-InSAR algorithms average out atmospheric artifacts, improve phase stability, and allow for the reconstruction of displacement time series. These techniques are capable of revealing long-term deformation trends and subtle surface displacements that might otherwise be concealed by noise.

Among the most established MT-InSAR methods, the Persistent Scatterers InSAR (PS-InSAR) technique (Ferretti et al., 2001; Hooper et al., 2004) constructs a single-reference interferogram network and identifies stable scatterers based on their consistently coherent phase signatures, making it particularly suitable for urban or built-up environments. Meanwhile, the Small Baseline Subset (SBAS) InSAR technique (Berardino et al., 2002) connects SAR images with small temporal and spatial baselines to reduce decorrelation, and can perform effectively in terrains with moderate vegetation or more complex topographic conditions.

These MT-InSAR techniques have been proven successful in multiple geodetic research domains, such as the evolution patterns of volcano activities (e.g. Tizzani et al., 2007), land subsidence (e.g. Yan et al., 2012), and active faults (e.g. Bürgmann et al. 2006). The ability of MT-InSAR in capturing long-term deformation patterns allows further applications on hazard assessment, infrastructure management, and scientific research.

doi: 10.6342/NTU202500538

2.4. MT-InSAR in Southwestern Taiwan

Many studies have tried to use multiple SAR acquisitions to solve the ground displacement field of Southwestern Taiwan. Multiple early researches focus on the active structures near the Tainan Tableland by using C-band ERS and Envisat images (e.g. Figure 10) (Fruneau et al., 2001; Tung, 2008; Huang et al., 2009; Lin, 2012; Wu et al., 2013). Huang et al. (2009) used 6 acquisitions from ERS satellites between 1996 and 2000 to construct multiple DInSAR results, solving the deformation pattern of the nearby Tainan fault, Houchiali fault, and Chungchou fault. Lin (2012) used the PS-InSAR algorithm to derive the deformation time series from 52 acquisitions from ERS between 1993 and 2000, as well as 21 acquisitions from Envisat between 2005 and 2008. The study by Lin (2012) revealed that the 1999 ML 7.3 Chi-Chi earthquake did not exhibit a significant impact based on the ERS results. However, the deformation pattern near Tainan Tableland changed in the 2005-2008 Envisat dataset, indicated some mechanisms that have not been clearly understood yet influenced the active structures here.

Following works use MT-InSAR to cover a larger region. Huang et al (2016) utilized ERS and Envisat SAR images to construct the deformation map of the coastal plain of Western Taiwan and Southwestern Taiwan from 1995 to 2008, documented the land subsidence and seasonal deformation patterns. Chao (2016) and Tsukahara & Takada (2018) used L-band ALOS acquisitions to get the displacement time series from 2007 to 2011, reported the deformation pattern near Tainan City and Fengshan Fault, repectively. Franklin & Huang (2022) utilized more than 300 acquisitions from both ascending track and descending track of Sentinel-1 between 2016 and 2021 to construct the 3 dimensional surface deformation pattern of the whole Taiwan Island. By combining the dataset from InSAR and GNSS, they constructed a strain rate map which emphasized the main active structures in Taiwan.

doi: 10.6342/NTU202500538

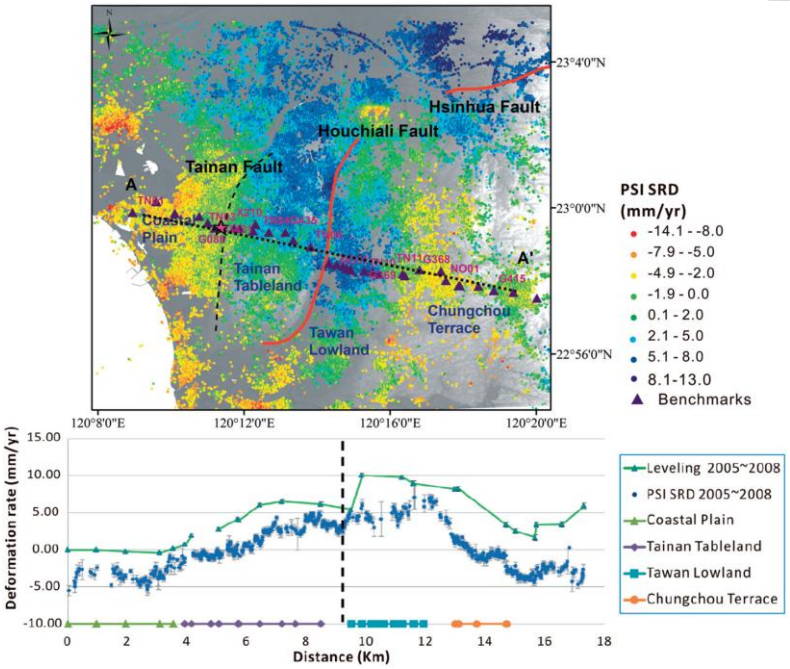

Figure 10. Using Envisat SAR images and leveling data from 2005-2008, Wu et al. (2013) obtained the velocity profile across the Tainan Tableland.

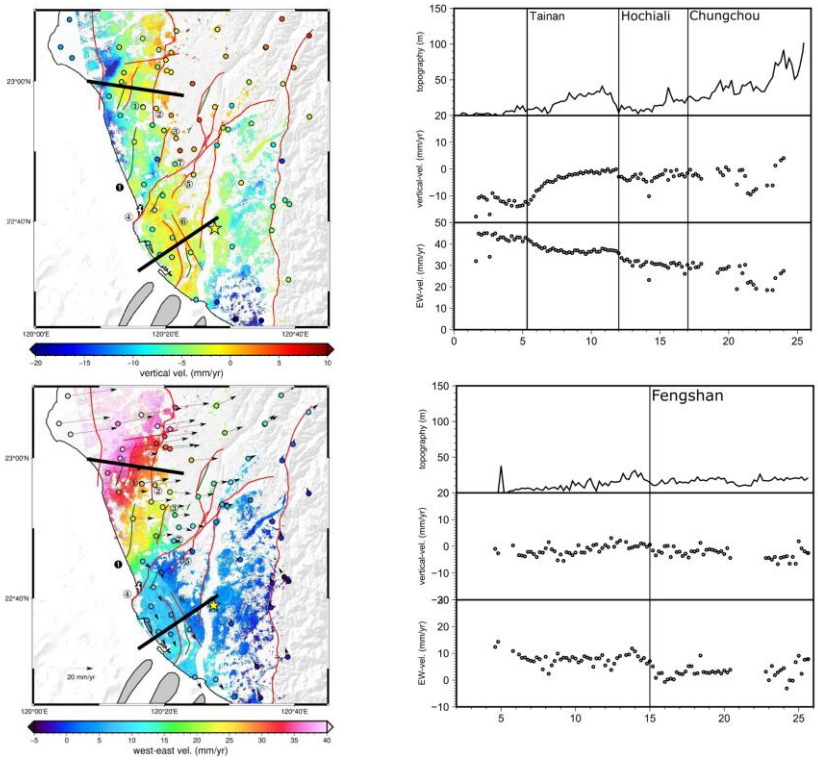

Figure 11. Chen (2021) used both ascending and descending SAR images captured by Sentinel-1 from 2018 to 2021 to construct the 3D velocity field in Southwestern Taiwan.

doi: 10.6342/NTU202500538

Recent studies have further refined MT-InSAR applications in the region. Chen (2021) used ascending and descending tracks of Sentinel-1 from 2018 to 2021 to separate the vertical and east-west deformation components in Southwestern Taiwan, revealing that shallow active structures exhibit different creeping behaviors in vertical and horizontal profiles (Figure 11).

Similarly, Jiang (2024) utilized Sentinel-1 ascending and descending images from March 2016 to November 2021 to construct vertical and east-west velocity maps for the region (Figure 12). By focusing on deformation along the Taiwan High-Speed Rail (THSR) and Taiwan Railway (TR), this study highlighted the significant threats posed by the shallow creeping of active faults to critical infrastructure.

Lee (2024) integrated descending SAR images from ERS (1995–1999), Envisat (2006–2008), and Sentinel-1 (2014–2023) to analyze the spatiotemporal variations of land subsidence in the coastal regions over the past three decades, documenting the compounded risks of land subsidence and sea level rise (Figure 13).

doi: 10.6342/NTU202500538

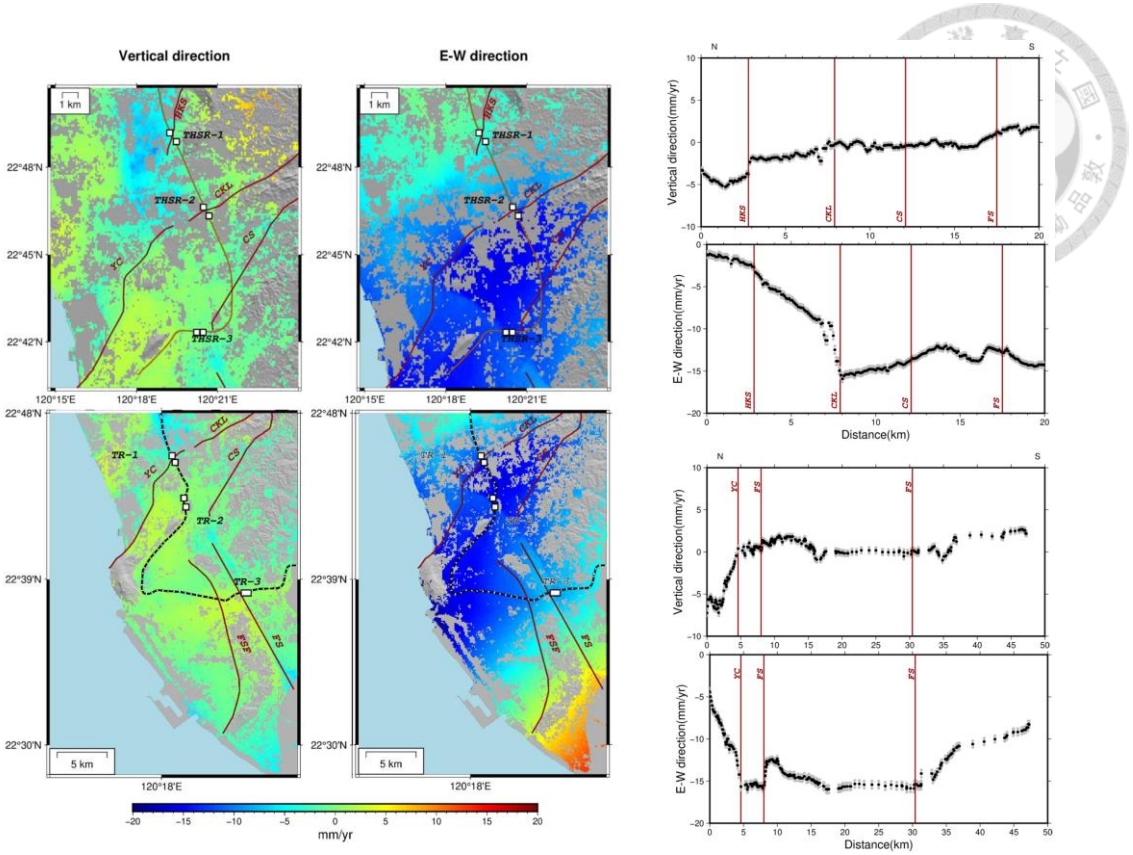

Figure 12. Vertical and east-west velocity field in Southwestern Taiwan, derived from Sentinel-1 SAR images taken between 2016 and 2021, along with velocity profiles of the THSR and TR Railways (Jiang, 2024).

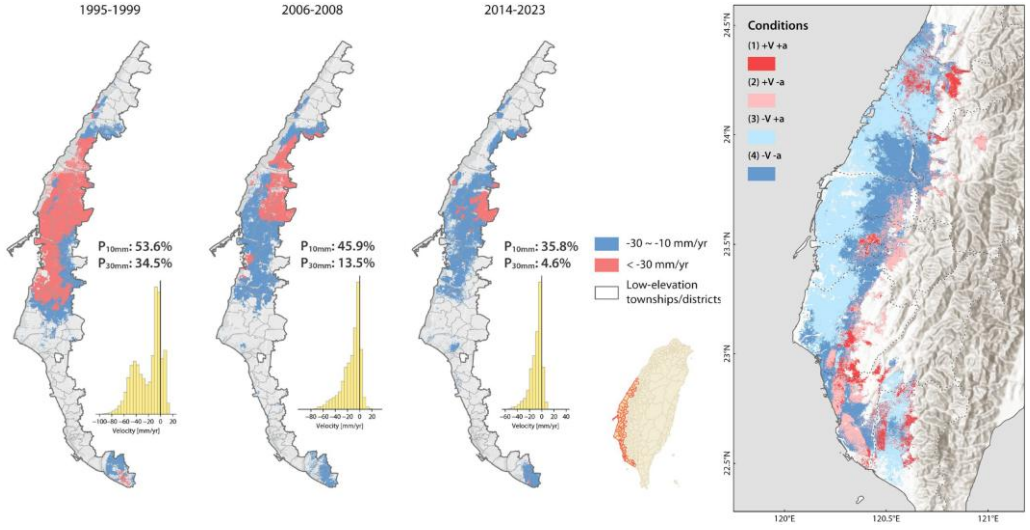

Figure 13. Lee (2024) calculated the spatiotemporal variations of land subsidence during three periods, based on InSAR analysis (left maps). The study integrates vertical velocities and acceleration rates over the past 30 years (right map).

doi: 10.6342/NTU202500538

2.5. Atmospheric Phase Mitigation

Synthetic Aperture Radar (SAR) systems use microwave signals to actively scan the Earth's surface, sending out pulses and analyzing the backscatter signal return from the Earth's surface. However, as these signals pass through the atmosphere, they encounter various disturbances. In the ionosphere, charged particles can cause phase delay, while water vapor, temperature changes, and pressure variations in the troposphere create distortions. These atmospheric effects can reduce the clarity and accuracy of SAR images.

While MT-InSAR techniques can average out phase errors caused by atmospheric delays in individual images, ignoring atmospheric influences can still introduce issues. For instance, seasonal oscillations in atmospheric phases, if overlooked, may be misinterpreted as ground deformation, leading to an overestimation of surface changes in the study area (Jolivet et al., 2014). Refining atmospheric corrections across the entire interferogram network, with careful consideration of seasonal patterns, is essential. By accurately accounting for these atmospheric effects, researchers can achieve more precise measurements of ground movement and surface changes, further enhancing the utility of SAR data.

2.5.1. Ionospheric Phase Delay

When the electromagnet wave signals pass through the ionosphere, they encounter charges particles that cause frequency-dependent delay. The signal delay caused by the ionosphere is inversely proportional to the square of the signal frequency. For example, considering the C-band Sentinel-1 satellite with a wavelength of 0.06 meters and the L-band ALOS-2 satellite with a wavelength of 0.23 meters, the delay experienced by the ALOS-2 image when passing through the same ionospheric disturbance would be approximately 15 times that of Sentinel-1. Therefore, eliminating the ionospheric phase impact is a primary challenge in processing all L-band SAR satellite images.

doi: 10.6342/NTU202500538

To mitigate the effects of ionospheric disturbances, researchers employ either SAR data itself or external ionospheric weather models. Among the methods that leverage SAR data directly, several techniques are prominent, including Faraday rotation-based correction, azimuth offset methods, and the range split-spectrum (RSS) method.

One notable ionospheric correction method is based on Faraday rotation, which occurs when SAR signals pass through magnetic fields in the ionosphere. Faraday rotation affects the polarization state of the SAR signal, causing different polarization modes to experience varying degrees of rotation (e.g. Figure 14). Leveraging this phenomenon, Freeman (2004) developed an algorithm capable of extracting ionospheric phase information from SAR imagery, particularly in L-band and P-band datasets. This method has shown effectiveness in high-latitude regions, where the interaction between the magnetic field and radar signals is more pronounced (e.g., Kim, 2013; Zhu et al., 2017).

The azimuth offset method originated from observations of azimuth streaks in interferograms, a phenomenon caused by Doppler shift and azimuth shift as radar signals traverse unevenly distributed ionospheric electron content. Mattar & Gray (2002) first explored this method for ionospheric estimation, while Raucoules and Michele (2009) refined it by providing a more detailed workflow. Subsequently, Jung et al. (2012) advanced the approach by employing Multiple Aperture Interferometry (MAI) to obtain azimuthal pixel offsets, significantly improving the method's accuracy.

doi: 10.6342/NTU202500538

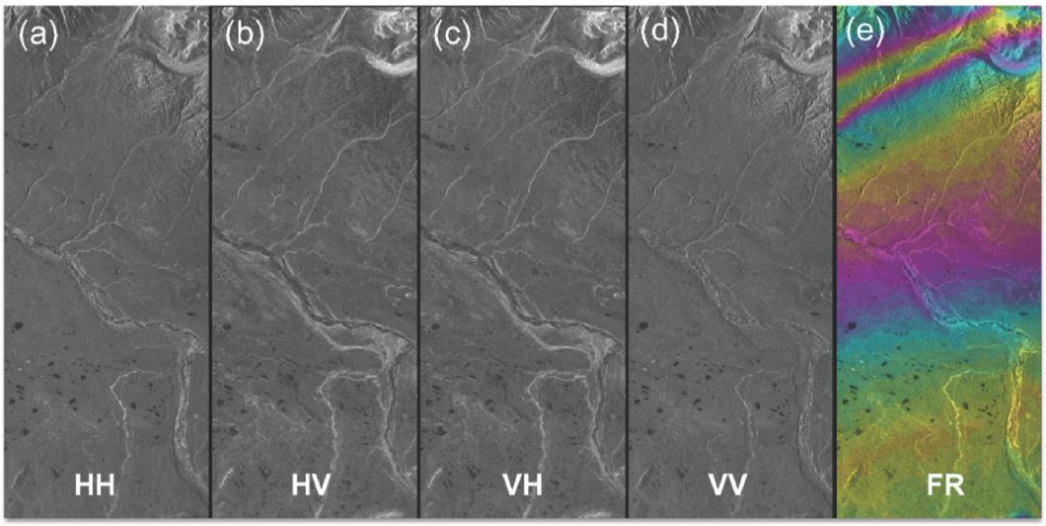

Figure 14. Full-polarization SAR imagery (Zhang et al., 2022). (a-d) Four polarization modes. (e) Ionospheric phase derived from Faraday rotation.

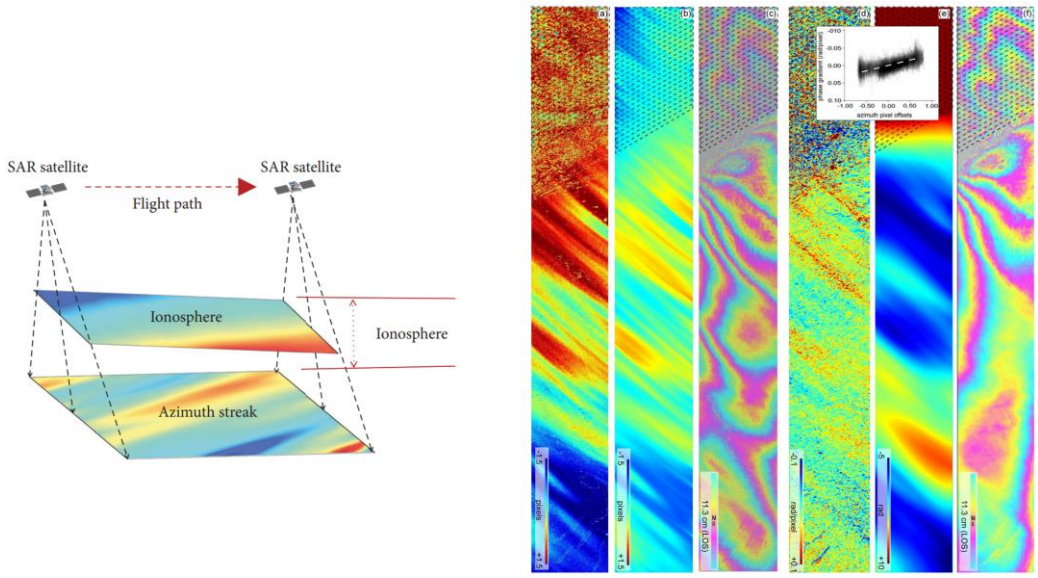

Figure 15. Left: Schematic of ionospheric disturbances causing azimuth streaks in SAR images (Zhu et al., 2017). Right: L-band ALOS DInSAR of the 2008 Wenchuan Earthquake (Raucoules and Michele, 2009). (a) Azimuth offset map showing streaks. (b) Ionospheric contribution after trend removal. (c) Interferogram. (d) Along-orbit phase derivative with streaks. (e) Ionospheric phase screen. (f) Corrected interferogram. The azimuth offset method successfully removes ionospheric delays.

doi: 10.6342/NTU202500538

Both tropospheric and ionospheric effects induced image distortions, but only ionosphere causes signal dispersion due to its frequency-dependent nature. This characteristic allows for the separation of ionospheric contributions from other non-dispersive components, such as topography, surface deformation, and tropospheric effects, through the range split-spectrum (RSS) method. In the RSS approach, the radar signal's bandwidth is divided into high- and low-frequency sub-bands, which are processed independently to generate two interferograms. The dispersive ionospheric phase component is then isolated by solving a linear system of equations based on the differing delays observed in the sub-bands. Gomba et al. (2015) introduced a comprehensive workflow for implementing RSS corrections, which has been adopted by numerous subsequent studies. Recently, the RSS method has become a major ionospheric correction algorithm integrated into many conventional InSAR applications, including SNAP, ISCE, and GMTSAR.

However, RSS faces notable limitations. Narrow-bandwidth systems like ALOS restrict resolution, while noise sensitivity and low interferometric coherence complicate its application (Rosen et al., 2010; Jung et al., 2012; Zhang et al., 2022). Scaling differences between sub-bands can also amplify phase noise or introduce discontinuities in the interferograms (Rosen et al., 2010). Solving for the dispersive term often magnifies noise, necessitating extensive smoothing that may obscure finer details (Rosen et al., 2010). Despite these challenges, the RSS method remains one of the most effective ionospheric correction techniques and is widely applied in modern SAR geodesy.

External GNSS data-based corrections assume ionospheric phase dominates long-wavelength residuals and exhibits spatial smoothness. This method is viable only in regions with a dense and reliable distribution of GNSS stations. Additionally, it often removes other long-wavelength residuals, such as orbital errors and tropospheric phase

doi: 10.6342/NTU202500538

contributions, along with the ionospheric effects. Neely et al. (2019) provided a detailed workflow and error assessment for this approach, naming the method GInSAR, which uses GNSS station velocities to correct ionospheric phase errors. Similarly, Tsukahara & Takada (2018) showed the application of GNSS corrections in L-band SAR data, successfully mitigating ionospheric noise impacts on interferograms.

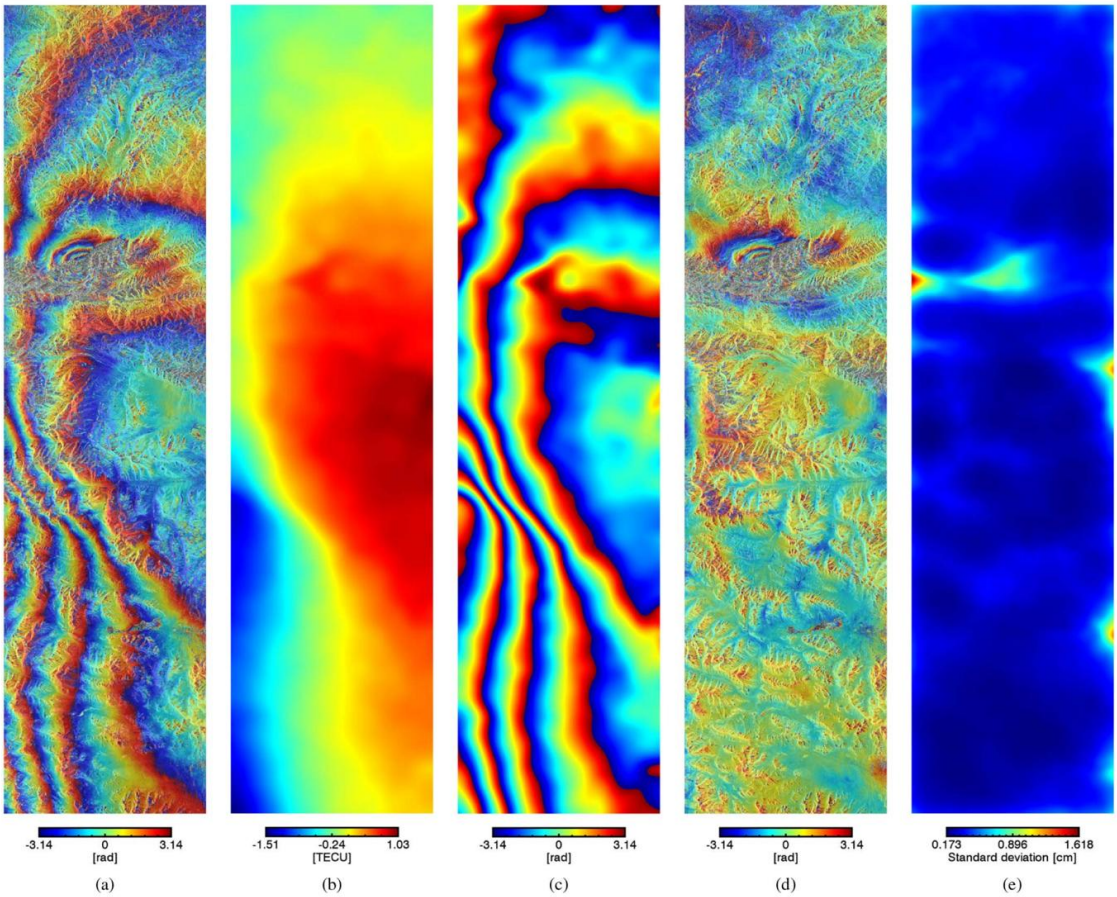

Figure 16. DInSAR results for the 2008 Kyrgyzstan earthquake using the RSS method with L-band ALOS data (Gomba et al., 2015). (a) Raw interferogram. (b) Total electron content (TEC) map. (c) Ionospheric phase delay. (d) Corrected interferogram. (e) Expected accuracy of ionospheric correction.

doi: 10.6342/NTU202500538

2.5.2. Tropospheric Phase Correction

Variations in temperature, pressure, and relative humidity within the troposphere cause electromagnetic waves from SAR systems to refract and delay, introducing phase distortions into SAR imagery. These effects can be corrected using two main approaches: empirical models and numerical weather models.

Empirical models estimate tropospheric delays based on the SAR image itself. For example, the Phase-based method assumed positive correlation between tropospheric phase delays and terrain elevation (Cavalié et al., 2007; Bekaert et al., 2015). While computationally efficient, this method has significant limitations. It assumes delays are dominated by stratified atmospheric signals, neglecting the influence of turbulent components. Additionally, it performs poorly in areas with limited elevation variation and can misinterpret deformation signals as atmospheric delays in regions where topography and deformation are correlated, such as volcanic areas. In such cases, numerical weather models are often more reliable.

Numerical weather models use external atmospheric data to predict and correct tropospheric delays. Widely used examples include ERA5, provided by the European Centre for Medium-Range Weather Forecasts (ECMWF) (Hersbach et al., 2020), and GACOS, developed by Yu et al. (2018). These models integrate atmospheric parameters such as temperature, pressure, and humidity to produce precise delay estimates. Their accuracy relies on the availability of external atmospheric data, which can sometimes be limited.

doi: 10.6342/NTU202500538

Name	Resolution	Period	Coverage
ERA-5 HRES ECMWF (GACOS)	0.25°, 37 pressure levels, 6 h 0.125°, 37 pressure levels 6 h	1989-date	Global
NCEP NARR	0.3°, 29 pressure levels, 3 h	1979-date	USA
MSM	5 km, 50 pressure levels 3 h	2001 to date	Japan
MERRA-2 NASA	0.5°,42 pressure levels, 6 h	1979-date	Global
WRF	Dependent on model parametrization		Global

Figure 17. Basic information on common numerical weather models for tropospheric phase correction (Kirui et al., 2021).

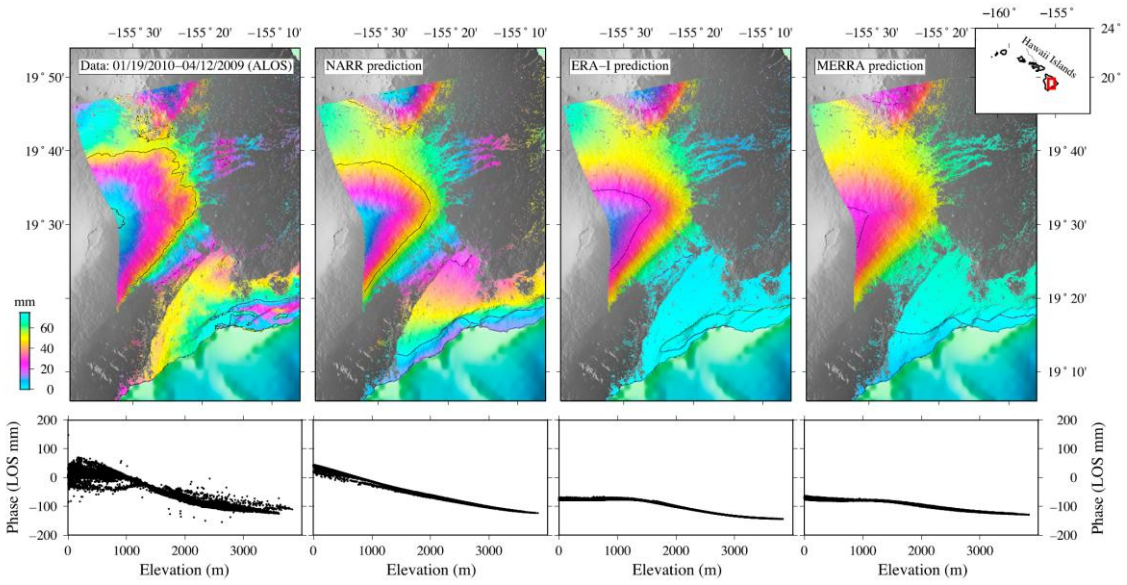

Figure 18. Tropospheric phase correction using different numerical weather models on Kilauea volcano, Hawaii. Figure adapted from Jolivet et al. (2014). The models can separate tropospheric phase and ground deformation from topography-related signals, which is difficult for empirical methods.

doi: 10.6342/NTU202500538

Chapter 3 Study Region

3.1. Tectonic Background of Southwestern Taiwan

Taiwan is situated at the convergent boundary between the Eurasian Plate and the Philippine Sea Plate. The tectonic environment is dominated by the oblique collision of these two plates, where the Eurasian Plate subducting beneath the Philippine Sea Plate. As the result, the southern part of Taiwan represents a relatively young orogenic stage, and the compression resulting from plate convergence significantly influences the structural activities in this region (Suppe, 1984; Huang et al., 1997). The southern foothill and the southern plain of Taiwan belong to the accretionary wedge in front of the orogenic belt, with a complex tectonic setting and considerable surface deformation activity (Pelletier and Stephan, 1986; Angelier et al., 1986).

Multiple active faults or structures had been defined in Southwestern Taiwan (Lin et al., 2021; Shyu et al., 2025), and the deformation of most of them is likely controlled by both the detachment at the basement and the active structures developed above it (Davis et al., 1983; Hung et al., 1999; Carena et al., 2002). Through geodetic observations, Southwestern Taiwan is moving at a rate of approximately 13-42 mm/yr towards the southwest relative to the stable Eurasian Plate (e.g., Yu et al., 1997; Ching et al., 2007). In some specific areas, such as the Zhongliao Tunnel on National Freeway No. 3 near the Lungchuan Fault and Chishan Fault, the surface is rapidly uplifting at a rate of 80 mm/yr, and there is still no common accepted interpretation for this phenomenon (Yang et al., 2015).

The Pingtung Plain, enclosed by the right-lateral Chishan Fault and left-lateral Chaochou Fault, is moving at a rate of approximately 50 mm/yr towards the southwest (Hu et al., 2007). Lu & Malavieille (1994) conducted laboratory sandbox simulations to study the tectonic structure of Taiwan's oblique collision orogenic movement. Lu (1994)

doi: 10.6342/NTU202500538

proposed the tectonic escape structure for the Taiwan orogenic belt based on these simulations. Previous studies further analyzed the trend of fault activity and data from continuous GNSS stations on the Earth's surface, suggesting a southwestward escape trend in the tectonic block between the Chishan Fault and Chaochou Fault, supporting this hypothesis (Lacombe et al., 2001; Ching et al., 2007; Angelier et al., 2009).

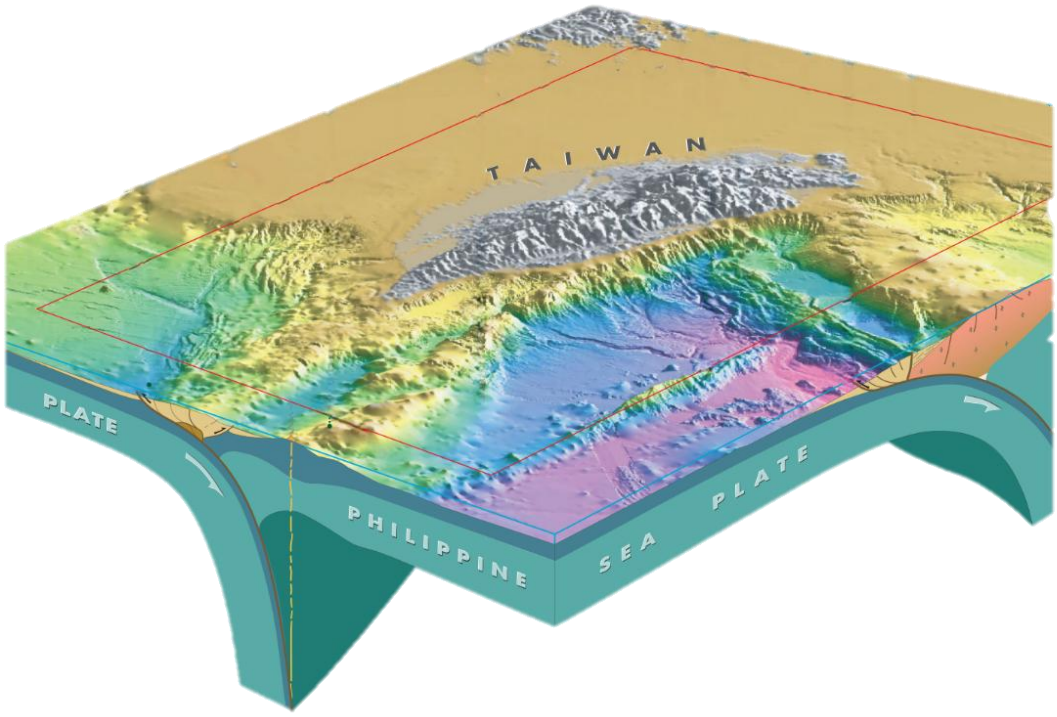

Figure 19. Adapted from Malavieille et al. (2021), this figure illustrates the tectonic geometry near the island of Taiwan.

doi: 10.6342/NTU202500538

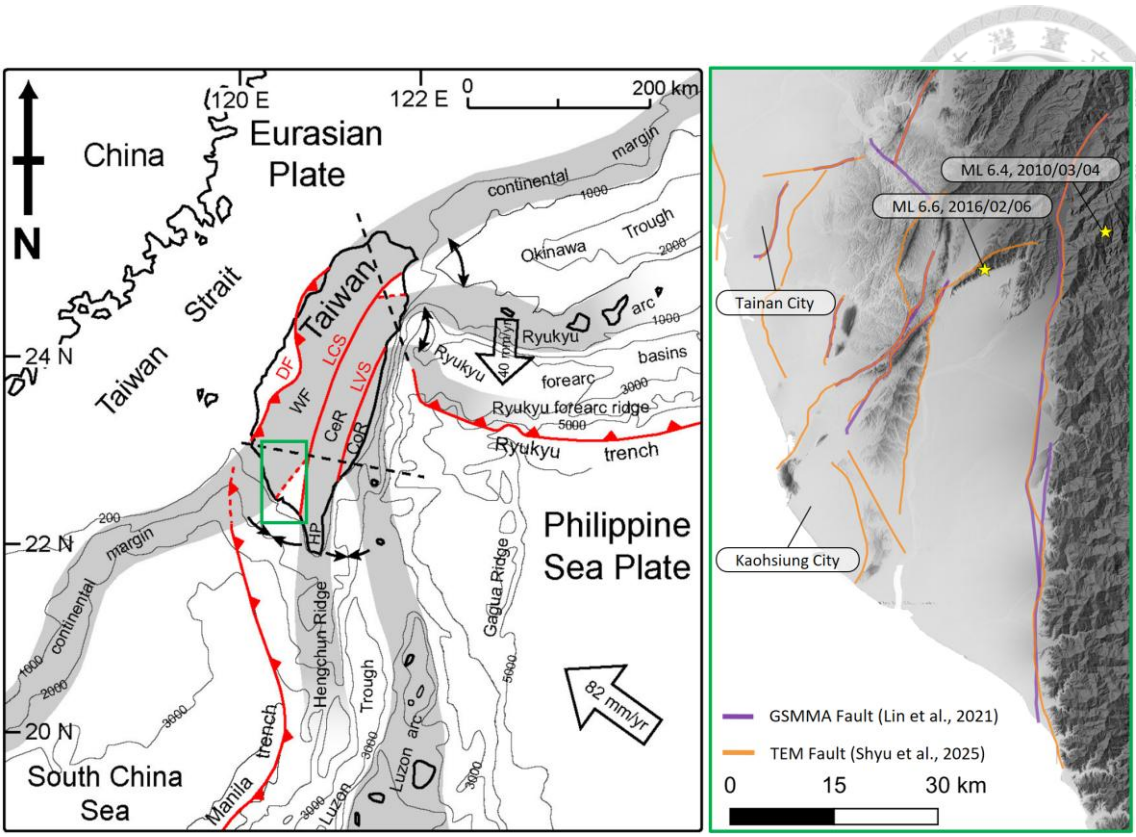

Figure 20. The map on the left, adapted from Shyu (2006), illustrates the plate boundary near Taiwan, emphasizing the high convergence rate of approximately 82 mm/yr. The green rectangle outlines Southwestern Taiwan, which is expanded in the map on the right. The right panel displays active structures as documented by Lin et al. (2021) and Shyu et al. (2025), along with the epicenters of the two significant earthquakes.

doi: 10.6342/NTU202500538

3.2. Active Structures in Southwestern Taiwan

The study area is located south of the Hsinhua Fault and west of the Chaochou Fault, encompassing the southern section of the Western Foothills and the coastal plains. This region hosts numerous imbricate thrust faults, predominantly trending in a north-south direction.

Geological surveys in this area date back to the Japanese colonial period, when early geological maps were produced by Yoshida (1932) and Torii (1932a, b). Subsequently, since the 1960s, geological surveys conducted by the Chinese Petroleum Corporation (CPC) have significantly expanded our understanding (e.g., Sun, 1964; Chou, 1971; Hsieh, 1972). More recently, researchers have further integrated geological investigations, geodetic observation data, and field surveys of seismic events to create modern fault maps, such as the Active Fault Map of Taiwan (Lin et al., 2021), the Taiwan Earthquake Model (Shyu et al., 2025), and The seismic zones of Taiwan (Chen et al., 2024). Collectively, these provide critical scientific foundations for earthquake risk assessments and infrastructure planning.

According to the definition provided by the Geological Survey and Mining Management Agency (GSMMA) of the Ministry of Economic Affairs in Taiwan, an active fault is "a fault that has been active since the late Pleistocene (approximately 100,000 years ago) and is likely to become active again in the future" (Lin et al., 2012). These faults can be identified through surface topography and stratigraphic features or mapped using seismic surveys and geodetic methods.

Specifically, Southwestern Taiwan exhibits the highest rates of surface deformation in Taiwan, with an east-west shortening rate of approximately 40 mm/yr from the foothills to the plains (Yu et al., 1997; Tsai et al., 2015). Despite this rapid tectonic activity, the seismicity in this region is relatively low, and devastating earthquakes are less frequent

doi: 10.6342/NTU202500538

than in eastern Taiwan. This phenomenon may be associated with rapid aseismic deformation of the shallow crust during interseismic periods.

Advances in geodetic techniques have enabled researchers to observe these active shallow structural movements during interseismic periods. These methods complement traditional geological approaches by revealing significant activity in young structures that are not easily identifiable in geological records but are prominent over geodetic time scales. These relatively young structures, discovered through geodetic data, exhibit high activity in Southwestern Taiwan and thus challenge the conventional definition of active faults.

In this chapter, I will divide the study area into five subregions based on the distribution of major faults in Southwestern Taiwan and review relevant studies on these active structures.

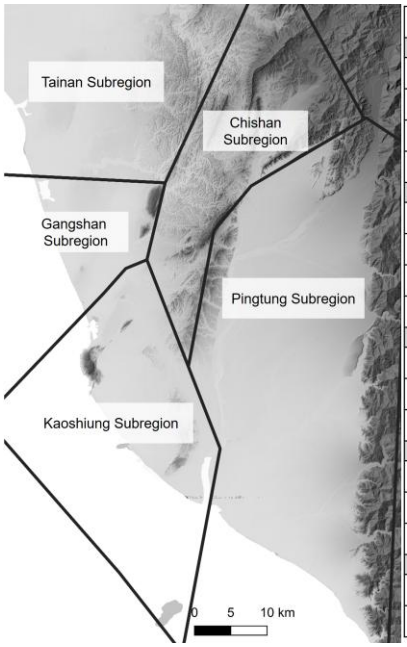

	Sun, 1964; Chou, 1971	Lacombe et al., 1999	Chen et al., 2011	Chao, 2016; Ching, 2017	Le Béon, 2019	Tung, 2021	Lin et al., 2021	Hu, 2025	Shyu et al., 2025
Tainan Subregion 台南構造區 (refer to section 3.2.1)									
Hsinhua Fault 新化斷層			V		V		V	V	V
Houchiali Fault 後甲里斷層	V	V			V		V	V	V
Tainan Fault 台南斷層		V	V						
Chungchou Fault 中洲斷層	V	V	V					V	V
Gangshan Subregion 岡山構造區 (refer to section 3.2.2)									
Chungchou Fault 中洲斷層		V	V					V	V
Hsiaokangshan Fault 小岡山斷層	V	V	V	V			V	V	V
Tadishan Fault 潭底山斷層				V					
Chikang Fault 赤崗斷層	V	V						V	
Chishan Subregion 旗山構造區 (refer to section 3.2.3)									
Lungchuan Fault 龍船斷層	V	V	V	V					V
Chekualin Fault 車瓜林斷層	V	V	V	V			V		V
Chishan Fault 旗山斷層	V	V	V	V			V		V
Kaohsiung Subregion 高雄構造區 (refer to section 3.2.4)									
Youchang Fault 右昌斷層	V	V	V	V					V
Shoushan Fault 壽山斷層	V	V							
Fengshan Fault 鳳山斷層	V		V	V					V
Pingtung Subregion 屏東構造區 (refer to section 3.2.5)									
Kaoping River Fault 高屏溪斷層			V						V
Chaochou Fault 潮州斷層			V				V		V

Figure 21. Map illustrating the five subregions of the study area: Tainan, Gangshan, Chishan, Kaohsiung, and Pingtung Subregions. The table on the right lists active faults referenced in the following sections, along with previous studies that have addressed each fault.

doi: 10.6342/NTU202500538

3.2.1. Tainan Subregion

In the northern part of this subregion lies the Hsinhua Fault, an ENE-striking high-angle strike-slip fault. The magnitude 6.3 earthquake on Dec. 5, 1946, caused surface ruptures along the Hsinhua Fault, with a maximum horizontal displacement of 2 meters and a vertical deformation of up to 76 cm (Chang et al., 1947; Bonilla, 1977). Shallow seismic profiles indicate that the fault appears as a broad shear zone in the shallow subsurface, with rock layers cut by high-angle discontinuities forming a flower structure (Lin et al., 2007). According to the drilling data from Chen et al. (2011), the long-term vertical slip rate of the Hsinhua Fault is approximately 0.8-4.5 mm/yr.

South of Hsinhua, the main structural features include the Tainan Anticline, the Tawan Syncline, the Chungchou Anticline, and the Guanmiao Syncline, all trending north-south. Early researchers (Pan, 1968; Hsieh, 1972; Sun, 1964) used seismic, gravity, and aerial photography methods to suggest that these en echelon structures may originate from mud diapir activities under regional compressional stress. Rapid structural uplift in the Tainan and Chungchou Anticlines has formed young marine terraces on the Tainan Tableland and Chungchou Tableland, composed of Holocene marine strata.

Chen & Liu (2000) suggested that the formation of the Tainan Anticline is related to mud diapir activity. Using carbon isotope dating and paleo-sea-level reconstruction, they estimated an absolute uplift rate of approximately 5 mm/yr over the past 6,000 to 10,000 years. Lacombe et al. (1999) identified the Tainan Fault along the front of the Tainan Tableland based on digital elevation models (DEM), borehole data, and seismic profiles. They interpreted it as an east-dipping thrust fault. Additionally, the Houchiali Fault on the eastern edge of the Tainan Tableland was initially identified as a high-angle normal fault based on bedding dips (Lin, 1957) but was later reinterpreted as a west-dipping thrust fault by Sun (1964). Le Béon et al. (2019) proposed that the northern end of the Houchiali

doi: 10.6342/NTU202500538

Fault may connect to the surface rupture of the 1946 Hsinhua earthquake, linking it to the Hsinhua Fault.

The Chungchou Anticline is another significant structural feature in the region. Based on seismic profiles, gravity measurements, and borehole data, researchers (Pan, 1968; Hsieh, 1972) associated its activity with mud diapir, with normal faults developing on both sides of the anticline. Sun (1964) observed abrupt stream channel shifts along the western edge of the Chungchou Anticline from aerial photos, suggesting the presence of a fault, which he named the Liuchiatien Fault. Lacombe et al. (1999) noted the asymmetry of the Chungchou Anticline, with its western edge forming a linear fault scarp likely caused by activity along an east-dipping thrust fault. Borehole data further confirmed the existence of the thrust fault (Chen & Yu, 2007), with an estimated vertical deformation rate of 5.8–6.4 mm/yr. Carbon isotope dating by Chen & Liu (2000) suggested an uplift

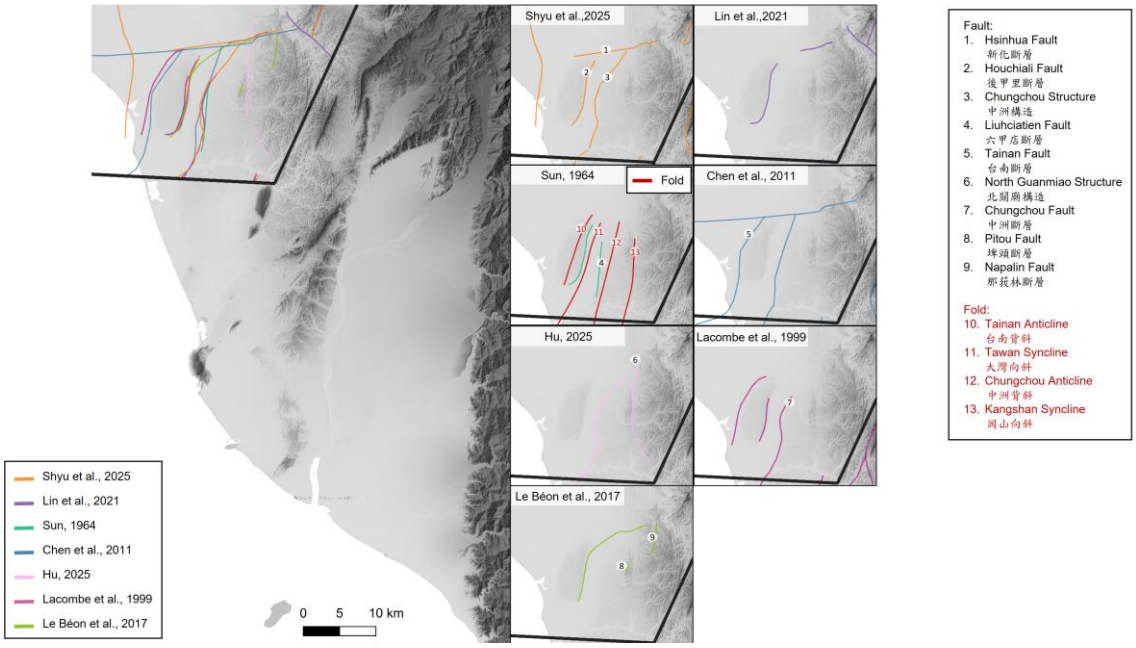

Figure 22. Active faults and folds in the Tainan subregion as identified by various researchers. The maps on the right show contributions from each study. The English and Chinese names of each location, fault, and fold are listed in the inset for reference.

doi: 10.6342/NTU202500538

rate of 4–7 mm/yr over the past 6,000–8,000 years, increasing eastward. This trend indicates that the tableland's formation is jointly influenced by mud diapir and active faulting. Chen et al. (2011) proposed that the Chungchou Fault connects northward to the Hsinhua Fault and extends southward to the coastal areas of Mituo, forming the leading edge of the Western Foothills' thrust fault system. Based on flexural scarp features, Hu (2025) suggested that this fault extends 30 km from Liuchiatien to Mituo.

The Guanmiao Syncline lies east of the Chungchou Anticline. Sun (1964) originally referred to it as the Kangshan Syncline. Le Béon (2017), using coseismic deformation fields from the 2016 Meinong earthquake derived from InSAR, field investigations of surface ruptures, and seismic profiles provided by Huang et al. (2004), identified a west-dipping thrust fault on the western side of the syncline, named the Pitou Fault. This fault forms an en echelon pattern with the north-south-trending Napalin Fault to the north. Hu (2025) further mapped a similar north-south-trending west-dipping thrust fault in this area based on the linear distribution of flexural scarps.

doi: 10.6342/NTU202500538

3.2.2. Gangshan Subregion

The primary structural features of this subregion are the Chungchou Anticline and the Takangshan Anticline, both trending north-south. Lacombe (1999) mapped the Chungchou Fault along the western margin of the Chungchou Anticline. Hu (2025) identified a flexural scarp associated with the fault, indicating that it extends from Luzhu to Mituo, spanning a total length of approximately 30 km.

Between the Chungchou and Takangshan Anticlines, Sun (1964), based on aerial photographs and seismic profile data, mapped a north-south-trending Kangshan Syncline and identified the Hsiaokangshan Fault along its eastern side. Shen et al. (2005) recorded six small linear scarps, each approximately 5 meters high, along the Hsiaokangshan Fault, providing geomorphic evidence of its activity. Chen et al. (2010) analyzed marine terrace distributions and stratigraphic data from the hanging wall and footwall, suggesting that the Hsiaokangshan Fault might extend southward to connect with the Youchang Fault. However, most researchers consider the southern boundary of the Hsiaokangshan Fault to be delineated by the Agongdian River, as the topographic features south of the river are less distinct (e.g., Shyu et al., 2016; Lin et al., 2021; Hu, 2025).

Several studies have also focused on quantifying the rates of uplift and slip along these structures. Chen et al. (2010), for instance, used borehole data to estimate that the hanging wall and footwall of the Hsiaokangshan Fault experience an uplift rate of approximately 2.2 to 4.4 mm/yr. Complementary findings by Shyu et al. (2020), which integrated coral reef dating and terrace offset analysis, point to a vertical slip rate of roughly 0.5–2.7 mm/yr.

In the Mituo area, various fault geometries have been proposed. Sun (1964) suggested that the Chungchou Anticline extends southward to Tadishan and identified NE–SW-trending faults on both sides of Tadishan mud volcano. Hsu & Chang (1979)

doi: 10.6342/NTU202500538

referred to it as Chihkan Fault. Lacombe (1999) indicated that Tadishan lies on a NE–SW-trending anticline distinct from the Chungchou Anticline, with its western margin marked by a NE–SW-trending thrust fault. Ching (2017), based on an analysis of ALOS InSAR and GNSS velocity fields, proposed that Tadishan is cut by an E–W-trending active fault, naming it the Tadishan Fault. Ching interpreted it as a thrust fault with a right-lateral component. These varying interpretations highlight the need for further research to fully clarify the complex fault geometry in this tectonically active region.

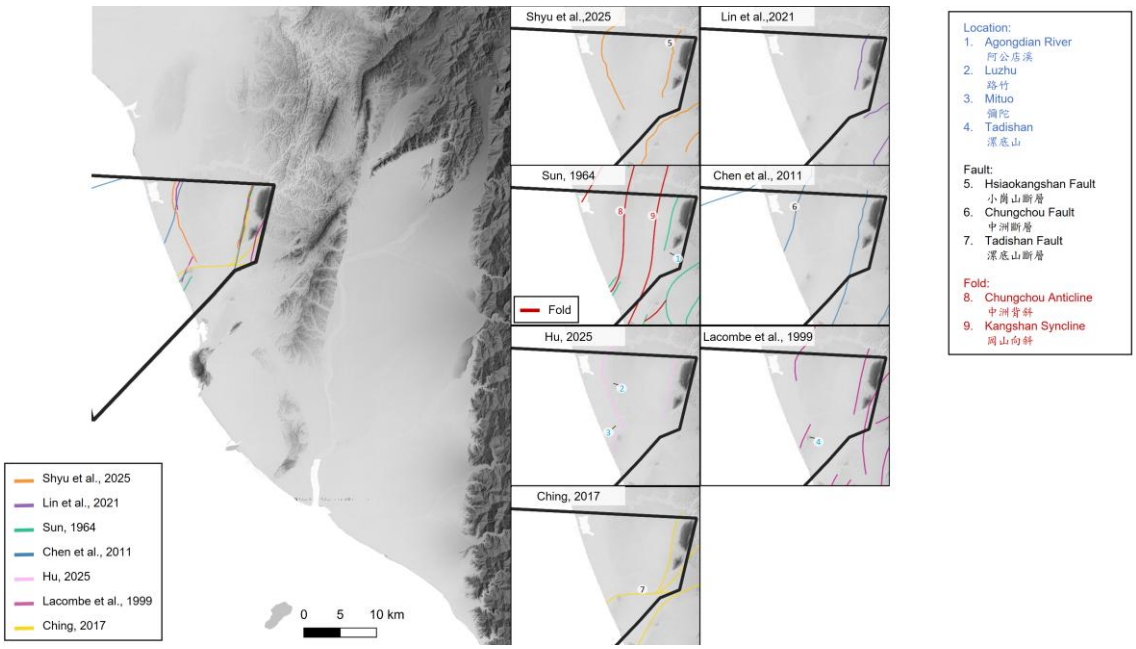

Figure 23. Active faults and folds in the Gangshan subregion as identified by various researchers. The maps on the right show contributions from each study. The English and Chinese names of each location, fault, and fold are listed in the inset for reference.

doi: 10.6342/NTU202500538

3.2.3. Chishan Subregion

The Chishan Subregion encompasses the major geological structures of the southwestern foothills of Taiwan, with the Chishan Fault being the most prominent thrust fault. The western side of the fault consists of thick mudstone layers from the Gutingkeng Formation, characterized by typical badland topography, while the eastern side features interbedded sandstone and shale of the Late Miocene, forming hilly terrains. The Chishan Fault was first mentioned in topographic and geological maps drawn by Yoshida (1932). Early CPC reports (Sun, 1964; Chou, 1971) mapped the Chishan Fault based on aerial photographs and topographic analysis, noting that it extends southward from Chishan through Renwu and gradually curves southeastward, developing parallel to the Fengshan Fault. According to the fault traces mapped by the GSMMA (Lin et al., 2021), the Chishan Fault originates near Chishan, passes through the Zhongliao Tunnel along National Freeway No. 3, and extends southward through Shenshui River to Dashe. Beyond this point, it gradually disappears into the alluvial plain, where its trace becomes indistinct.

Chen et al. (2011) suggested that the Chishan Fault formed approximately 1.6 million years ago, with a cumulative vertical displacement of up to 2,000 meters, making it a key thrust fault system within the foreland basin of Southwestern Taiwan. Outcrops of the Chishan Fault can be observed in areas such as Chishan, Zhongliao Tunnel, and Shenshui River. The fault has an eastward dip with an angle of 55–65 degrees, displaying the typical characteristics of a thrust fault (Song et al., 2005; Chen, 2005; Lin et al., 2009; Chiu et al., 2019). Based on fault plane striations observed in field surveys, Chen (2005) proposed that the Chishan Fault has a left-lateral component. However, GPS data analyses indicate a right-lateral component, with thrust faulting motion (Lacombe et al., 2001; Ching et al., 2007; Hu et al., 2007; Rau et al., 2010). Near the Zhongliao Tunnel on National Freeway No. 3, the fault exhibits extensional motion with a right-lateral component, resulting in

doi: 10.6342/NTU202500538

an uplift rate of up to 80 mm/yr in the hanging wall (Chang-Lee, 2014; Chen, 2015). These geodetic observations differ from the geological characteristics that define the Chishan Fault as an east-dipping thrust fault.

The Chekualin Fault lies west of the Chishan Fault. Early reports from the CPC (Sun, 1964; Chou, 1971) described a fault along Lungchuan Hill extending southward to the Chekualin area, running parallel to the Chishan Fault. Upon reaching the alluvial plain, the fault curves southeast near Ciaotou and connects with the Fengshan Fault. However, the GSMMA did not identify an active fault near Lungchuan but mapped the Chekualin Fault near the Chekualin area with a similar NE–SW orientation (Lin et al., 2021). As the fault extends southward into the plains, its trace becomes indistinct, terminating near Ciaotou. Ching (2017), based on surface deformation trends observed in ALOS InSAR data, proposed that the Chekualin Fault might extend further southward and connect with the Youchang Fault.

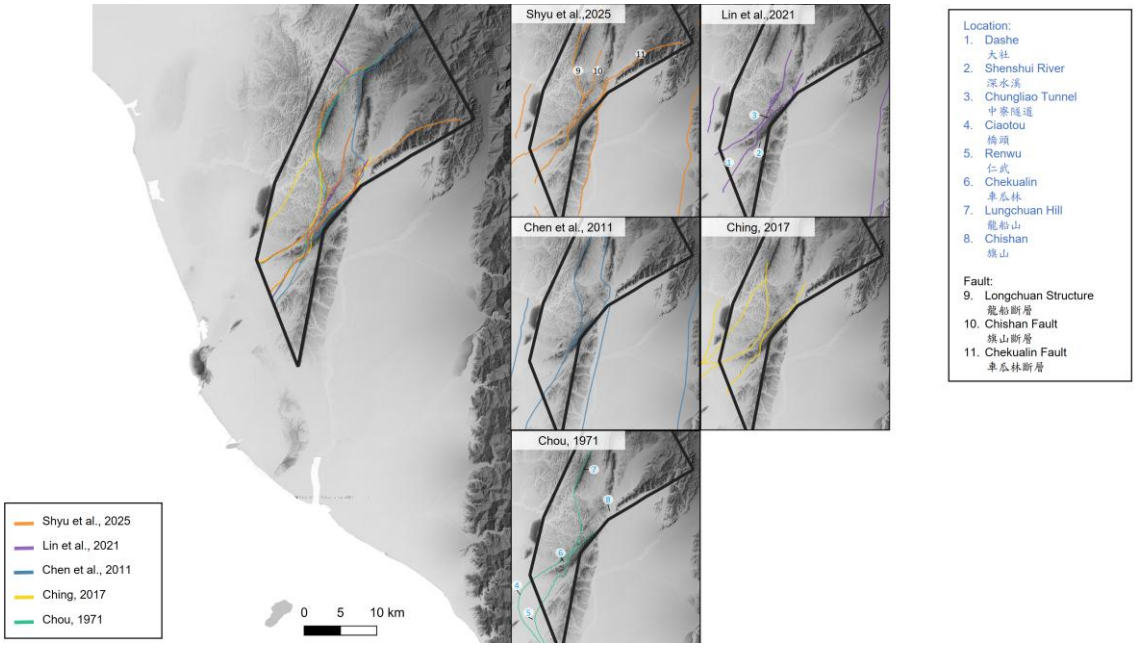

Figure 24. Active faults and folds in the Chishan subregion as identified by various researchers. The maps on the right show contributions from each study. The English and Chinese names of each location, fault, and fold are listed in the inset for reference.

doi: 10.6342/NTU202500538

3.2.4. Kaohsiung Subregion

This subregion includes two major anticlines: the NE–SW-trending Panpingshan Anticline and the NW–SE-trending Fengshan Anticline. Based on stratigraphic attitudes and aerial photo analysis, Sun (1963, 1964) suggested that the Panpingshan Anticline is cut by the Youchang Fault and the Shoushan Fault, with the latter being an east-dipping thrust fault. Some studies have attempted to link the Shoushan Fault with the similarly trending Chishan Fault to explain the southwest-directed tectonic escape in the Kaohsiung-Pingtung area (Lacombe et al., 2001; Ching et al., 2007), but this hypothesis lacks geological evidence. Using borehole data, Chen et al. (2010) proposed that the Youchang Fault might connect with the Hsiaokangshan Fault based on the similarity of sedimentary layers observed between the two faults.

Shyu et al. (2005), using DEM, identified a series of tectonic scarps around the Panpingshan Anticline, attributing their formation to active fault motion with a right-

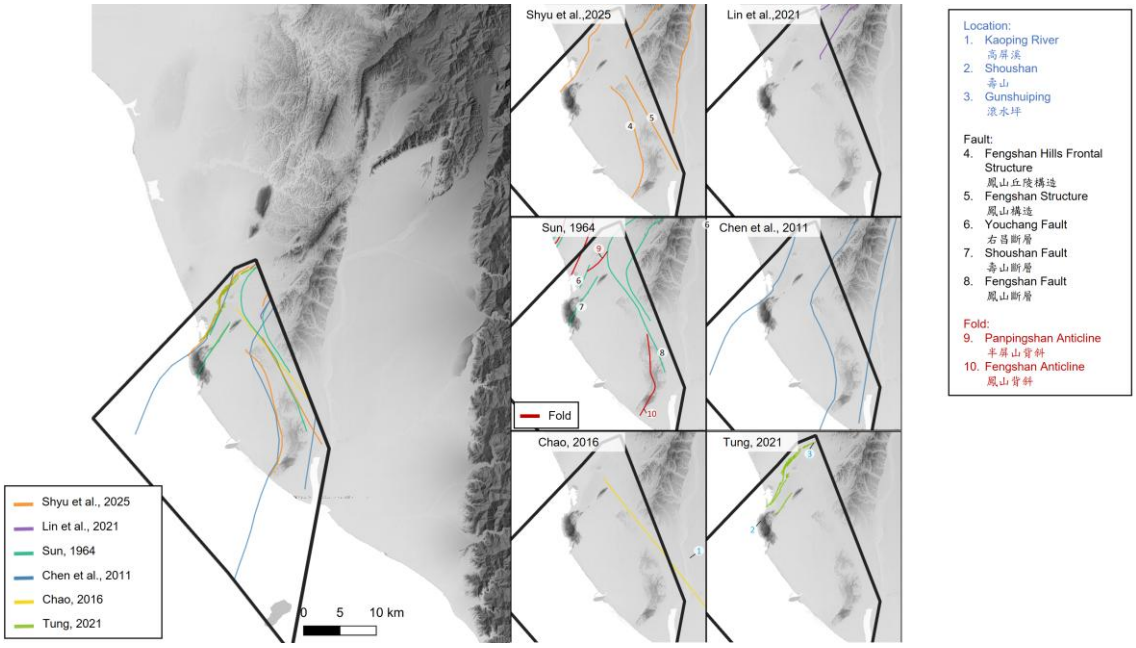

Figure 25. Active faults and folds in the Kaoshiung subregion as identified by various researchers. The maps on the right show contributions from each study. The English and Chinese names of each location, fault, and fold are listed in the inset for reference.

doi: 10.6342/NTU202500538

lateral component. Tung (2021) further combined structural geomorphology analyses to map the fault scarp distribution of the Youchang Fault, revealing that it extends southwestward from the Gunshuiping mud volcano, passing northwest of Shoushan before reaching the sea. Tung's study also identified the formation of at least four stages of river terraces, which may be linked to the activity of the Youchang Fault.

The Fengshan Anticline occupies another significant position in the Kaohsiung Subregion. Sun (1964), based on aerial photo interpretation, observed a topographic scarp along the eastern side of the Fengshan Anticline and named it the Fengshan Fault. Shyu et al. (2005) identified additional tectonic scarps on both the eastern and western sides of the Fengshan Hills, concluding that the eastern structure is dominated by left-lateral motion, while the western Fengshan Hills are primarily influenced by thrust faulting. Using ALOS InSAR data, Chao (2016) observed variations in surface velocity fields on both sides of the Fengshan Fault, suggesting that the fault intersects with the Youchang Fault to the north and extends southward across the Kaoping River before entering the Pingtung Plain.

3.2.5. Pingtung Subregioin

The Pingtung Plain hosts two major geological structures identified in previous studies: the Chaochou Fault and the Kaoping River Fault.

The Chaochou Fault is an east-dipping thrust fault. Based on borehole data and stratigraphic distribution, Chen et al. (2011) suggested that the fault formed around 2.2–2.6 Ma, with a cumulative vertical displacement exceeding 4,000 meters, making it another major thrust fault system in the southwestern foreland basin alongside the Chishan Fault. The fault creates prominent flexural scarps on the surface, influencing the distribution of river terraces along its trace (Shyu et al., 2005; Ota et al., 2024). Shyu et

doi: 10.6342/NTU202500538

al. (2016), using the elevation of lateritic terraces, estimated the vertical uplift rate of the Chaochou Fault to range from 0.28 to 1.5 mm/yr.

The Kaoping River Fault, located along the western side of the Pingtung Plain, is a north-south-trending, west-dipping thrust fault. Shyu et al. (2005) proposed that river terraces on the western bank of the Kaoping River are closely associated with this structure, initially naming it the West Pingtung Plain Fault. In the subsequent publications, it was referred to as the Kaoping River Fault/Structure (e.g. Shyu et al., 2016; Ota et al., 2024). Based on analyses of lateritic terrace elevations, Shyu et al. (2016) estimated the vertical uplift rate of the Kaoping River Fault to be approximately 0.08–0.69 mm/yr.

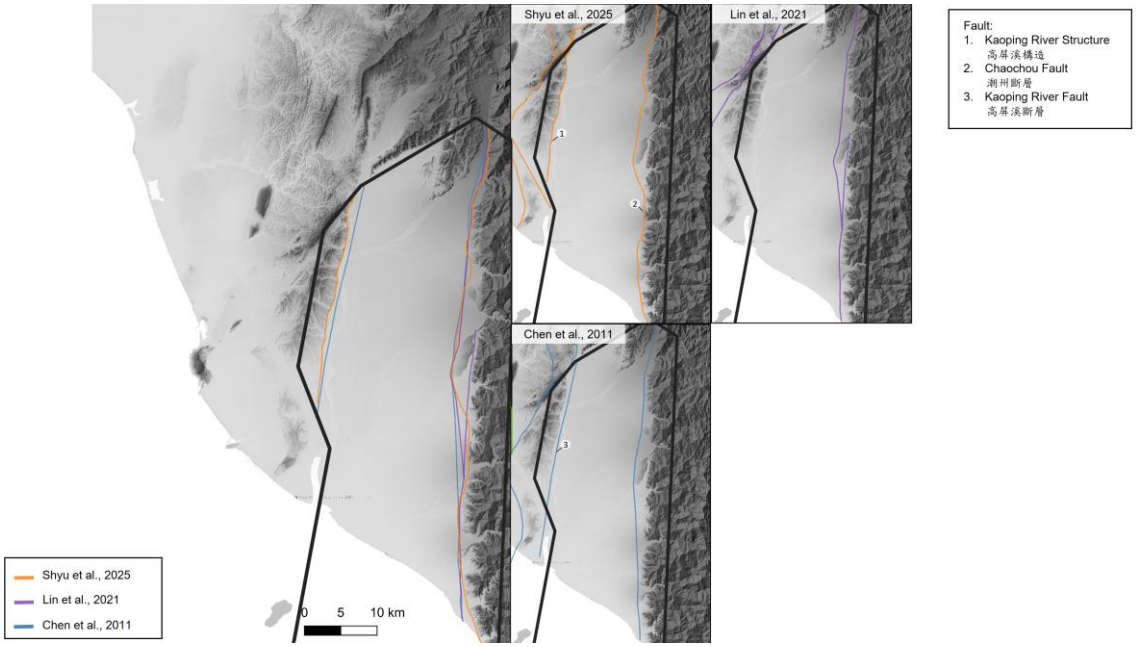

Figure 26. Active faults and folds in the Pingtung subregion as identified by various researchers. The maps on the right show contributions from each study. The English and Chinese names of each location, fault, and fold are listed in the inset for reference.

doi: 10.6342/NTU202500538

3.3. Jiashian Earthquake and Meinong Earthquake

In recent years, the Jiashian (2010) and Meinong (2016) earthquakes in Southwestern Taiwan have drawn significant academic interest due to their similar seismic mechanisms and regional impacts. The Jiashian earthquake, with a magnitude of Mw 6.3, occurred on March 4, 2010, at a depth of approximately 23 km. Studies by Huang et al. (2011), Rau et al. (2012), and Wen et al. (2012) revealed a northwest-southeast (NW-SE) oriented fault plane with a left-lateral strike-slip behavior.

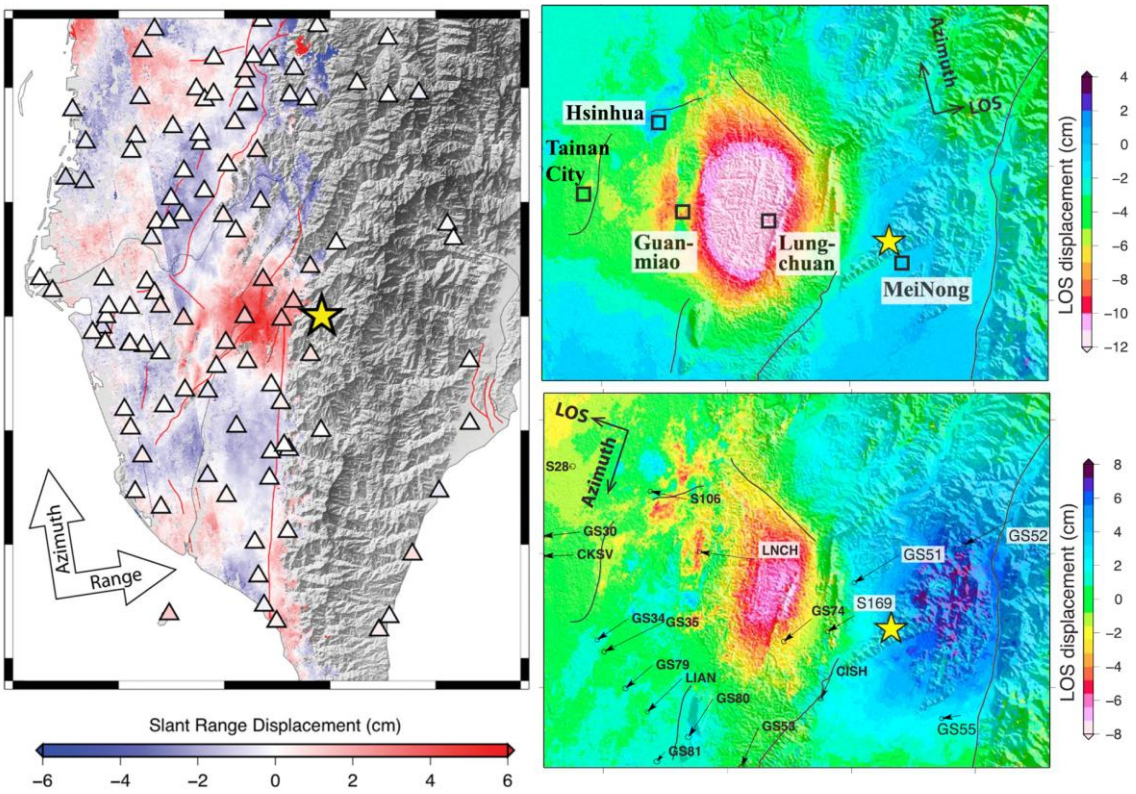

Figure 27. Left panel is the coseismic deformation map of the 2010 Jiashian earthquake derived by Huang et al. (2013). Right panel shows the 2016 Meinong coseismic deformation of two different InSAR geometries (Huang et al., 2016). The yellow stars mark the epicenter, and the red and blue zones indicate surface movement away from and toward the satellite, respectively.

doi: 10.6342/NTU202500538

Although various studies concluded a similar result regarding the focal mechanism of the main shock, the lack of surface rupture in the Jiashian earthquake has led to different interpretations of the involved fault planes. Hsu et al. (2011) proposed that the Jiashian earthquake was caused by rupture on a blind fault beneath the Earth's surface, while Lin et al. (2016) suggested that two fault surfaces may have been involved. Ching et al. (2011) suggested that the earthquake rupture may belong to the Chishan Transfer fault zone, acting as a lateral ramp in the southern segment of the foothill. In the months following the earthquake, from the InSAR observation, Huang et al. (2013) indicated that the Lungchuan Anticline experienced 20-50 mm of deformation within four months after the Jiashian earthquake

The Meinong earthquake, with a magnitude of Mw 6.4, occurred on February 6, 2016, at a depth slightly greater than the detachment surface within the regional tectonic structure, indicating a deep-seated blind fault origin similar to the Jiashian event. However, it triggered substantial shallow fault activity, likely due to stress transfer and high pore pressure, affecting faults trending north-south at depths of 5-10 km (Huang et al., 2016). This earthquake generated widespread aftershocks across three main clusters and significant ground shaking near Tainan City. Yi et al. (2023) observed that post-seismic slips were concentrated along structures on both sides of the Guanmiao Syncline, where aseismic folding may play a significant role in stress distribution.

doi: 10.6342/NTU202500538

Chapter 4 Material and Methods

4.1. SAR Imagery

The SAR images used in this study were provided by two different remote sensing satellites, the Advanced Land Observing Satellite (ALOS) and ALOS-2, both launched by JAXA. Equipped with the Phased Array type L-band Synthetic Aperture Radar (PALSAR) and PALSAR-2 systems, these satellites provided SAR imagery during their respective missions: ALOS operated from Jan. 2006 to May 2011, and ALOS-2 has been operational since May 2014.

The wavelength of those two L-band SAR system is approximately 0.23 meters, which is longer than that of other SAR systems such as Sentinel-1 (~0.06 m) and Envisat (~0.03 m). This longer wavelength allows for more reliable observations in forested areas but is more heavily influenced by ionospheric particles.

In this study, SAR images from both ALOS and ALOS-2 satellites were used to analyze ground deformation over time. For ALOS, 10 fine resolution mode images were utilized, covering the period from January 2006 to January 2010. These images are from ascending track 447, frames 430 to 460, and provided ground deformation information before the 2010 Jiashian earthquake. The azimuth angle of the ALOS images is approximately 10.6°- 10.9°, while the incidence angle is 37.0°- 40.5°. For ALOS-2, 12 StripMap 6-meter resolution images were used, spanning from July 2015 to May 2022. These images from ascending track 137, frames 430 to 470, captured the coseismic and interseismic deformation patterns of the 2016 Meinong earthquake. The azimuth angle of the ALOS-2 images is approximately 10.8°- 11.0°, with an incidence angle ranging 29.0°- 34.0°.

doi: 10.6342/NTU202500538

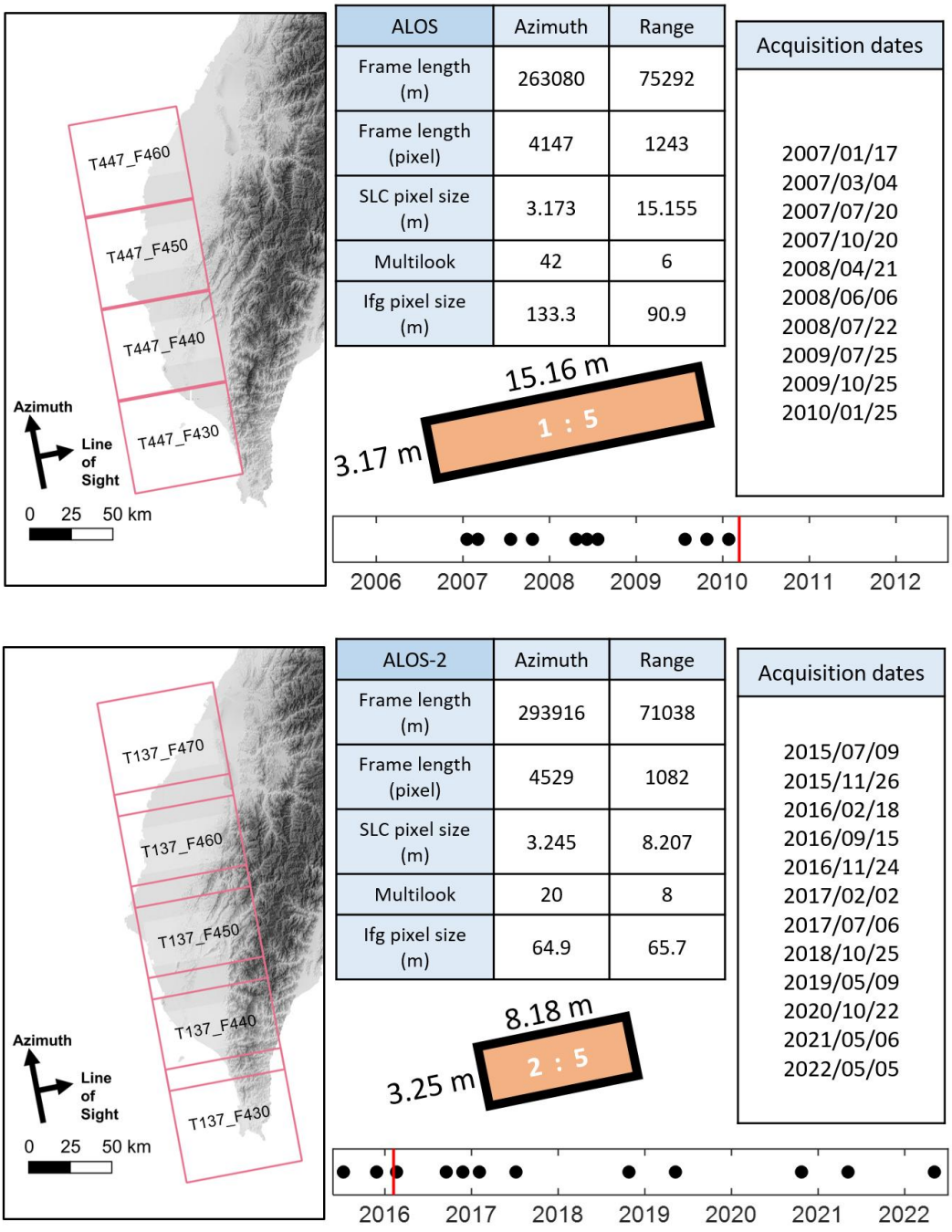

Figure 28. The two maps show the SAR image coverage of the ALOS and ALOS-2 satellite. The orange blocks simulated the pixel size of SLC ALOS and ALOS-2 image. The black points in the bottom panel indicates the image acquisition time of ALOS (2007-2010) and ALOS-2 (2015-2022). The red lines in the timeline represent the 2010 Jiashian earthquake and the 2016 Meinong earthquake, which are the key seismic events within the study period.

doi: 10.6342/NTU202500538

4.2. GNSS and Leveling Datasets

The GNSS and leveling data in this study were provided by the GSMMA under the Ministry of Economic Affairs, ROC. The GNSS data were collected from the continuous stations maintained by various organizations, including the GSMMA, Academia Sinica, the Central Weather Bureau, the Ministry of the Interior, the National Land Surveying and Mapping Center, and the Water Resources Agency. These stations provided continuous daily data that enabling precise measurements of the surface deformation in the study area.

The GNSS data were processed by a team at National Cheng Kung University, using the GipsyX software. Daily solutions were generated for each station, providing 3D displacement data in the east-west, north-south, and vertival directions. In total, 133 stations were utilized, providing a comprehensive spatial and temporal coverage of the study area.

In addition to GNSS data, leveling measurements were conducted along 5 survey lines that cross the major fault systems in the study region. Each leveling line was calibrated using a nearby continuous GNSS station as a reference point. The GNSS and leveling data offers point-based geodetic data, which are highly reliable and can be compared with the InSAR data.

doi: 10.6342/NTU202500538

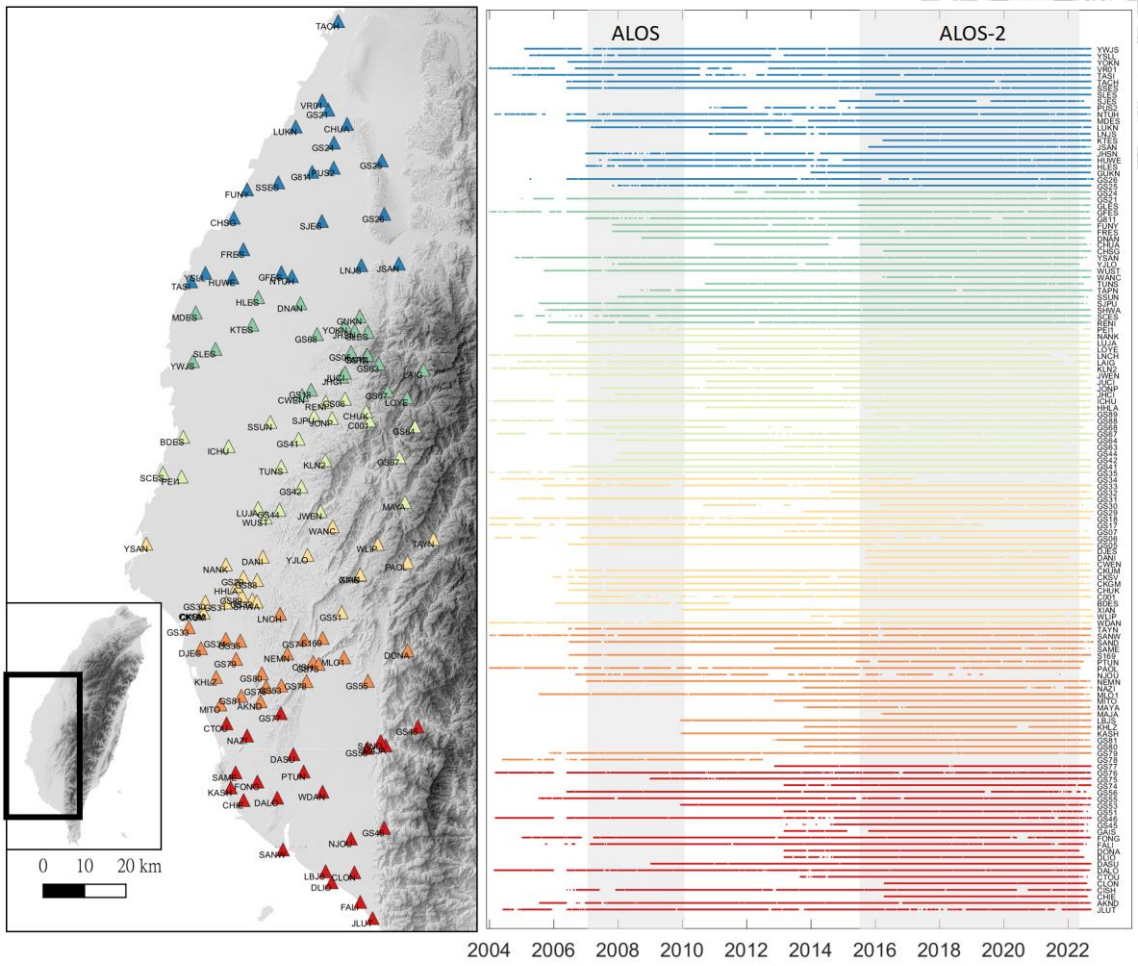

Figure 29. The left panel shows the distribution of 133 continuous GNSS stations in the study area, while the right panel illustrates the temporal coverage for each station. For visual identification, the stations are color-coded by latitude. The gray strips in the background of the time series indicate the observation periods of the ALOS and ALOS-2 satellite.

doi: 10.6342/NTU202500538

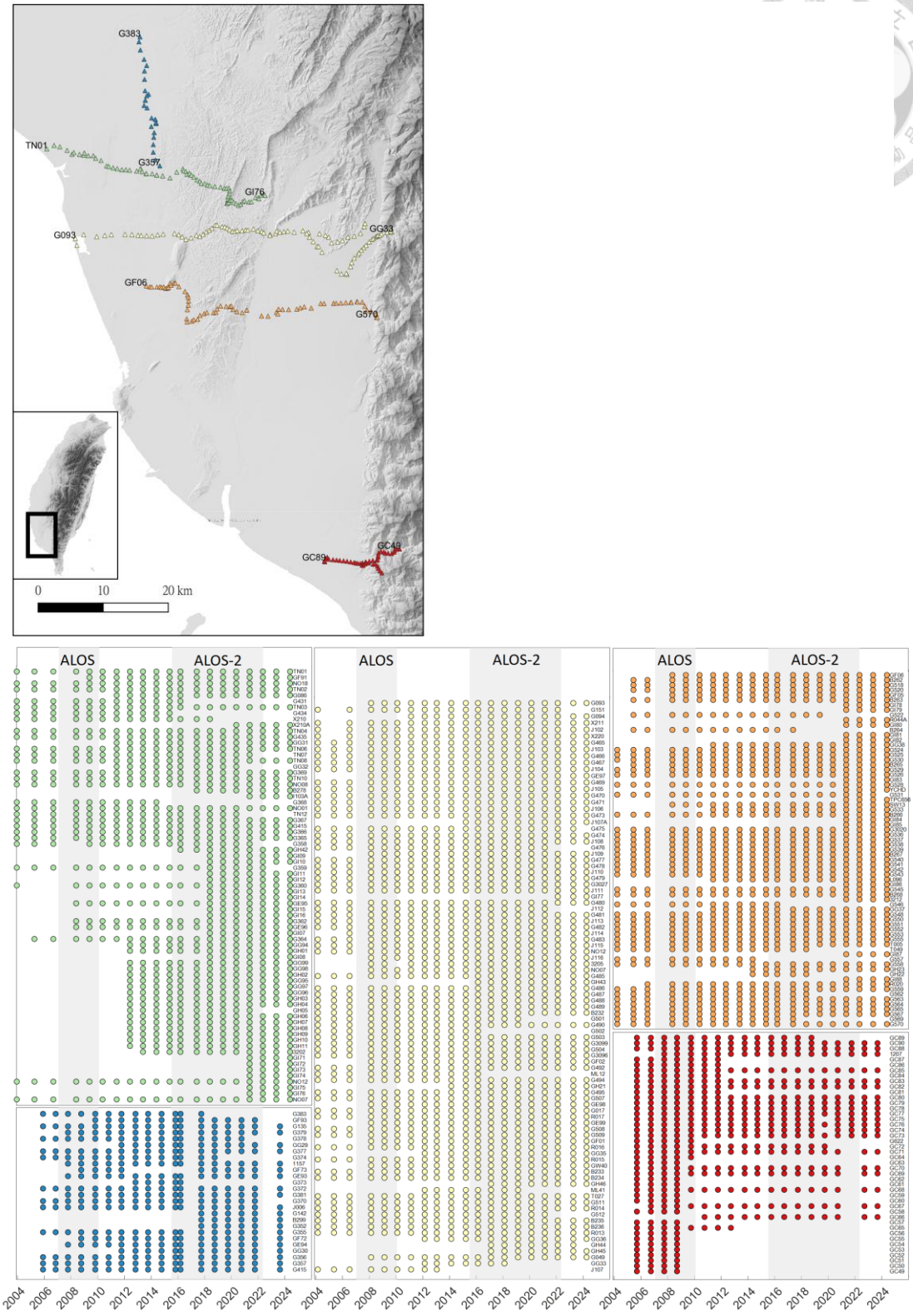

Figure 30. The top panel shows the locations of the five leveling survey lines. The bottom panels display the measure time of each stations on every survey lines, alongside the time periods of the ALOS and ALOS-2 satellite observations.

doi: 10.6342/NTU202500538

4.3. SAR Interferometry

4.3.1. ISCE

To generate interferogram network, I utilized the open-access tool Interferometric SAR Scientific Computing Environment 2 (ISCE2), funded by NASA (Rosen et al., 2012). The image mosaic, coregistration, multilooking, interferometry, and filtering were performed using ISCE's built-in processing modules. Specifically, the StripMap stack processor (Fattahi et al., 2017) was applied to process ALOS imagery, while the alosStack processor (Liang & Fielding, 2017) was used for ALOS-2 data.

In the coregistration step, pixel offsets caused by geometry differences between SAR acquisitions were mitigated using a combination of topography data from a Digital Elevation Model (DEM) and the satellite's orbital parameters. This process ensures that pixels from multiple SAR images can be aligned into the raster of the referenced SAR image, despite differences in satellite viewing angles or terrain variations. Achieving sub-pixel accuracy in this step is critical, as it directly affects the quality and coherence of the interferogram.

The acquisitions would also be resampled to reduce noise and save the computation resource. Mutliple pixels in the azimuth and range direction would be averages after the step of multilooking. This results a lower resolution but a cleaner image. For ALOS images, the multilooking factors were set at 42 looks in azimuth and 6 in range, while for ALOS-2, 20 looks in azimuth and 8 in range. These parameters ensure that both interferograms have a similar pixel size in range and azimuth direction.

The interferometry step is simply multiplying each pixel of the reference image by the conjugate of the corresponding pixel in the secondary image, producing phase values that represent the phase difference between the two images.

doi: 10.6342/NTU202500538

After the interferogram is generated, filtering is applied to refine the phase information by removing high-frequency noise. After filtering, the processor calculated the spatial coherence of the filtered interferogram. The calculated coherence, which ranged from 0 to 1, reflects the variability of the phase difference within a multilook window (default is 5*5). The spatial coherence map is helpful for assessing the reliability of the interferogram.

The phase unwrapping procedure was performed using SNAPHU (Statistical-Cost, Network-Flow Algorithm for Phase Unwrapping), developed by Chen & Zebker (2002). Phase unwrapping resolves the ambiguity of the wrapped phase, where values are confined within the range of -π to π, enabling the reconstruction of true surface deformation.

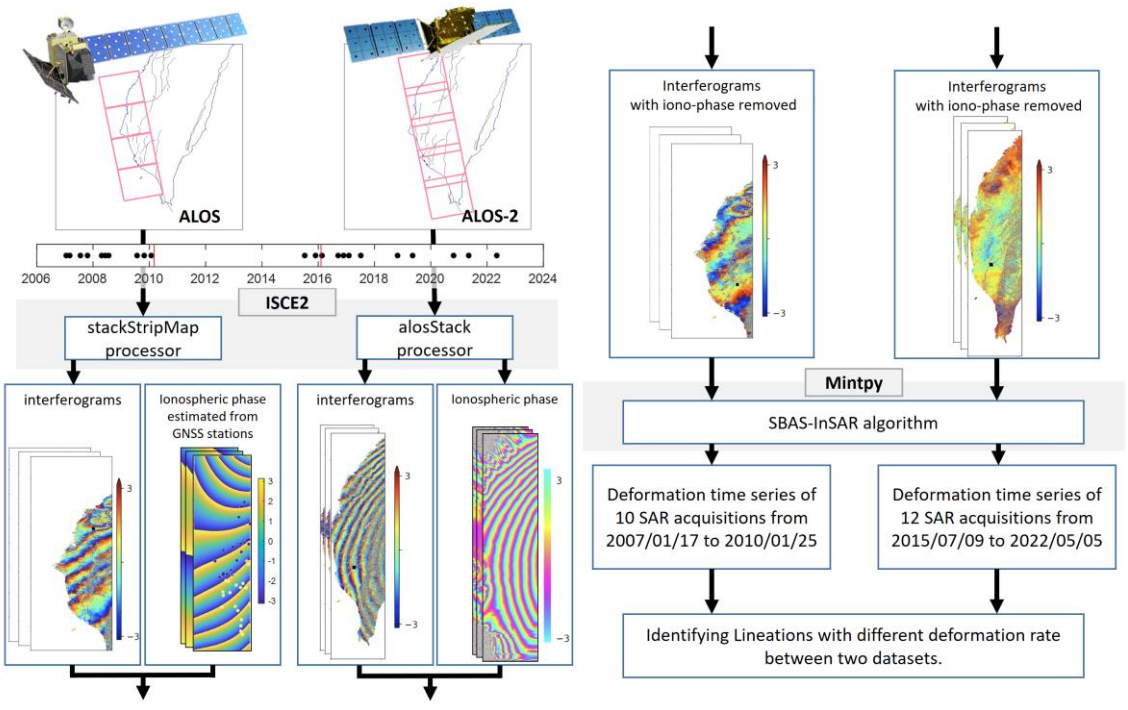

Figure 31. The InSAR processing workflow in this study. By using the module from ISCE2 and Mintpy, the ground deformation time series can be derived from the SAR SLC imagery.

doi: 10.6342/NTU202500538

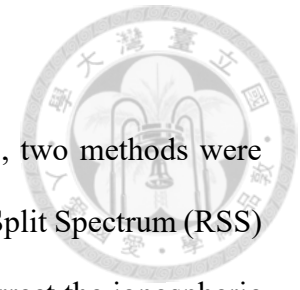

4.3.2. Ionospheric Phase Mitigation

To mitigate the ionospheric disturbances in the interferograms, two methods were applied in this study. First, for ALOS-2 imagery, the built-in Range Split Spectrum (RSS) module within the alosStack processor was used to estimate and correct the ionospheric delay. The RSS method, originally proposed by Rosen et al. (2010) and Brcic et al. (2010), and further refined by Gomba et al. (2015), can work by using the SAR image's own information. It calculates the ionospheric delay map by separating the SAR signal into two frequency bands. While this method performs well with wider-bandwidth SAR systems like ALOS-2, it is highly sensitive to noise. Thus, the effectiveness can be reduced for interferometric pairs with low coherence.

For ALOS imagery, however, same RSS method did not produce good results. To address this problem, I utilized the dense network of continuous GNSS stations in the study area to remove the ionospheric delay from the ALOS interferograms. The GInSAR (GNSS corrected InSAR) method, inspired by Tsukahara & Takada, (2018) and Neely et al. (2019) assumed that the GNSS stations can provide the true surface displacement in the LOS direction. The long-wavelength trend differences between the displacement values from ALOS interferograms and the GNSS data are attributed mainly to ionospheric delays. To model this trend difference, I fitted a third-order polynomial surface to the residuals between the InSAR and GNSS displacement values. This polynomial surface was then treated as the ionospheric delay map in the interferograms.

doi: 10.6342/NTU202500538

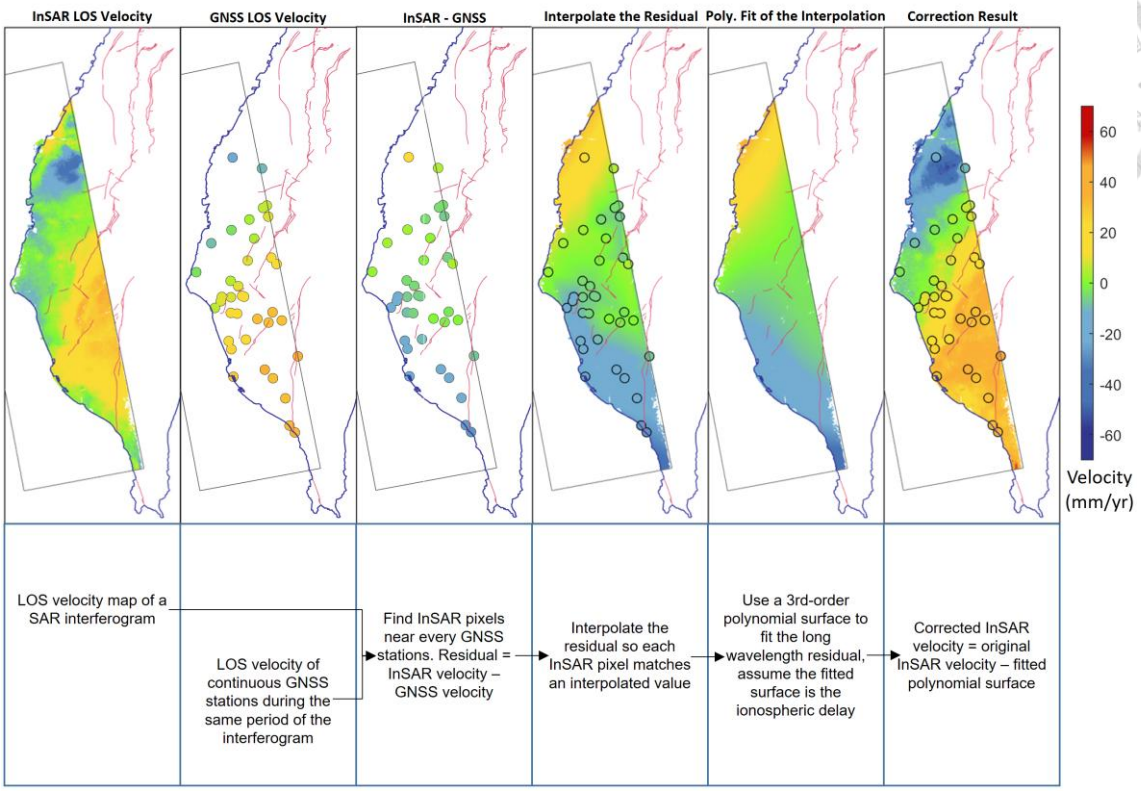

Figure 32. An example workflow of GInSAR method. Taking the advantage of high density GNSS stations in Southwestern Taiwan, this method can sufficiently extract the error ramp from InSAR interferograms.

doi: 10.6342/NTU202500538

4.4. SAR Time Series Processing

4.4.1. Mintpy

Coregistered and unwrapped SAR interferograms were input into a SBAS-InSAR algorithm, known as the Miami InSAR time-series software in Python (Mintpy), to compute the displacement time series for image pixels. Mintpy is a freely accessible Python software published by Yunjun et al. (2019). The Mintpy package enables users to customize the interferogram network with different criteria, modify the spatial and temporal reference, and set the coherence threshold for image masking. By using Mintpy, the stack of interferograms generates a deformation time series for each pixel in the image.

For the ALOS interferogram network, I manually selected interferograms based on the connected component distribution during the unwrapping step, and the quality of GInSAR-derived ionospheric correction result. Due to the inconsistencies of the mosaic step, some interferograms exhibited significant striping, which affected unwrapping quality and GInSAR estimation. As a result, I retained 20 out of 45 interferograms. For ALOS-2, I also selected interferograms from the connected component distribution during unwrapping, and 26 out of 38 interferograms were kept. The temporal coherence of each pixel was then estimated, and pixels with coherence below 0.6 for ALOS and 0.7 for ALOS-2 were discarded.

In the next step, the tropospheric phase correction module of Mintpy was applied, offering three correction methods explained in detail in the next section. The GNSS station CISH, located near Chishan City near the center of the study region, was used as the reference point for estimating ground displacement time series. This GNSS station provides high temporal coverage for ALOS and ALOS-2 data.

doi: 10.6342/NTU202500538

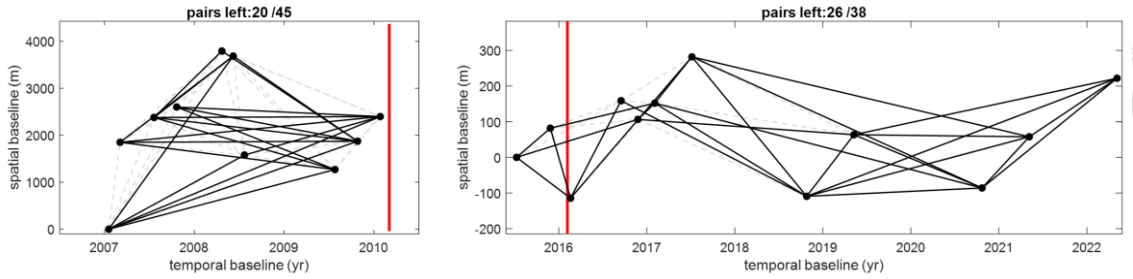

Figure 33. Baseline plot of the interferogram networks of ALOS and ALOS-2 datasets. Red line indicates the 2010 Jiashian Earthquake and the 2016 Meinong Earthquake.

4.4.2. Tropospheric Phase Mitigation

Although microwave SAR signals can avoid the absorption of water vapor, SAR images remain influenced by both the stratified and turbulent components of the Earth's troposphere. The Mintpy module offers tropospheric correction using ERA5, GACOS, or a height-correlation method. The former two are Numerical Weather Model published by European Centre for Medium-Range Weather Forecasts (Hersbach et al., 2020) and a team from Newcastle University, UK (Yu et al., 2018), which account for both tropospheric components. The height-correlation method, which assumes tropospheric delay is directly related to topography, only considers the stratified component and is particularly effective in regions with high topographic variation (Doin et al., 2009).

To evaluate each method, I calculated the change in standard deviation of each pixel's velocity time series, and the correlation between the corrected result and GNSS velocities. Results showed that the ALOS time series performed best without tropospheric correction, likely due to the GInSAR method had already mitigated tropospheric effects. For ALOS-2, however, the GACOS method provided the most effective correction.

doi: 10.6342/NTU202500538

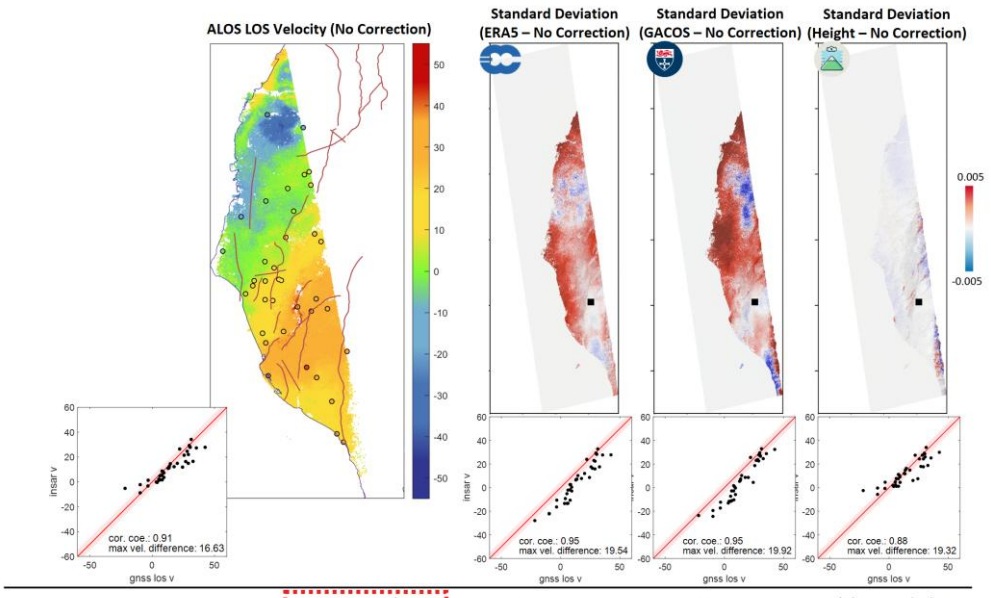

	No Correction	ERA5	GACOS	Height Correlation
Standard Deviation of Time Series	-	Worsen	Worsen	Neutral
Correlation with GNSS LOS velocity	0.91	0.95	0.95	0.88

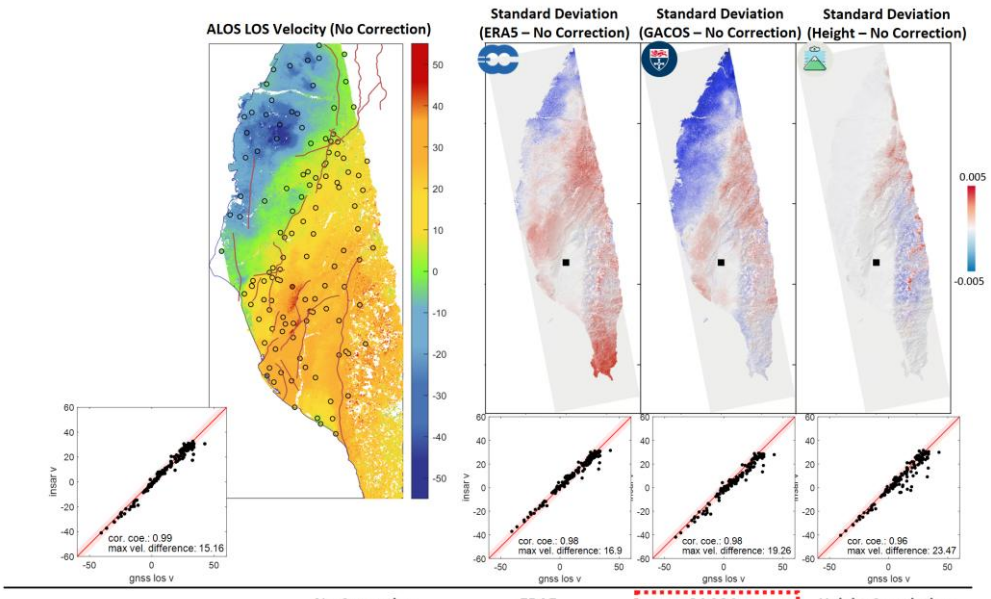

	No Correction	ERA5	GACOS	Height Correlation
Standard Deviation of Time Series	-	Worsen	Improved	Neutral
Correlation with GNSS LOS velocity	0.99	0.98	0.98	0.96

Figure 34. To evaluate the performance of ERA5, GACOS, and height correlation method, two approaches were used: the distribution of standard deviation drop, and the velocity correlation between the SAR interferogram and GNSS stations. A good result should have wide blue area that indicates the drop of velocity standard deviation, and an improved correlation coefficient between InSAR and GNSS velocities.

doi: 10.6342/NTU202500538

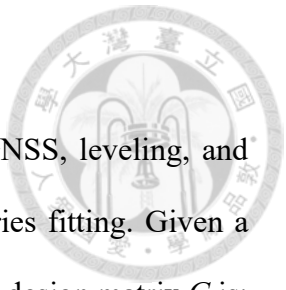

4.5. Error Estimation

To reliably compare ground displacement and velocity from GNSS, leveling, and MT-InSAR time series, error estimation is essential during time series fitting. Given a geodetic time series with time matrix *t* and displacement matrix *d*, the design matrix *G* is:

$$G = [ones(size(t)),\ t,\ sin(2pi*t),\ cos(2pi*t),\ sin(4pi*t),\ cos(4pi*t),\ coseismic,\ postseismic]$$

The formula of model inversion is:

$$m = (G^T G)^{-1} G^T d$$

From the derived model matrix *m*, the secular velocity is *m(2)*, and the coseismic deformation is *m(7)*, respectively.

To estimate uncertainties of these modeled values, I first calculated the covariance matrix for the model. Regularization was applied to avoid the matrix singularity:

$$cov = (G^T G + diag(size(m))*10^{-6})^{-1} * (std(d - G\,m))^2$$

The standard errors (SE, here after) for secular velocity and coseismic displacement were obtained from $(cov(2,2))^{0.5}$ and $(cov(7,7))^{0.5}$, respectively.

To estimate ground deformation velocity over a specific period, I calculated the SEs for the start and end points of the modeled time series. The SE at any given time index *i* was calculated as:

$$(G(i,:)*cov*G(i,:)^T)^{0.5}$$

The velocity SE between two times, t_1 and t_2, is derived from the root sum square of the two standard deviations, divided by the time interval, as:

$$((se_1/T)^2+(se_2/T)^2)^{0.5}$$

The resulting standard errors provide a consistent estimate of the model's uncertainty throughout the entire time series.

doi: 10.6342/NTU202500538

To estimate the deformation rate of a region using multiple geodetic datasets, each with rates in different directions and varying standard errors, a weighted averaging method ensures accuracy. Data points with smaller standard errors contribute more to the average, while those with larger errors have less influence. By applying this principle, the deformation rate is calculated by weighting each dataset based on its standard error, providing a more reliable result. For example, considering four InSAR observations with different LOS directions, where the LOS velocity is V_{LOS} and the error is SE_{LOS}:

$$\begin{bmatrix} V_{LOS1} \\ V_{LOS2} \\ V_{LOS3} \\ V_{LOS4} \end{bmatrix} = \begin{bmatrix} G\_LOS1_N & G\_LOS1_E & G\_LOS1_U \\ G\_LOS2_N & G\_LOS2_E & G\_LOS2_U \\ G\_LOS3_N & G\_LOS3_E & G\_LOS3_U \\ G\_LOS4_N & G\_LOS4_E & G\_LOS4_U \end{bmatrix} \begin{bmatrix} V_N \\ V_E \\ V_U \end{bmatrix} + \varepsilon$$

The geometry matrix G projects the unknown North–East–Up deformation V onto each LOS directions, and ε contains measurement errors. To incorporate the standard errors properly, we construct a covariance matrix Σ for the LOS measurements. In the simplest case, if the four LOS measurements are assumed independent, then

$$\Sigma = \begin{bmatrix} {SE_{LOS1}}^2 & 0 & 0 & 0 \\ 0 & {SE_{LOS2}}^2 & 0 & 0 \\ 0 & 0 & {SE_{LOS3}}^2 & 0 \\ 0 & 0 & 0 & {SE_{LOS4}}^2 \end{bmatrix}, W = \Sigma^{-1}$$

The weighted least squares solution then balances each LOS velocity according to its uncertainty. This leads to the 3D velocity estimate:

$$V=(G^T W G)^{-1} G^T W d$$

where $d=[V_{LOS1} ; V_{LOS2} ; V_{LOS3} ; V_{LOS4}]$. Once the V matrix is obtained, its uncertainties follow from the covariance matrix for the parameters *cov*:

$$cov=(G^T W G)^{-1}$$

and the standard error in each component is the square root of the corresponding diagonal element.

doi: 10.6342/NTU202500538

Chapter 5 Results

5.1. SAR Time Series and Result Validation

5.1.1. Temporal Coherence Map

In this section, the temporal coherence distribution maps derived from both ALOS and ALOS-2 datasets are presented. Temporal coherence (γ), calculated via the Mintpy module and was based on the concept published by Pepe & Lanari (2006), is a measure of phase stability over time for each pixel in the InSAR dataset and is calculated as follows:

$$\gamma = \frac{\left|\sum_{p=0}^{M-1} \exp\left[\, j\left(\varphi_p - \bar{\varphi}_p\right)\,\right]\right|}{M}$$

Where M is the total number of SAR acquisitions, φ_p is the phase of the p-th acquisition, and $\bar{\varphi}_p$ represents the average phase across all acquisitions. Temporal coherence values range from 0 to 1, with values closer to 1 indicating very low phase variability. Several factors can lead to a decrease in temporal coherence, including unwrapping errors, coseismic jumps, and changes in land use. Maps of temporal coherence are the key for understanding the quality of our InSAR time series analysis.

For the ALOS dataset, the larger pixel sizes result in a wider area of high coherence near the reference point in Kaohsiung and Pingtung. However, as we move northward towards Chiayi and Yunlin, a decline in temporal coherence is observed, probably due to the agricultural activities. Additionally, the low coherence in the northern region may also be related to mosaic step issues during image stitching.

In contrast, the ALOS-2 dataset, with its finer pixel size, shows lower temporal coherence outside urban areas and roads in Chiayi and Yunlin. This pattern also reflects the challenges posed by agricultural activities in these regions. Moreover, areas near the reference point in Kaohsiung and Pingtung maintain robust temporal coherence. A notable observation is the significant drop in temporal coherence east of Tainan, particularly in

doi: 10.6342/NTU202500538

the Guanmiao and Shinhua areas. This drop is likely due to the coseismic deformation of the 2016 Meinong earthquake.

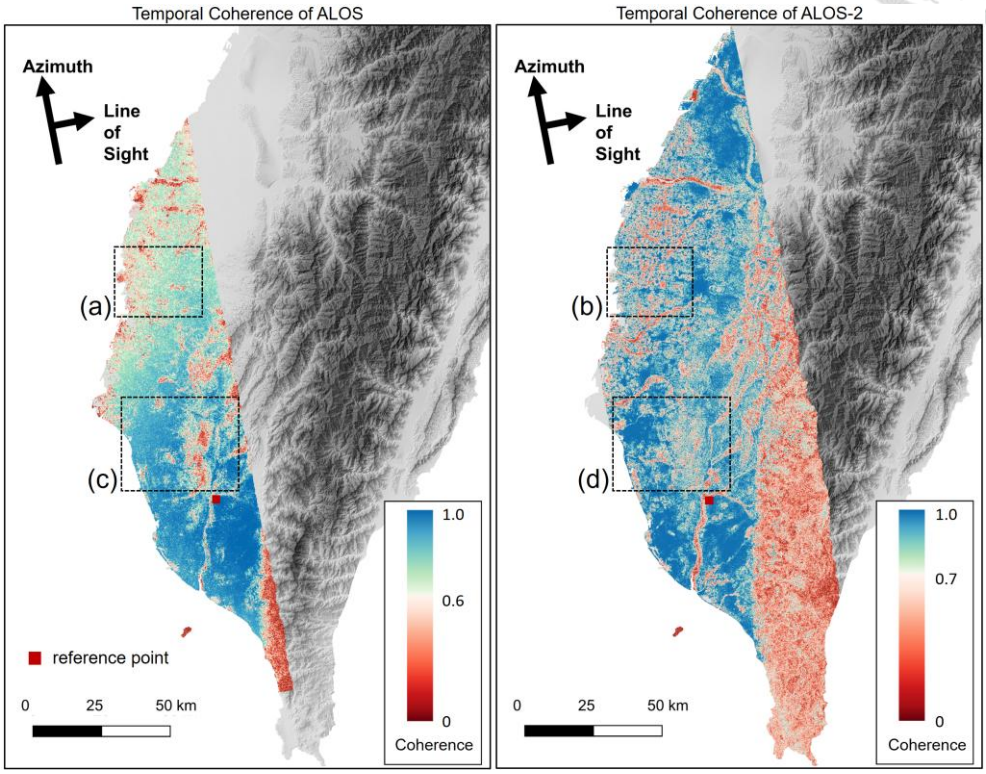

Figure 35. Temporal coherence map of ALOS (left panel) and ALOS-2 (right panel).

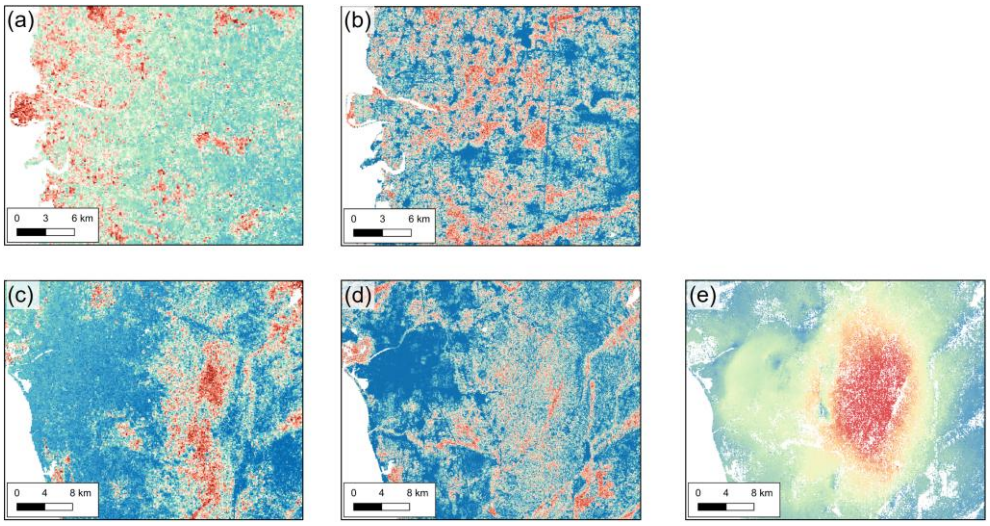

Figure 36. (a) and (b) show the difference between ALOS and ALOS-2 in the northern part of the study region. (e) is the coseismic displacement map from Figure 37, highlighting similarity with the decorrelated region in (d).

doi: 10.6342/NTU202500538

5.1.2. Coseismic and Interseismic Deformation

The InSAR time series processed using ISCE and Mintpy, with ionospheric and tropospheric corrections applied, are shown in the two maps on the top panels of Figure 37. ALOS and ALOS-2 have similar radar LOS geometries, resulting in comparable trends in LOS direction velocities for both time series. The Zhuoshui River alluvial plain and the coastal areas of Pingtung show land subsidence, producing signals moving away from the satellite on LOS direction. In the central and southern parts of the study area, tectonic activity drives southwestward deformation trends, leading to relatively high deformation rates towards the satellite on the LOS direction.

The ALOS-2 dataset includes 2 SAR images taken before the 2016 Meinong earthquake and 10 taken afterward, allowing for the separation of coseismic deformation signals using the following calculation:

G=[ones(size(A2_t) A2_t A2_t>2016.098]; m=G\d;

The results of the separation are shown in the two maps on the bottom panels of Figure 37, where the coseismic uplift caused by the 2016 Meinong earthquake is represented in the InSAR displacement field as LOS direction signals moving closer to the satellite.

doi: 10.6342/NTU202500538

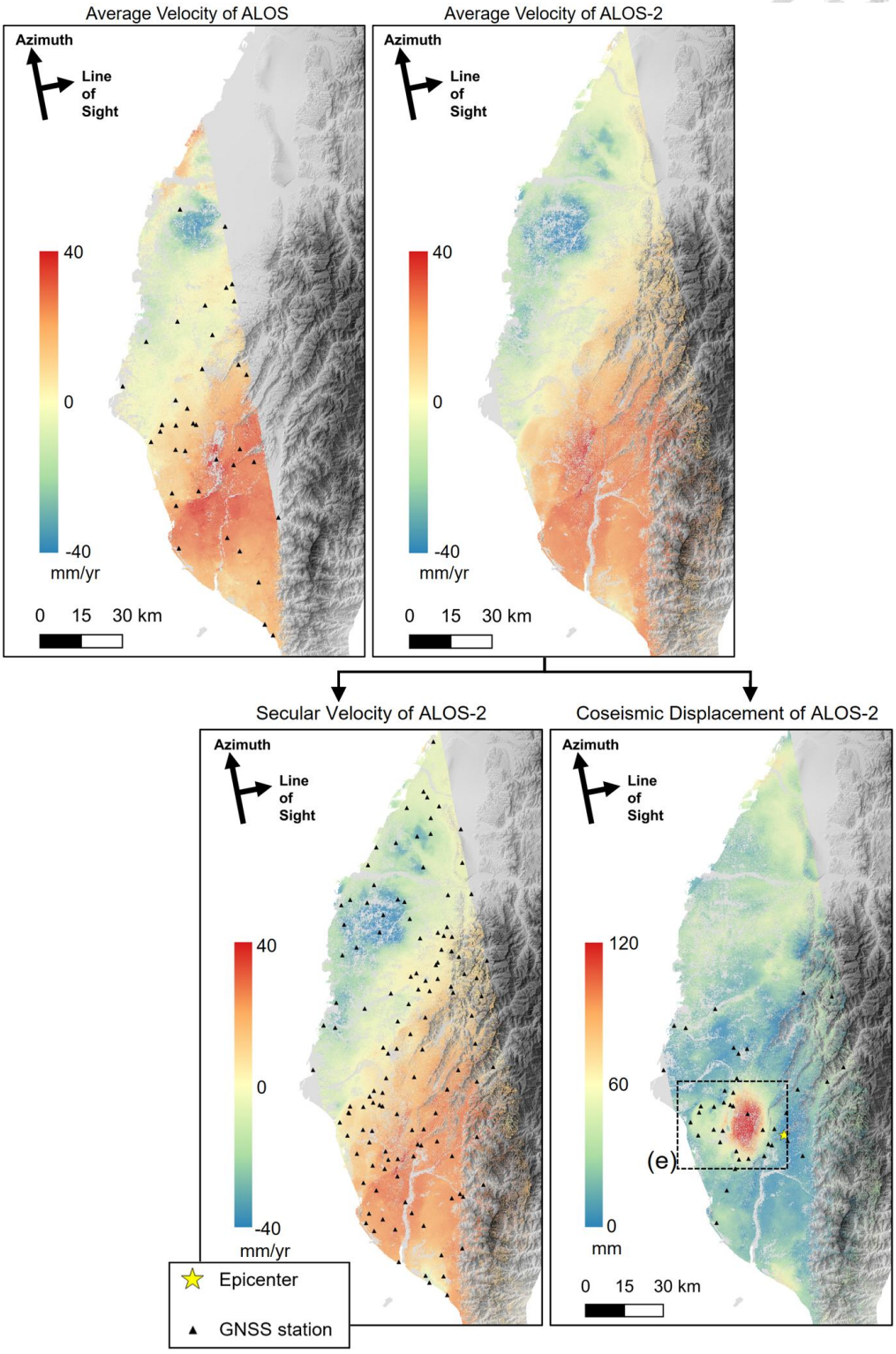

Figure 37. The two maps on the top show the average velocities of the ALOS and ALOS-2 time series, respectively. The bottom maps display the derived secular velocity and coseismic displacement from the 2016 Meinong earthquake. The yellow star on the coseismic displacement map marks the epicenter of the 2016 Meinong earthquake.

doi: 10.6342/NTU202500538

5.1.3. Error Distribution

To validate the estimation of secular velocity and coseismic displacement, the SE of time series fitting for each pixel was calculated based on the definition introduced in Section 4.5, as shown in Figure 38.

The error distribution for the ALOS dataset in the northern region is similar to the low coherence area described in Section 5.1.1. Additionally, the strip of higher error in the southern region might be due to stitching issues when mosaicking the raw SLC image frames. In the coastal area of Pingtung, where severe land subsidence is occurring, high SEs are observed, likely reflecting the impact of this subsidence.

For the average velocity map of ALOS-2, the majority of high-error pixels are concentrated in the central region of the study area, east of Tainan City. This concentration of error is likely due to the coseismic displacement from the 2016 Meinong earthquake. After incorporating the coseismic step into the model, the error in this central region can be significantly mitigated. Similar to the ALOS dataset, ALOS-2 also exhibits higher error in the northern region around Yunlin and Chiayi, as well as in the coastal region of Pingtung.

Figure 39 illustrate the relationship between velocity and SE for each pixel in the study area, revealing variations in data reliability across different velocity ranges. In the both datasets, the group of point with velocities lower than 10 mm/yr exhibit slightly higher SEs compared to the higher-velocity points higher than 10 mm/yr. This agrees with the trend observed in the lower-velocity region like the Zhuoshui River alluvial plain and the coastal areas of Pingtung. The overall SE in ALOS-2 is lower than in ALOS, suggesting an improvement in data reliability, with the majority of ALOS-2 SEs are lower than 4 mm/yr. Points with SEs above 4 mm/yr appear primarily in regions impacted by significant coseismic activity. In the right panel, the higher residual values correspond to

doi: 10.6342/NTU202500538

greater coseismic deformation, and a clear trend suggests that including coseismic events reduces SE, especially in regions with notable seismic impact.

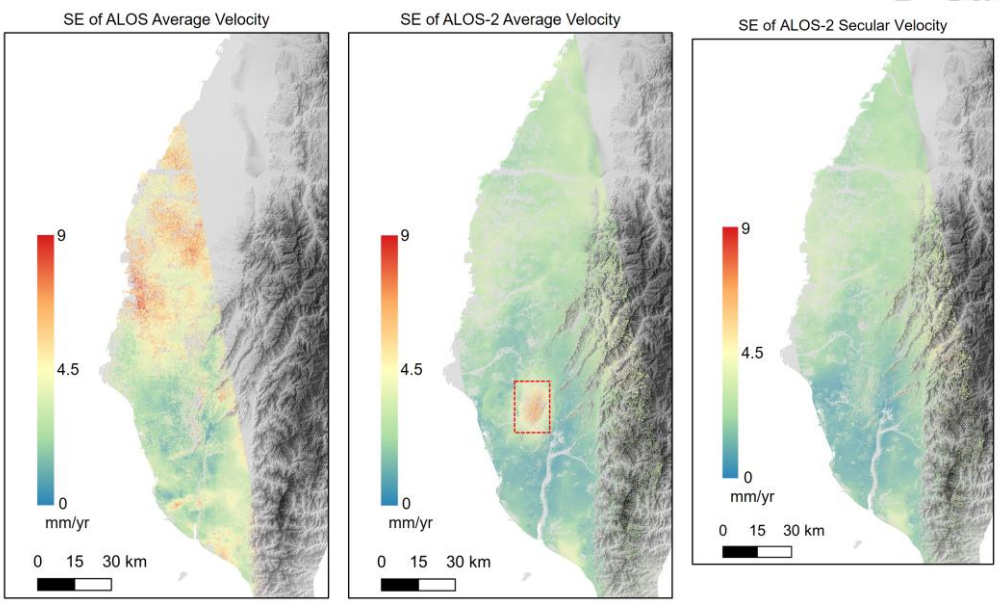

Figure 38. Spatial distribution of SE in velocity estimation for the ALOS (left panel) and ALOS-2 (middle panel) time series. By considering the coseismic deformation into the model, the SE of ALOS-2 secular velocity (right panel) can mitigate the effect of the coseismic deformation.

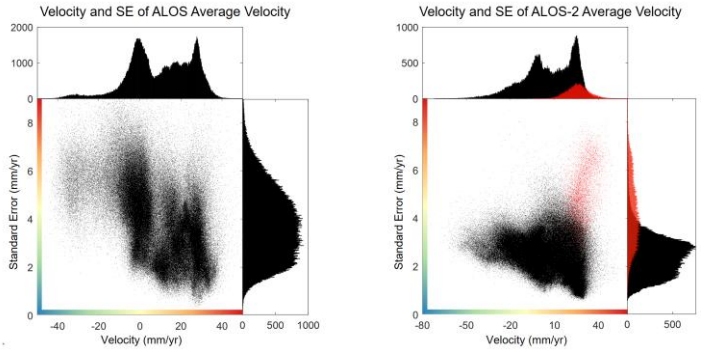

Figure 39. The relationship between velocity and standard error (SE) for each pixel. The left and right panels show ALOS and ALOS-2 average velocities, respectively. Red points represent data from the red box in Figure 38, with their count in the histograms amplified by a factor of 10 for clarity.

doi: 10.6342/NTU202500538

5.1.4. Validation with GNSS

The dense GNSS network in Southwestern Taiwan helps verify the accuracy of InSAR data. During the ALOS period, 37 stations provided data, increasing to 127 stations for the ALOS-2 period. Additionally, 41 stations recorded deformation from the 2016 Meinong earthquake. The GNSS-InSAR velocity comparison in Figure 40 reveals a strong correlation, with coefficients exceeding 0.90 for all components.

This high correlation is largely due to the distinct velocity patterns in the study area. The InSAR ascending LOS velocity map shows a clear velocity gradient, with significant subsidence in the north and high tectonic deformation in the south. To better understand the relationship between GNSS and InSAR data, both datasets were detrended using a 3rd-order polynomial.

Figure 41 displays the detrended result. After detrending, the correlation worsens for both datasets, with the ALOS correlation coefficient dropping below 0.5. Figure 42 highlights the velocity differences between the detrended maps. Differences exceeding 10 mm/yr are primarily observed in northern agricultural areas, mountainous regions, and Pingtung's coastal areas. These regions correspond to areas of low temporal coherence (Section 5.1.1) and high standard error (Section 5.1.3).

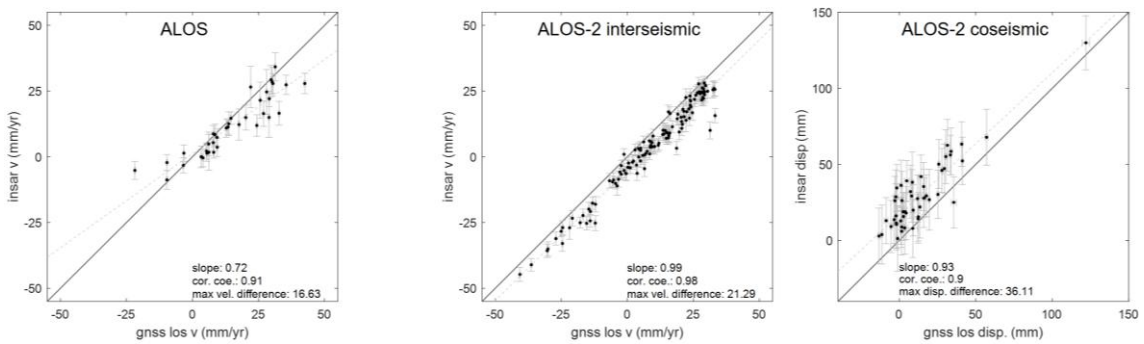

Figure 40. Comparison of LOS velocities and displacements between GNSS stations and InSAR observations. Error bars indicate one standard deviation of the velocity estimation. The spatial distribution of the GNSS stations is shown in Figure 37.

doi: 10.6342/NTU202500538

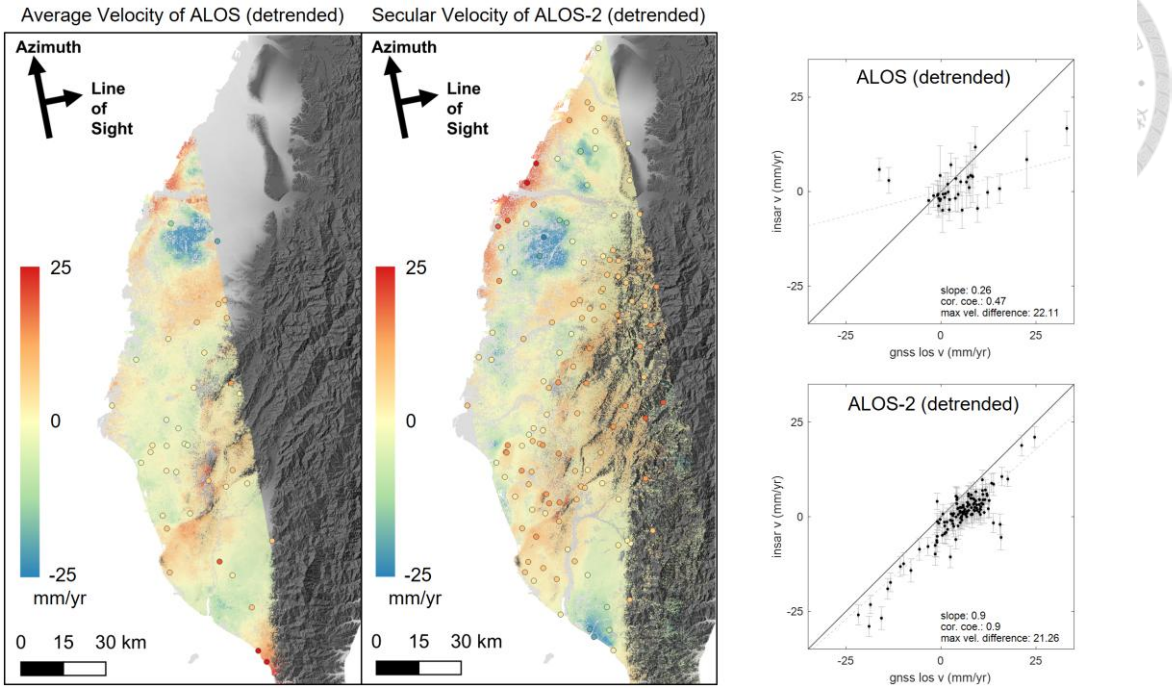

Figure 41. Detrended velocity maps and corresponding comparison plots. LOS velocities derived from GNSS stations are shown as color-coded circles on the maps, using the same color scale as the InSAR results. Error bars in the comparison plots represent one standard deviation.

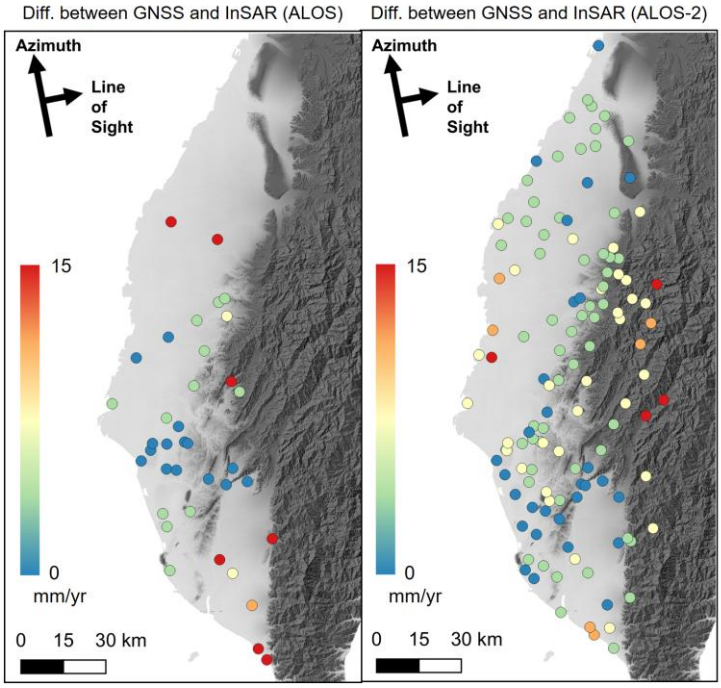

Figure 42. Maps showing the differences in LOS velocity between GNSS stations and InSAR observations.

doi: 10.6342/NTU202500538

5.2. Velocity Difference between Two InSAR Datasets

To make the interseismic deformation rates between the two InSAR datasets comparable, the primary task here is to equalize the radar LOS geometries of two satellites. In this study, I applied a straightforward project method to convert the LOS velocity field of the ALOS satellite to match the LOS direction of the ALOS-2 satellite. By using the 3D velocity components from continuous GNSS stations, I projected the GNSS 3D velocities into the LOS geometries of both ALOS and ALOS-2 separately. The residual between these two projections was assumed to be very similar to the difference in LOS geometries between the two InSAR datasets. Subtracting this residual map from the ALOS velocity map results in an ALOS velocity field effectively "projected" into the ALOS-2 LOS geometry.

The resulting velocity difference map, shown in Figure 44, illustrates the changes in deformation rates between the two datasets. This map reveals areas where acceleration occurred, with red pixels indicating regions that have experienced an increase in deformation rate between the ALOS and ALOS-2 periods.

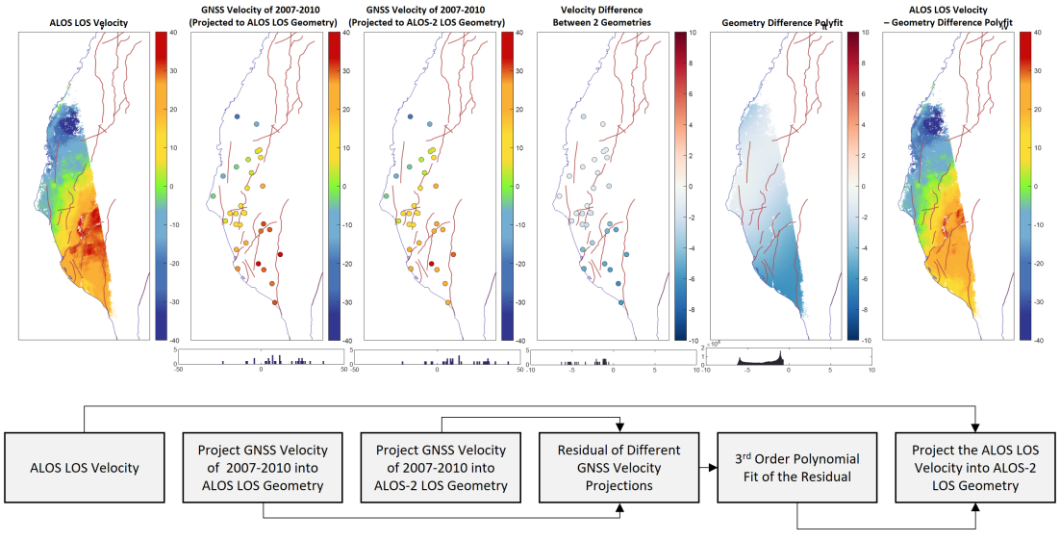

Figure 43. The workflow of projecting ALOS LOS velocity into the radar geometry of ALOS-2 LOS.

doi: 10.6342/NTU202500538

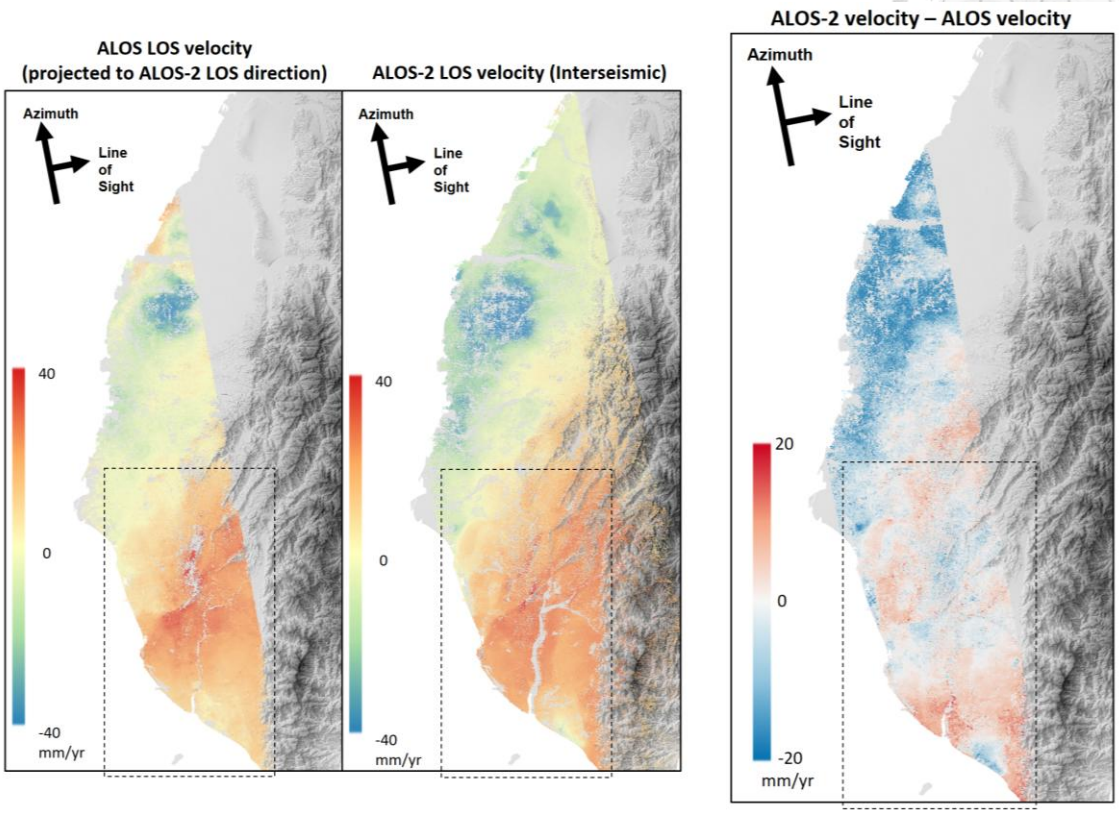

Figure 44. The comparison of the interseismic velocity maps of two SAR observations.

doi: 10.6342/NTU202500538

5.3. Mapping the Velocity Boundaries

Focusing on the region between the Hsinhua Fault and the Pingtung Plain, numerous boundaries on the residual map suggest potential creeping events along shallow active structures. Based on the maps shown in the Figure 45, I manually identified boundaries with detectable velocity discontinuities. In total, 15 boundaries were identified, some of which correspond to previously known shallow active structures such as the Houchiali Fault, Hsiaokangshan Fault, Youchang Fault, and Lungchuan Anticline. On the other hand, boundaries like Gangshan Boundary, Pingtung Boundary, and Fangliao Boundary have received less attention in previous studies, highlighting that many shallow active structures in southwestern Taiwan remain poorly understood.

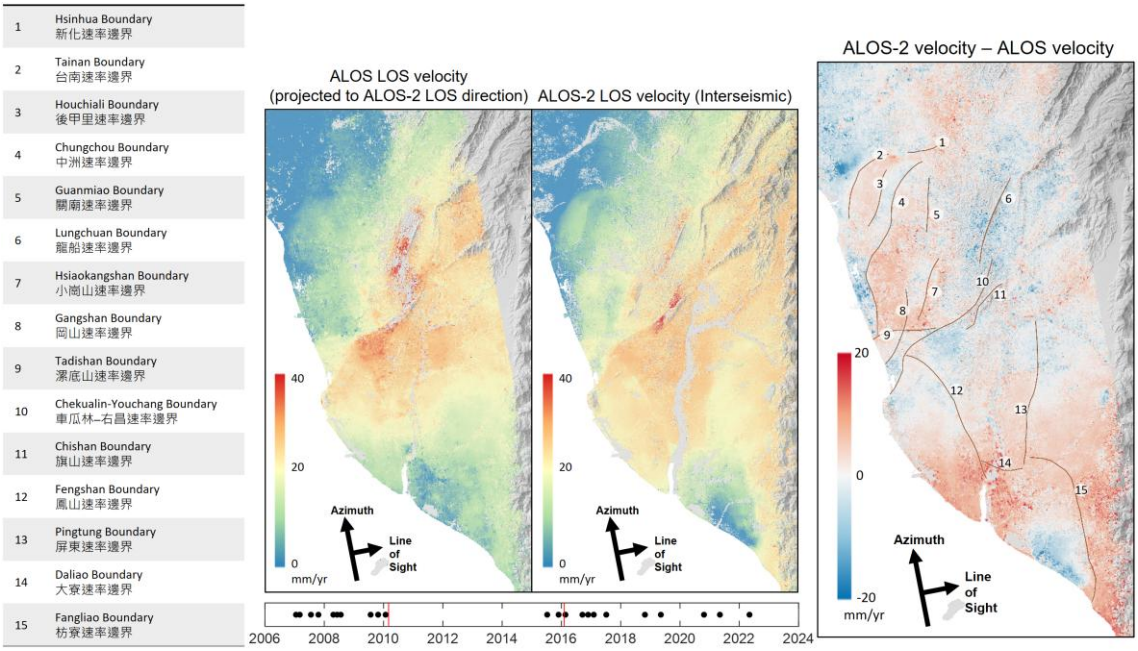

Figure 45. The zoomed in maps of the interseismic velocity maps in Figure 44. Fifteen boundaries were identified in this study by the velocity discontinuous features on the maps.

doi: 10.6342/NTU202500538

5.4. Profiles of InSAR, Leveling, and Topography

As mentioned in the Section 4.2, five leveling profiles across active structures in the study area. In this section, the leveling velocity profiles were compared to the InSAR, GNSS, and topography data. By overlaying these geodetic datasets along each profile, this study analyzes how the velocities change along the previous mapped boundaries.

5.4.1. The Shanhua – Guanmiao Profile

The first profile extends from Shanhua to Guanmiao, running north-south across the Hsinhua Boundary. Between 2006 and 2010, no significant near-field velocity difference is observed across the boundary in either the leveling or ALOS InSAR profiles. However, between 2015 and 2022, a near-field velocity difference becomes evident, measuring approximately 2 mm/yr on the leveling profile and around 6.3 mm/yr on the ALOS InSAR profile. These observations suggest that the Hsinhua Boundary may represent a shallow active structure that was locked during 2006–2010 and exhibited creeping behavior between 2015 and 2022, predominantly with a strike-slip component.

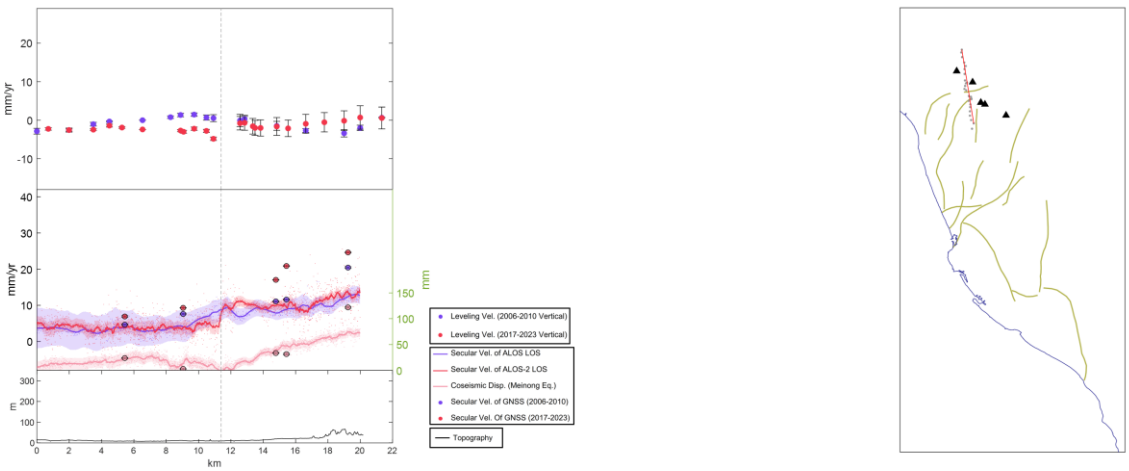

Figure 46. Profile of vertical leveling velocity, GNSS and InSAR LOS velocity, and topography along a transect from Shanhua to Guanmiao.

doi: 10.6342/NTU202500538

5.4.2. The Anping – Longpi Profile

The second profile, spanning about 35 km, extends from Anping to Longpi, crossing the Tainan Tableland and Lungchuan Anticline. This profile intersects five boundaries, three of which (Tainan Boundary, Guanmiao Boundary, and Lungchuan Boundary) exhibit coseismic slip as a result of the 2016 Meinong earthquake. Active structures across the Tainan Tableland show higher creeping rates in 2015–2022, while the Guanmiao Boundary and Lungchuan Boundary display more activity during 2006–2010, followed by reduced creeping rates afterward. The Houchiali Boundary, however, does not show clear coseismic slip, though both the Houchiali Boundary and Chungchou Boundary exhibit entirely different slip behavior in the two time periods.

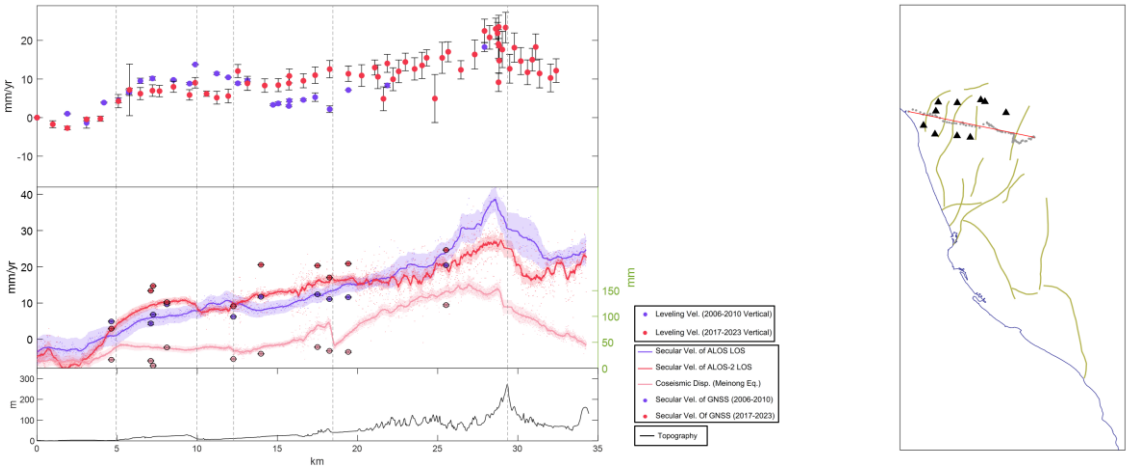

Figure 47. Profile of vertical leveling velocity, GNSS and InSAR LOS velocity, and topography along a transect from Anping to Longpi.

doi: 10.6342/NTU202500538

5.4.3. The Luzhu – Maolin Profile

The third profile runs from Luzhu to Maolin, crossing the Chungchou, Hsiaokangshan, Lungchuan, and Chekualin structures over a distance of approximately 50 km. The velocity difference across the Chungchou Boundary is around 13.1 mm/yr in the ALOS-2 InSAR profile and 9.7 mm/yr in the leveling profile for the period 2015–2022, while no notable near-field velocity difference is observed between 2006 and 2010. Although coseismic uplift exceeds 70 mm near the Guanmiao, Lungchuan, and Chekualin anticlines, no clear coseismic slip is detected in the coseismic deformation map. Both leveling and InSAR profiles suggest that the interseismic uplift to the west of the Lungchuan Anticline slowed down in the later period.

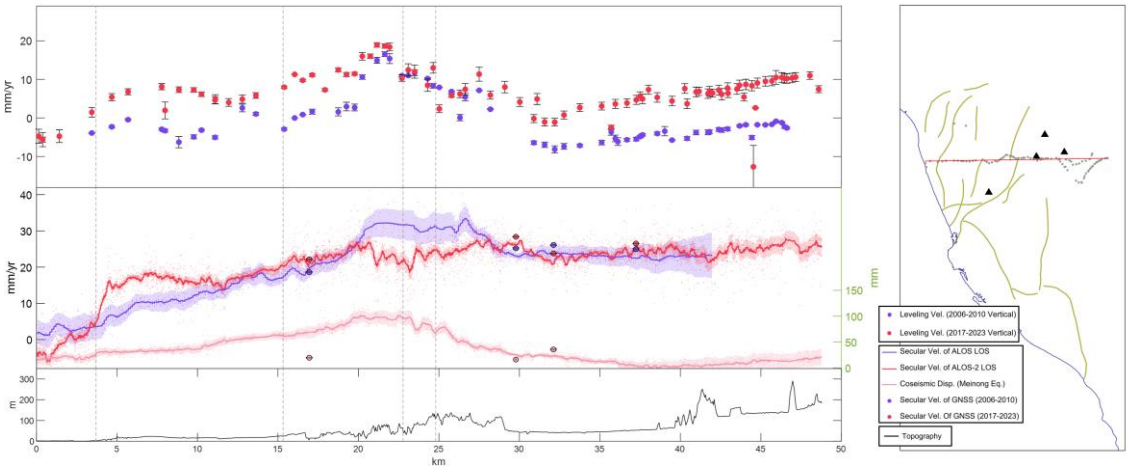

Figure 48. Profile of vertical leveling velocity, GNSS and InSAR LOS velocity, and topography along a transect from Luzhu to Maolin.

doi: 10.6342/NTU202500538

5.4.4. The Gangshan – Anpo Profile

The fourth profile, the Gangshan–Anpo line, crosses the Chekualin–Youchang Boundary and Chishan Boundary, while the leveling measurements follow a meandering route across the Hsiaokangshan Boundary. The fourth and fifth leveling points from the west show a consistent velocity difference across the Hsiaokangshan Fault in both time periods, indicating ongoing tectonic activity. Around the Chekualin and Chishan areas, the uplift patterns differ between the two profiles, likely because the leveling and InSAR profiles are not perfectly aligned, with a few kilometers of separation between them. The rapid uplift observed in the InSAR profile is localized and mainly noticeable near the Zhongliao Tunnel area.

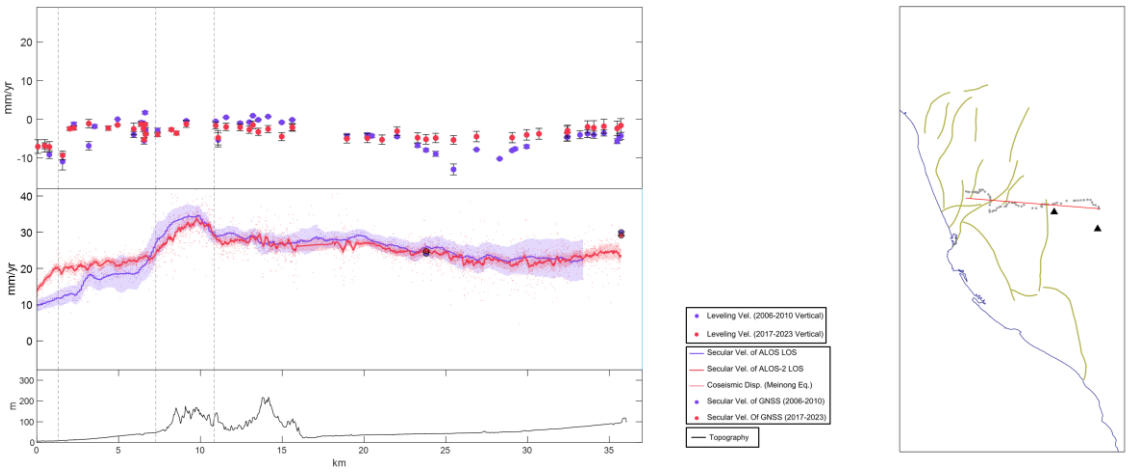

Figure 49. Profile of vertical leveling velocity, GNSS and InSAR LOS velocity, and topography along a transect from Gangshan to Anpo.

doi: 10.6342/NTU202500538

5.4.5. The Jiadong – Qijia Profile

The fifth profile is located along the southeastern edge of the Pingtung Plain. Both leveling and InSAR measurements indicate a consistent transient event, with a velocity discontinuity of 8–10 mm/yr across the Fangliao Boundary over the two time periods. Although there is no clear topographic evidence to support the classification of the Fangliao Boundary as an active structure, the consistent findings from leveling and InSAR strongly suggest the presence of an active structure.

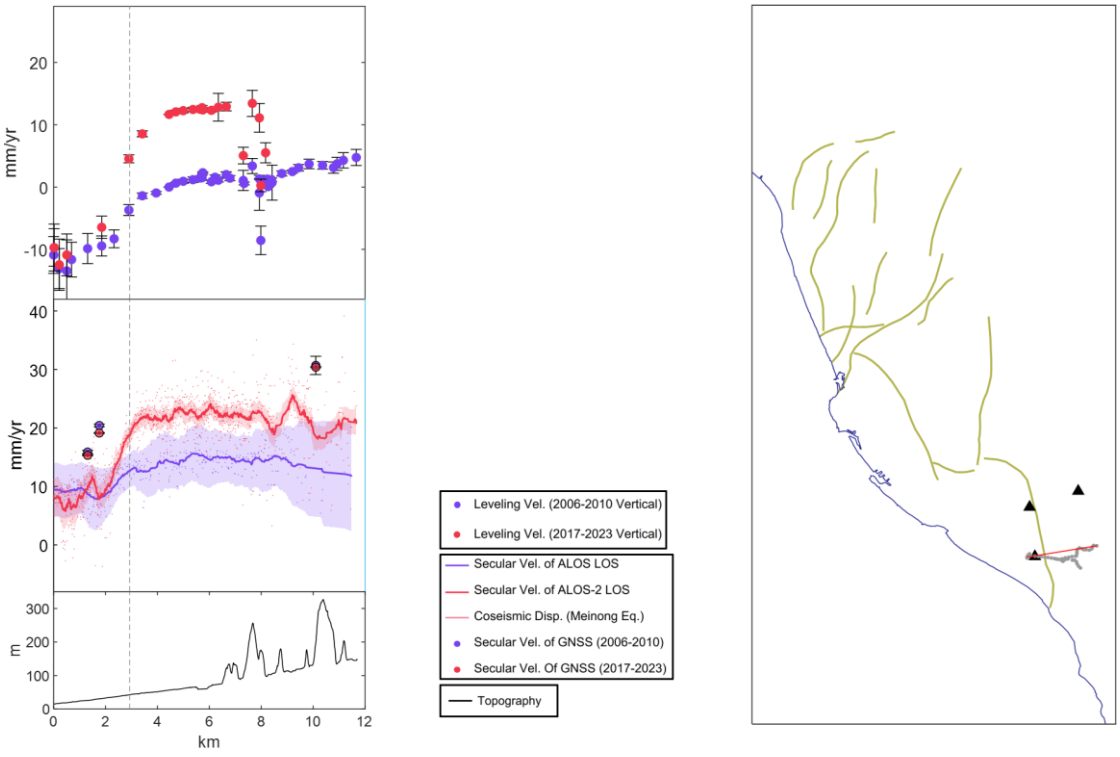

Figure 50. Profile of vertical leveling velocity, GNSS and InSAR LOS velocity, and topography along a transect from Jiadong to Qijia.

doi: 10.6342/NTU202500538

Chapter 6 Discussion

6.1. Data Limitations and Processing Challenge

Due to the long revisit interval of SAR satellite, the temporal baselines of the SAR imagery used in this study are long. Specifically, ALOS imagery had a maximum interval of 184 days, while ALOS-2 imagery extended to an impressive 364 days. By using the Small Baseline Subset (SBAS) method, the number of interferograms can be maximized, and the most information from each image can be extracted.

Ionospheric effects were another significant challenge, particularly for L-band data like ALOS and ALOS-2. The widely used Range Split Spectrum (RSS) method was employed for ionospheric correction but exhibited limitations, particularly for the noisier ALOS data. As noted by many previous studies (e.g. Rosen et al., 2010; Jung et al., 2012), the RSS method is highly sensitive to noise, which complicated its application to ALOS imagery. The relatively lower image quality of ALOS compared to its successor, ALOS-2, made this issue even more challenging to address.

To overcome this, the study employed the GInSAR method, which uses GNSS station data to estimate and correct ionospheric phases. Figure 51 (top) shows examples of GInSAR-corrected ALOS interferograms. In one example, the ALOS 2007/01/17–2009/07/25 interferogram exhibited noticeable streaks. Despite these artifacts, the correlation between the corrected results and GNSS measurements was relatively strong, justifying its inclusion in the analysis. Conversely, the ALOS 2007/01/17–2008/06/06 interferogram did not show significant improvement after GInSAR correction and was therefore excluded from further study.

For ALOS-2 data, GInSAR and RSS corrections produced similar results, as illustrated in Figure 52 (bottom). The ALOS-2 2019/05/09–2022/05/05 interferogram showed very good correlation between GNSS and InSAR velocity rates after GInSAR

doi: 10.6342/NTU202500538

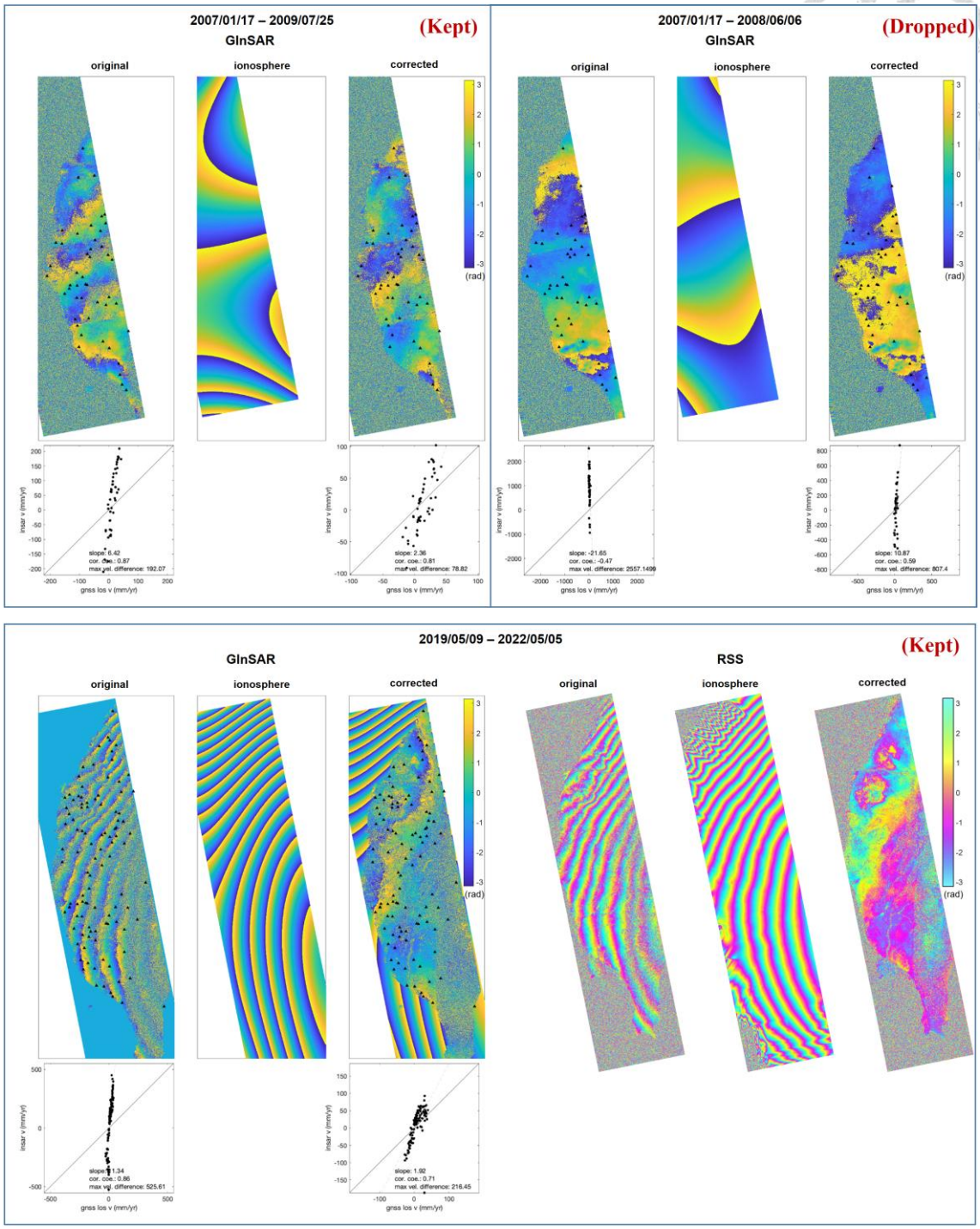

Figure 51. The example interferograms of ALOS (top) and ALOS-2 (bottom). For each examples, the original interferograms, estimated ionospheric phase, and corrected results are shown. Black triangles in the GInSAR examples exhibited the distribution of GNSS stations with data available during the same time period.

doi: 10.6342/NTU202500538

correction. Moreover, the ionospheric phase pattern derived using GInSAR closely matched the one estimated through the RSS method, validating the reliability of both approaches for ionospheric phase correction in SAR imagery.

An interesting finding was that, for ALOS data, results without tropospheric delay corrections performed better than those using three tested models (refer to Figure 34). Unlike RSS, GInSAR cannot target only the dispersive components of the interferometric phase for correction. This limitation means that when GInSAR is used, non-dispersive components such as tropospheric delays, which are influenced by water vapor distribution, weather conditions, and topography, remain uncorrected. In this study, GInSAR-corrected ALOS data introduced additional complexities that made subsequent tropospheric corrections ineffective, as the residual tropospheric phase could not be reliably isolated.

In summary, this study successfully addressed ionospheric effects using GInSAR for ALOS data and RSS for ALOS-2 data, demonstrating both methods as viable approaches for ionospheric correction. These corrections improved the accuracy of surface deformation estimates and provided a strong basis for analyzing tectonic structures and fault activity.

doi: 10.6342/NTU202500538

6.2. Toward 3D Surface Deformation Mapping

This section presents an initial attempt to calculate three-dimensional surface deformation rates by combining ascending InSAR data from this study, descending InSAR data from Lee (2024), and GNSS-derived north-south velocity fields. The results reveal interesting deformation patterns in the east-west and vertical direction velocity fields. These findings highlight the potential for further exploration to understand the complex tectonic behaviors in this region.

The descending InSAR datasets provided by Lee (2024) are MT-InSAR time series from Envisat and Sentinel-1 processed with ISCE and Mintpy software. The descending LOS deformation patterns exhibit significant differences from those observed in the ascending LOS results derived from my ALOS and ALOS-2 ascending datasets, reflecting the complex deformation behaviors within the study area. These differences highlight the limitations of relying on a single satellite's viewing geometry to comprehensively capture surface deformation processes.

The Envisat data, spanning from 2006 to 2008, partially overlaps with my ALOS observations. Envisat's azimuth angle is approximately 164°, with an incidence angle ranging from 22° to 25°. Meanwhile, the Sentinel-1 data spans from 2014 to 2023, closely align with my ALOS-2 observations. Sentinel-1's azimuth angle is approximately 169°, with an incidence angle ranging from 40° to 42°.

To better constrain the ground deformation in the north-south direction and avoid an underdetermine scenario, I used continuous GNSS stations to interpolate the north-south velocity across the study area. The resulting velocity field is illustrated in Figure 52. Taking advantage of the temporal overlap between InSAR datasets, I decomposed the LOS velocities from both ascending and descending orbits into three-dimentional components: north-south, east-west, and vertical directions.

doi: 10.6342/NTU202500538

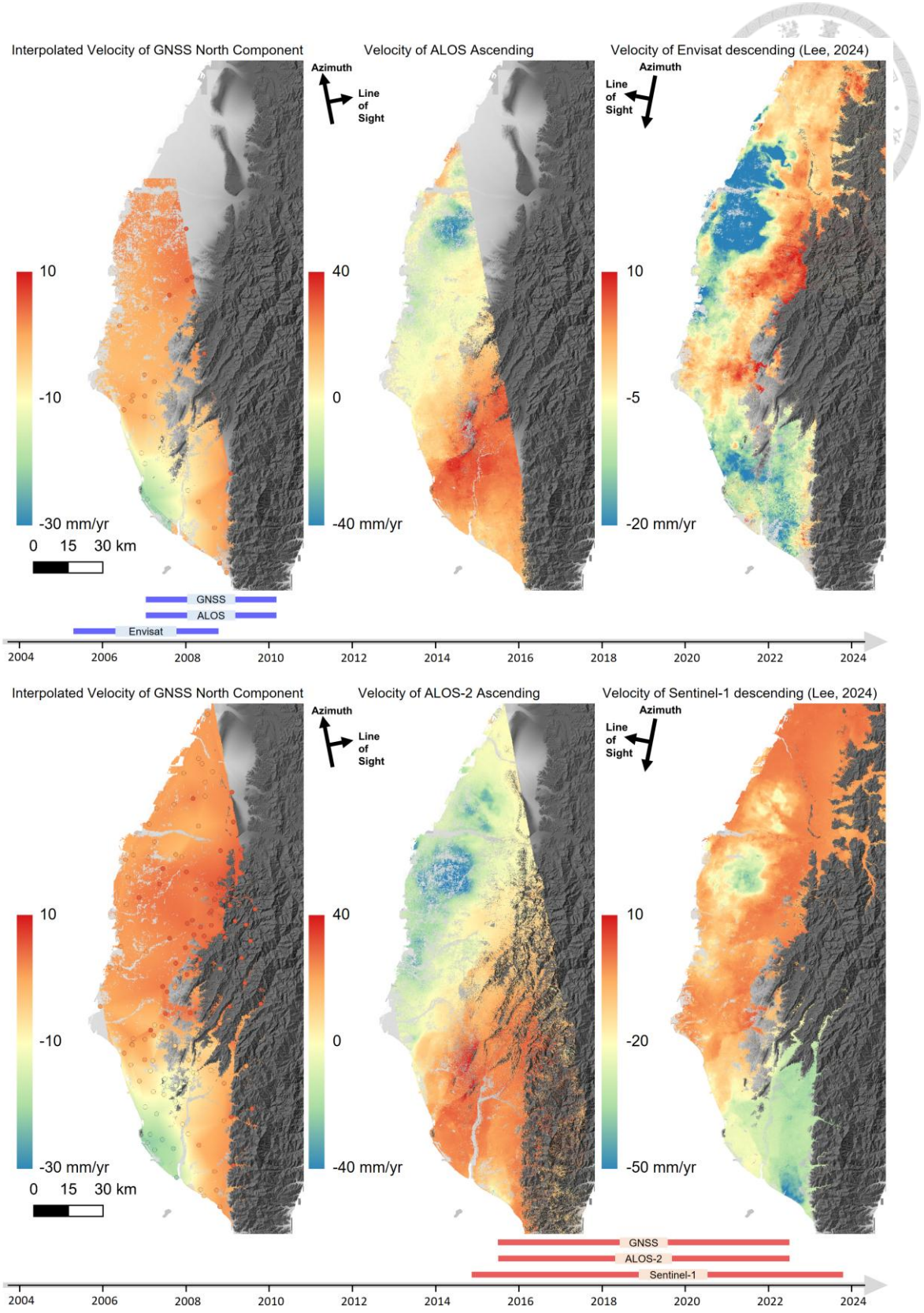

Figure 52. Data sources for 3D inversion calculation.

doi: 10.6342/NTU202500538

For a given pixel in the InSAR velocity map, the 3D velocity components V_N, V_E, and V_U can be derived from the two LOS velocities V_{asc} and V_{des} . Specifically, the observation vector and design matrix are defined as:

$$d = \begin{bmatrix} V_{GNSS\_n} \\ V_{asc} \\ V_{des} \end{bmatrix}, \qquad G = \begin{bmatrix} 1 & 0 & 0 \\ G\_asc_N & G\_asc_E & G\_asc_U \\ G\_des_N & G\_des_E & G\_des_U \end{bmatrix}$$

Where the geometry coefficients *G_asc* and *G_des* represent the components of the LOS vectors for the ascending and descending tracks in the north, east, and vertical directions. To account for measurement uncertainties, the weighting matrix is constructed:

$$W = \begin{bmatrix} (Err_{GNSS\_n})^{-2} & 0 & 0 \\ 0 & (Err_{asc})^{-2} & 0 \\ 0 & 0 & (Err_{des})^{-2} \end{bmatrix}$$

By applying a weighted least squares approach, the 3D velocity vector V and the covariance matrix *cov* can be obtained via

$$V=(G^T W G)^{-1} A^T W d, \qquad cov=(G^T W G)^{-1}$$

Once the velocity components are solved, the standard errors in V can be expressed as:

$$SE=(diag(cov))^{0.5}$$

The LOS velocity errors for the ALOS and ALOS-2 datasets are referenced in Section 5.1.3. For this analysis, the errors for the Envisat and Sentinel-1 datasets are assumed to be identical to those of the ALOS and ALOS-2 datasets, respectively. Additionally, the errors for the interpolated GNSS north-south velocities are assumed to correspond to the LOS difference between the GNSS and ascending InSAR results.

The decomposed result for the two time periods are illustrated in Figure 53 and Figure 54. The north-south deformation pattern is robust, but the vertical and east-west components clearly reveal distinct deformation patterns across various active structures. For instance, at the southern end of the Fengshan fault, the structure splits into three

doi: 10.6342/NTU202500538

segments: one dominated by east-west creeping motion and two by vertical motion. For the Youchang fault, intersected by the Fengshan fault, east-west creeping dominates the northern section, while vertical motion is prominent in the south. These insights underscore the value of three-dimensional decomposition in capturing complex deformation features.

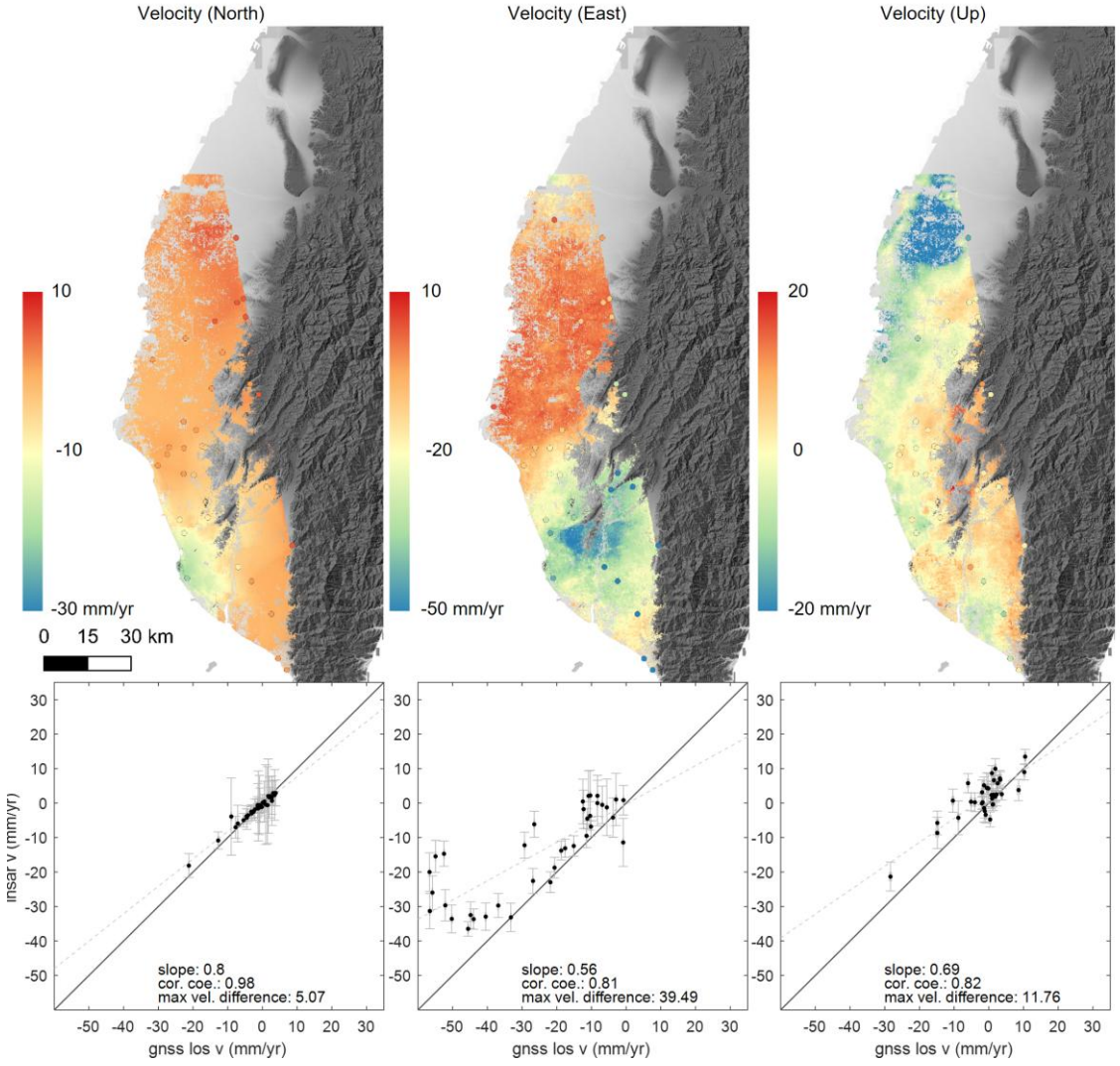

Figure 53. The top three maps illustrate the north-south (N), east-west (E), and vertical (U) velocity fields derived from descending Envisat InSAR (2006-2008) and ascending ALOS InSAR (2007-2010). The location and velocity of GNSS stations are plotted on the map. And the bottom three plots represent the relationship between the 3D velocity field and GNSS velocities, with error bar represents the standard error.

doi: 10.6342/NTU202500538

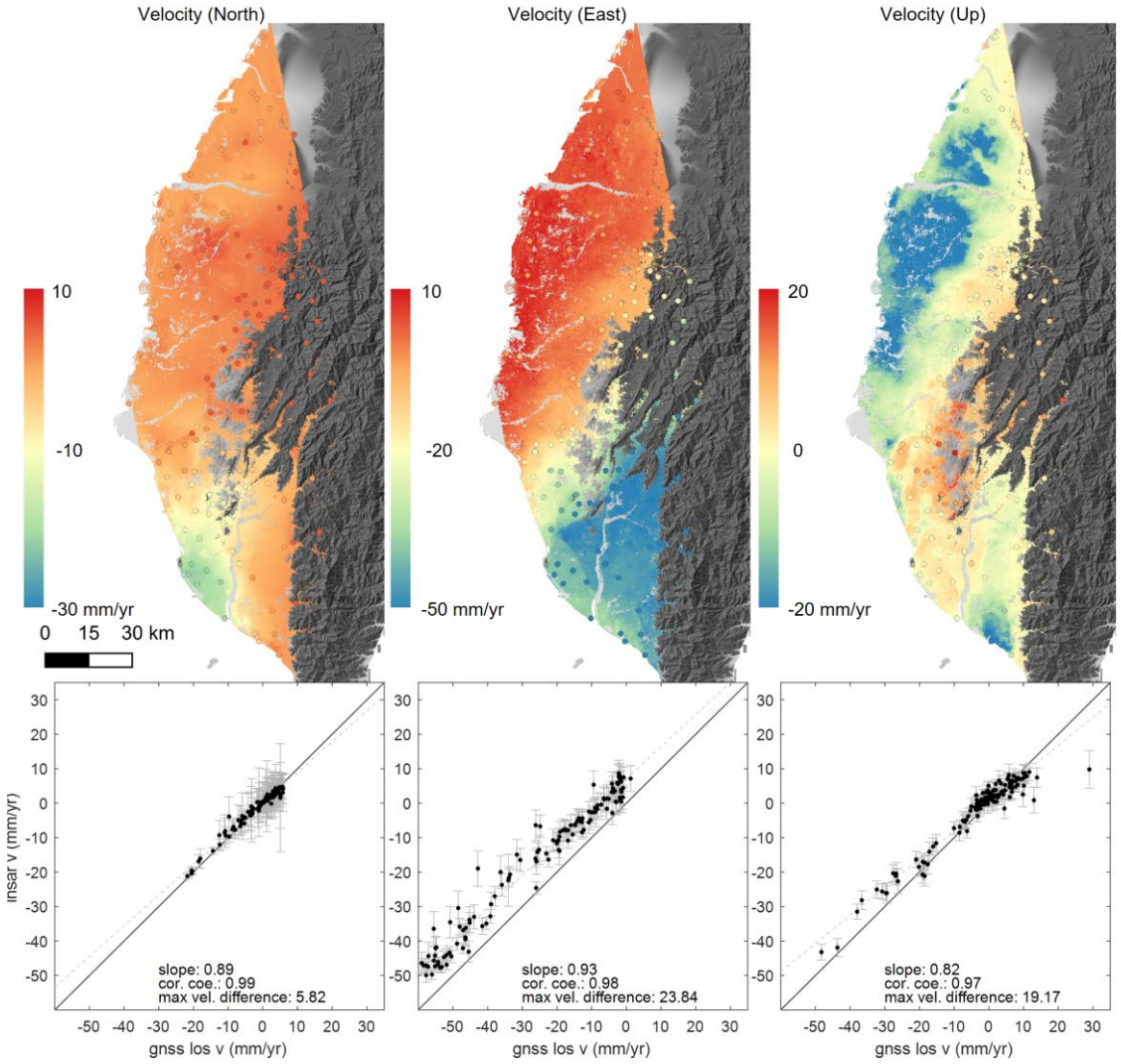

Figure 54. The top three maps illustrate the north-south (N), east-west (E), and vertical (U) velocity fields derived from descending Sentinel-1 InSAR (2014-2023) and ascending ALOS-2 InSAR (2015-2022). The location and velocity of GNSS stations are plotted on the map. And the bottom three plots represent the relationship between the 3D velocity field and GNSS velocities, with error bar represents the standard error.

doi: 10.6342/NTU202500538

6.3. Comparison of Observed and Previous Fault Structures

6.3.1. The Fault Trace of The Chungchou Fault

The activity of the Chungchou Fault shows clear differences between the ALOS (2007–2010) and ALOS-2 (2015–2022) time periods. During the ALOS period, the fault shows very little activity, with no significant deformation patterns detected. However, in the ALOS-2 period, a noticeable uplift is observed on the eastern side of the fault, as shown in Figure 55. Leveling profiles from Figure 47 and 48 confirm that the fault was largely inactive between 2006 and 2010. In contrast, during 2017–2023, the interseismic deformation rate shows an uplift of approximately 4.5 mm/yr along the northern section of the fault, which is parallel to the Houchiali Fault, and about 6.1 mm/yr along the southern section, which is parallel to the Hsiaokangshan Fault.

The coseismic deformation from the 2016 Meinong earthquake shows significant slip on faults related to the Tainan and Lungchuan anticlines, but no clear coseismic deformation is observed along the Chungchou Fault. Although it did not show notable coseismic deformation, its interseismic slip rate increased significantly after the earthquake, indicating a possible change in fault activity triggered by the event. This suggests that the Chungchou Fault behaved differently during the earthquake.

The relationship between the southern end of the Chungchou Fault and the Chihkan Structure is also worth noting. Previous studies, such as those by Hsu and Chang (1979), Lacombe et al. (1999), and Hu (2025), identified flexural scarps around Tadishan as part of a separate fault system, called the Chihkan Fault. However, neither the ALOS nor ALOS-2 velocity fields show clear evidence of activity along the Chihkan Fault. I propose that the southern end of the Chungchou Fault is cut off by the Tadishan Fault, a right-lateral fault identified by Ching (2017) using InSAR data. The Chihkan Fault south of Tadishan may represent a remnant of the Chungchou Fault's activity before it was cut.

doi: 10.6342/NTU202500538

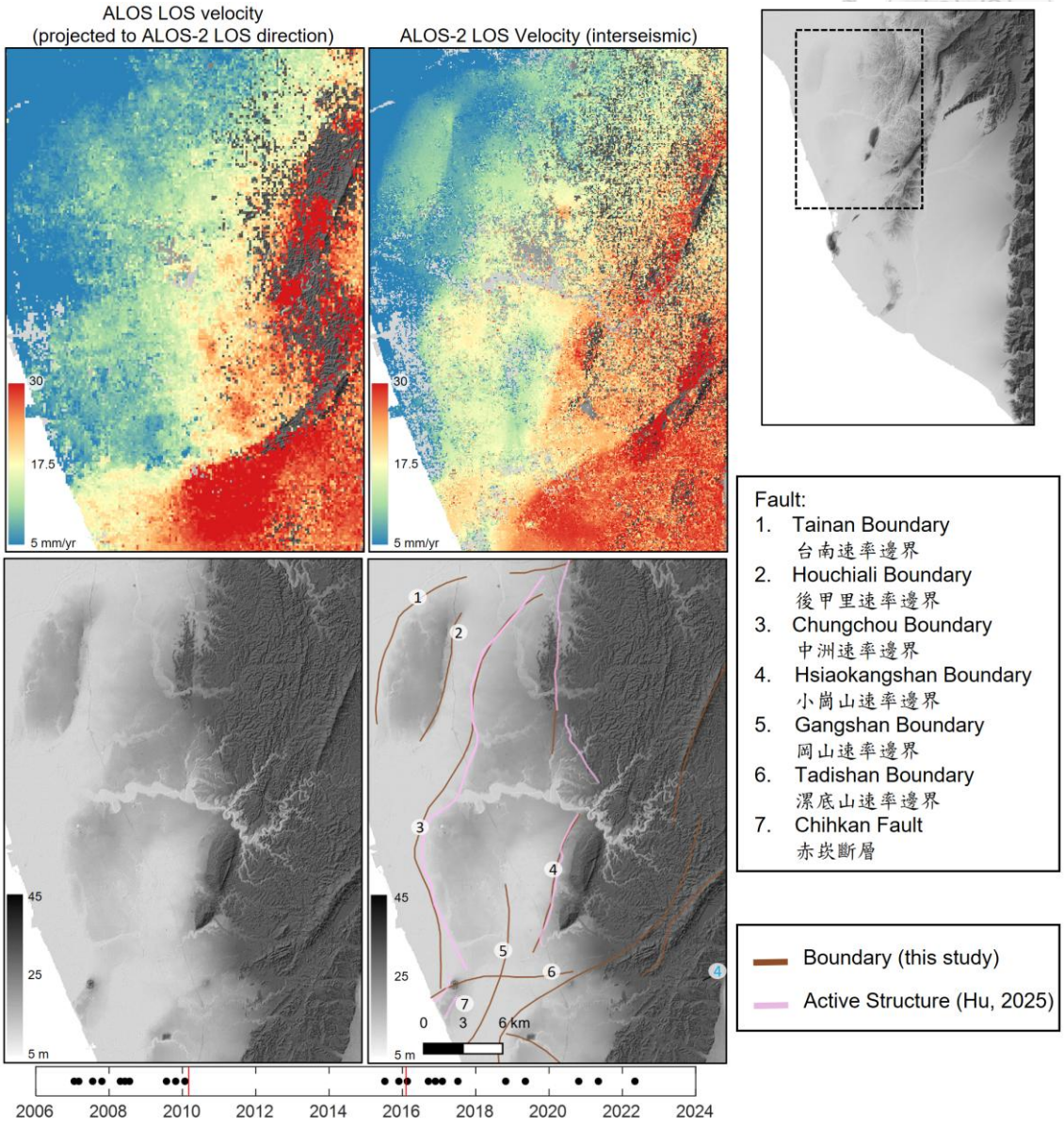

Figure 55. Zoomed in maps of two interseismic velocity fields. The bottom-right map highlights the Tainan, Houchiali, Chungchou, Hsiaokangshan, Gangshan, Tadishan, and Chihkan boundaries/ faults.

doi: 10.6342/NTU202500538

6.3.2. Chekualin, Youchang, and Fengshan Faults

The Chekualin, Youchang, and Fengshan Fault are prominent shallow structures in Southwestern Taiwan. Using InSAR data, this study provides an updated evaluation of their interrelationships and behavior. Chen et al. (2010) used borehole data to propose that the Youchang Fault might connect with the Hsiaokangshan Fault. Chao (2016), employing ALOS InSAR data, mapped the Fengshan Fault as originating from the Youchang Fault in the north, extending southward across the Kaoping River into the Pingtung Plain. Tung (2021) further detailed the fault scarp distribution of the Youchang Fault, showing its northeastward extension to the Gunshuiping mud volcano.

The Chekualin-Youchang Boundary, as observed in the InSAR velocity maps, forms a continuous active fault approximately 31 km in length. This boundary likely connects the Chekualin Fault and Youchang Fault, creating a significant structural boundary across the study region. This interpretation aligns with the hypothesis of Tung (2021) that suggest the Youchang Fault may have a further northeastward extension.

However, based on the InSAR velocity field, the portion of the boundary previously identified as the Youchang Fault appears to be composed of two distinct fault segments, with the intersection point with the Fengshan Fault. The southern Youchang Fault extends from Shoushan to near National University of Kaohsiung (NUK), where it intersects the Fengshan Fault. The northern Youchang Fault continues from near National University of Kaohsiung toward the Gunshuiping mud volcano area, connecting with the Chekualin Fault and the Tadishan Fault.

The Fengshan Boundary presents a more complex structural pattern. Located to the south of the Chekualin-Youchang Boundary, it is characterized by velocity discontinuities and branching features observed in both ALOS and ALOS-2 deformation maps. The north

doi: 10.6342/NTU202500538

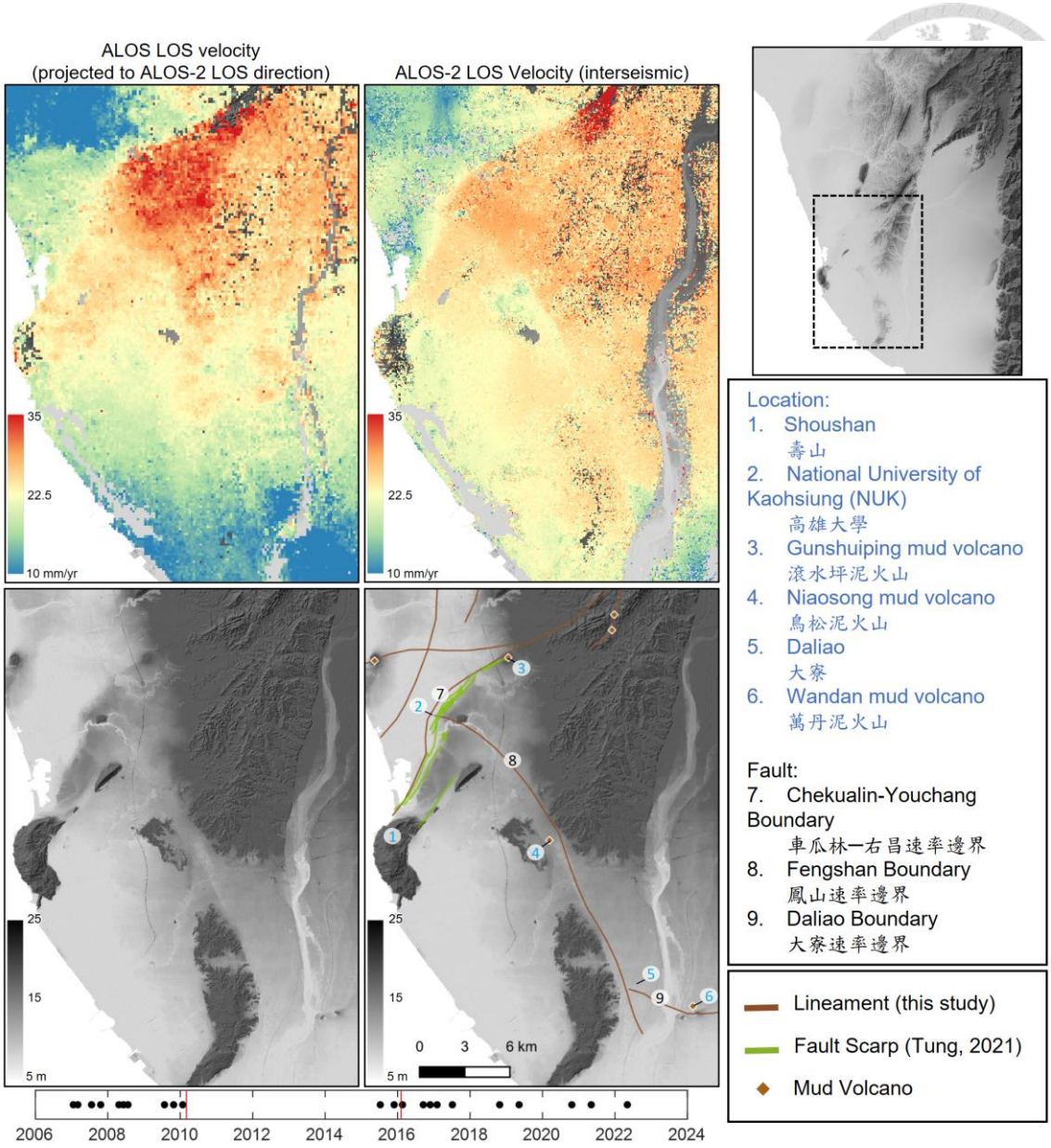

Figure 56. Zoomed in maps of two interseismic velocity fields. The bottom-right map highlights the Chekualin-Youchang, Fengshan, and Daliao boundaries, as identified in this study, alongside the locations of mud volcanoes: Gunshuiping, Niaosong, and Wandan.

doi: 10.6342/NTU202500538

-ern end of the Fengshan Boundary intersects with the Chekualin-Youchang Boundary. However, tracing its continuation further north remains challenging. The Spatial distribution of the Fengshan Boundary corresponds closely with that of the Fengshan Fault, where Sun (1964) first identified topographic scarps, and Shyu et al. (2005) described its left-lateral faulting features.

A notable correlation exists between the Fengshan Boundary and mud volcanoes, as illustrated in Figure 56. Near Daliao, the southern end of the Fengshan Boundary branches into two segments. One branch extends eastward, crossing the Kaoping River and reaching the Wantan mud volcano in Pingtung. This spatial overlap suggests a possible relationship between tectonic activity along the boundary and subsurface fluid movement, as proposed by Chao (2016). This updated interpretation integrates multiple pieces of evidences, offering a more comprehensive understanding of the activity of these shallow active faults.

doi: 10.6342/NTU202500538

6.3.3. Shallow Active Structures on the Pingtung Plain

Despite significant land subsidence in the southern coastal areas of the Pingtung Plain, several shallow active structures causing distinct velocity boundaries can still be identified across the plain.

The Pingtung Boundary is a north-south trending feature located on the eastern bank of the Kaoping River. It appears as a distinct velocity boundary in the ALOS-2 velocity field, extending from Wandan northward through Pingtung City before disappearing near the Ailiao River. In the Pingtung area, LOS velocities west of the boundary are 4–5 mm/yr higher than those to the east, with differences of 2–3 mm/yr near Wandan.

Shyu et al. (2016) identified a west-dipping thrust fault, the Kaoping River Structure, based on river terrace morphology, estimating an uplift rate of 0.43–0.46 mm/yr. However, this study found no clear evidence of creeping along the Kaoping River Structure using InSAR data. From the InSAR result, Pingtung Boundary likely represents a shallow creeping fault to its east, with similar geometry, which may influence the activity of the Kaoping River Structure.

These findings highlight the complexity of active faulting across the Pingtung Plain, where subsidence can mask or modify near-surface fault expressions. The high spatial resolution of InSAR data allows for precise delineation of velocity boundaries caused by shallow fault creep, which may otherwise remain undetected using traditional survey methods. By correlating InSAR results with field observations, researchers can better constrain fault geometry and slip behavior, leading to more reliable assessments of seismic hazard.

doi: 10.6342/NTU202500538

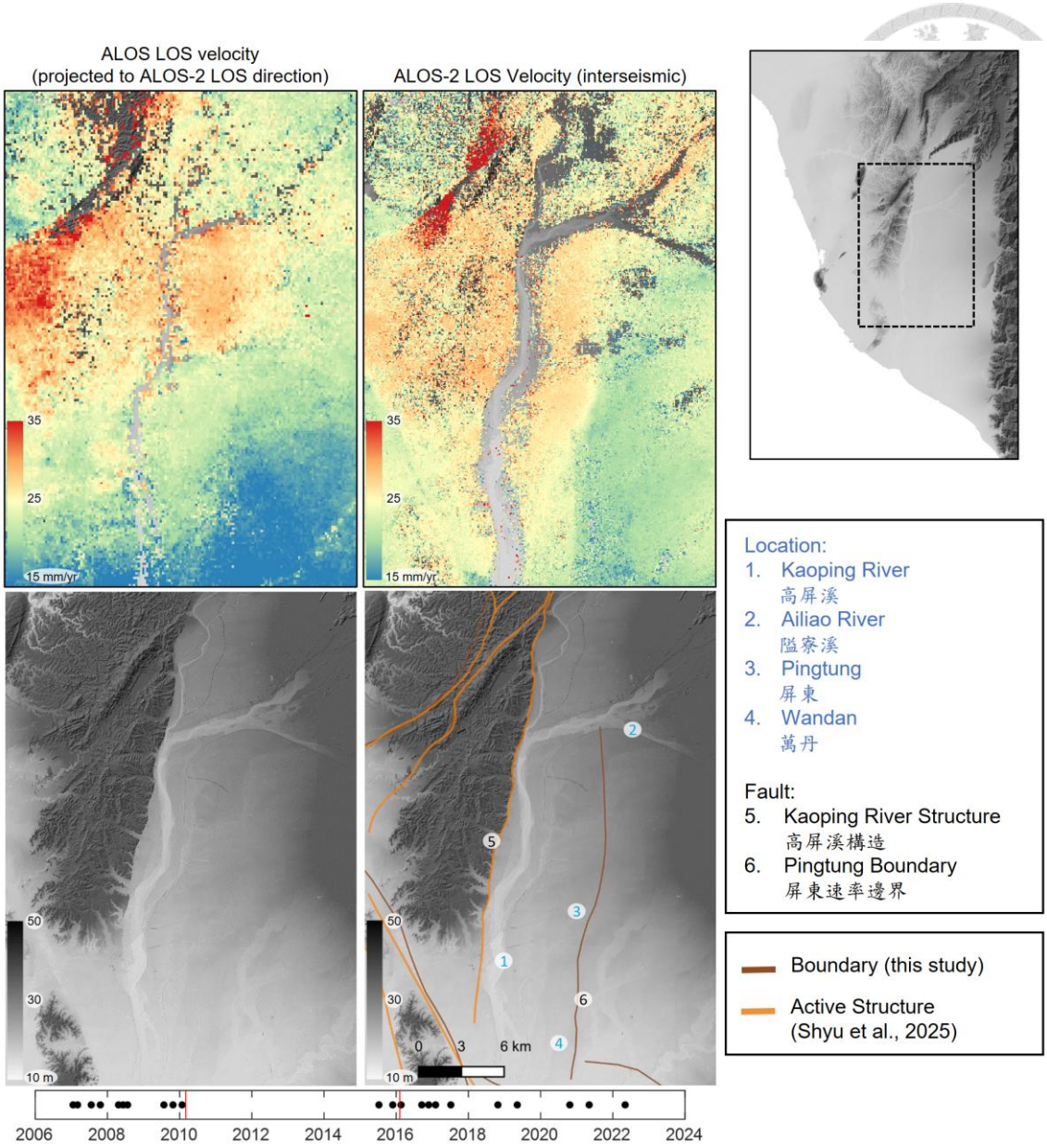

Figure 57. Zoomed in maps of two interseismic velocity fields. The bottom-right map highlights the Kaoping River Structure from Shyu et al. (2025) and the Pingtung Boundary identified in this study.

doi: 10.6342/NTU202500538

The Daliao Boundary, a branch of the Fengshan Boundary, crosses the Kaoping River in an east-west direction and truncates the north-south trending Kaopingshi Boundary. Both boundaries display clear, well-defined patterns in the InSAR velocity fields from both ALOS and ALOS-2, indicating that these two shallow active structures have been steadily deforming at rates of approximately 3–5 mm/yr in the LOS direction over the past two decades.

On the eastern margin of the Pingtung Plain, the north-south trending Chaochou Fault has been identified through previous geological studies as an active thrust fault system with over two million years of activity, based on stratigraphic relationships and geomorphic evidence (e.g. Chen et al., 2011). However, no interseismic creeping is observed along the Chaochou Fault in either of the InSAR velocity fields. Instead, a distinct velocity boundary west of the Chaochou Fault, referred to here as the Fangliao Boundary, shows different behaviors. The Fangliao Boundary exhibits no significant activity in the ALOS velocity field, but in the ALOS-2 velocity field, rapid interseismic creeping is observed at rates of approximately 11–14 mm/yr on either side of the fault. This behavior is further corroborated by leveling velocity profiles shown in Figure 50, which reflect a similar deformation trend. The cause of this transient deformation event and its implications for the seismic potential of the Chaochou Fault require further investigation.

This study identifies three shallow active faults on the Pingtung Plain, which exhibiting deformation rates ranging from a few millimeters to over ten millimeters per year. Interestingly, these faults lack clear surface geomorphic features, suggesting they may be relatively young active faults. The seismic potential of these shallow creeping faults and their influence on stress distribution in the surrounding region remain critical questions for future research and assessment.

doi: 10.6342/NTU202500538

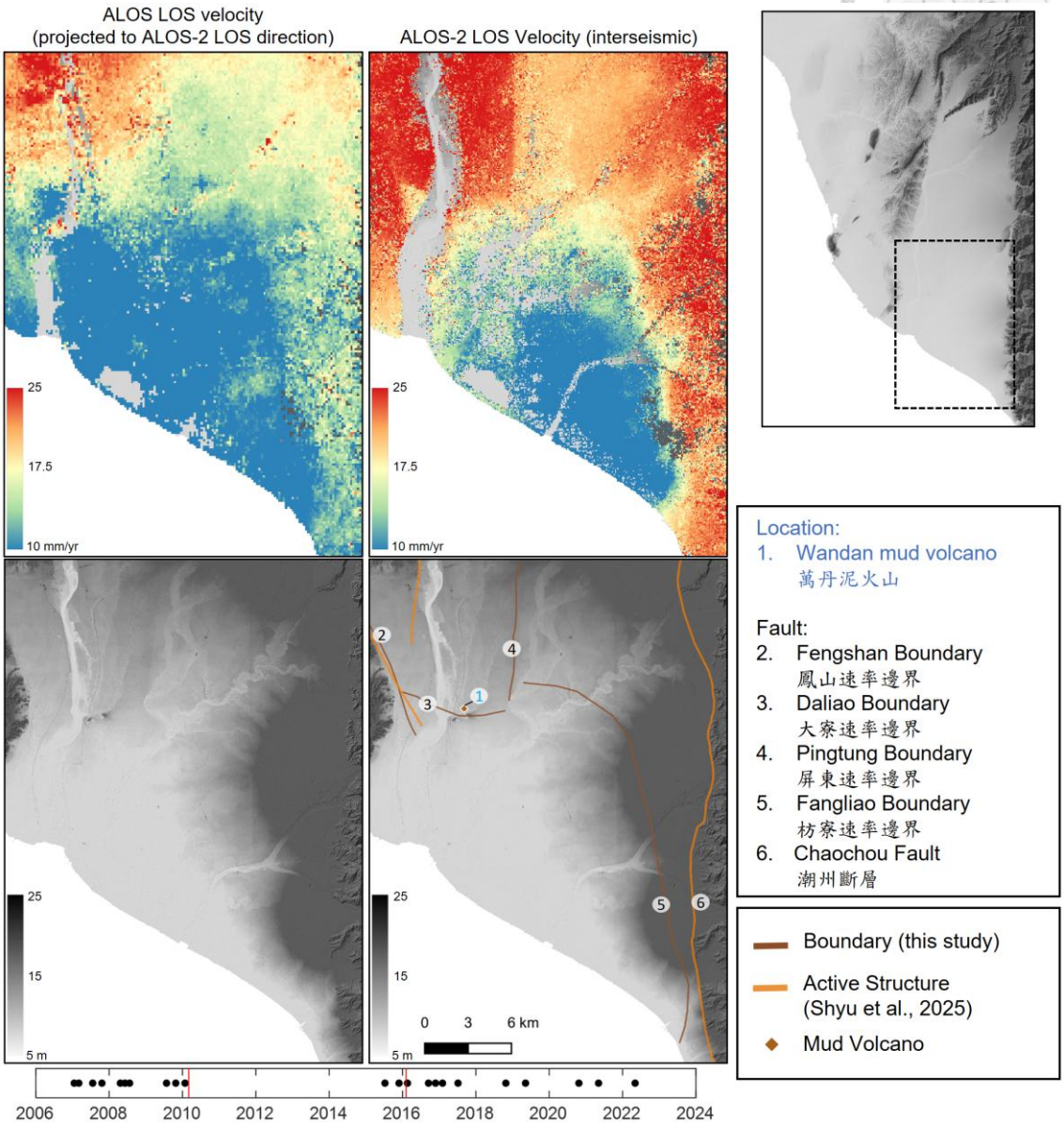

Figure 58. Zoomed in maps of two interseismic velocity fields. The bottom-right map highlights the Fengshan, Daliao, Pingtung, and Fangliao Boundaries, and the location of the Wandan mud volcano.

doi: 10.6342/NTU202500538

6.4. Temporal Evolution of Fault Activity

In Section 5.2 and Section 5.3, I compared the velocity changes between the two InSAR time series, and mapped boundaries that show clear velocity contrasts in those maps. As the previous paragraphs in the discussion section addressed, the observed slip rates and velocity patterns reveal significant temporal variations across different tectonic structures. Specifically, velocity boundaries such as the Houchiali Boundary and Chungchou Boundary, which were influenced by the 2016 Meinong Earthquake, exhibit significant changes in slip rates between the two InSAR time periods. These variations are likely reflective of transient deformation processes triggered by seismic events. In addition, notable velocity changes are observed in the southern Pingtung Plain, particularly along the Fangliao Boundary, which is far away from the direct impact of the Meinong Earthquake. The slip rate variation is clear in both InSAR and leveling data, but the driving mechanisms of this event remain unknown.

To quantitatively compare the deformation rates across different boundaries during the two observation periods, I selected two rectangular areas on either side of each of the 15 boundaries. Each rectangle measures 2 kilometers in length and 1 kilometer in width, with a separation of 1 kilometer between them. By calculating the velocity difference between these two rectangles, I quantified the rate of deformation across each boundary. The results, representing the velocity differences along the ALOS-2 LOS direction during the ALOS and ALOS-2 time periods, are illustrated in Figure 59.

These results are further compared with long-term vertical uplift rates derived from previous studies using geological methods such as river terraces and borehole data. This comparison emphasizes the importance of variations in creep rates observed over geodetic timescales, and highlights the potential differences between short-term geodetic observations and long-term geological processes.

doi: 10.6342/NTU202500538

From Figure 59, it is evident that most of the 15 boundaries in the study region exhibit creeping behavior. For instance, the LOS deformation rate of the Houchiali Boundary reversed from -2.7 mm/yr to 2.5 mm/yr, while the southern segment of the Chungchou Boundary accelerated significantly from 2.4 mm/yr to 18.5 mm/yr over the past two decades. These observations have reshaped our understanding of active faults in Southwestern Taiwan, highlighting the necessity of incorporating a more comprehensive geodetic dataset to develop an accurate geohazard potential model for the region.

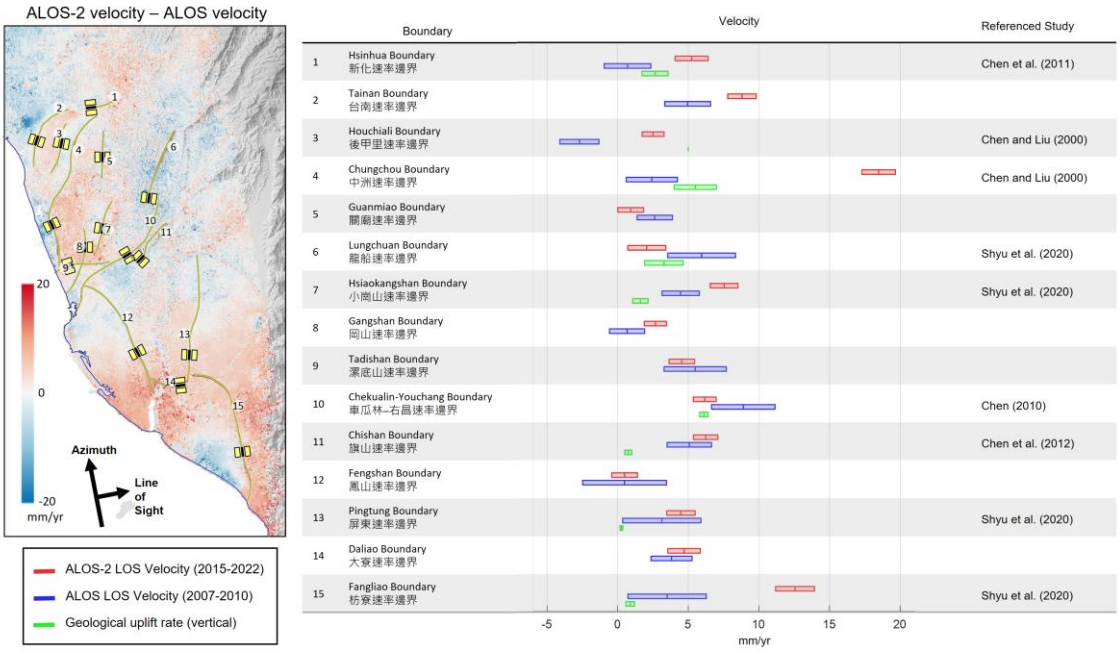

Figure 59. This figure compares ALOS (2007–2010) and ALOS-2 (2015–2022) InSAR interseismic velocities in the LOS direction with geological uplift rates from referenced studies. InSAR data were collected from the yellow rectangles on either side of the 15 boundaries shown on the map. Geological uplift rates for the Kaopingshi Boundary are from the Kaoping River Structure, and for the Fangliao Boundary from the Chaochou Fault (Shyu et al., 2020).

doi: 10.6342/NTU202500538

By analyzing slip rate changes along several long boundaries in the study area, inconsistent variations along the fault lines were observed. Figure 60 divides each boundary into 1-km segments, with 1-km by 1-km rectangles drawn on both sides of each segment. Differences in InSAR LOS velocities between the rectangles are calculated, with the sum of their squared standard deviations used as the error.

The results reveal notable spatial patterns. Along the southern Chungchou Boundary, velocity changes reach up to 19 mm/yr, while the northern section shows minimal variation. For the Chekualin-Youchang Boundary, slip rates accelerate from Shoushan to NUK campus but clearly decrease from NUK to Yanchao. Near the NUK campus, the Fengshan Boundary intersects the Chekualin-Youchang Boundary. Whether these slip rate changes are linked to Fengshan Fault activity requires further study.

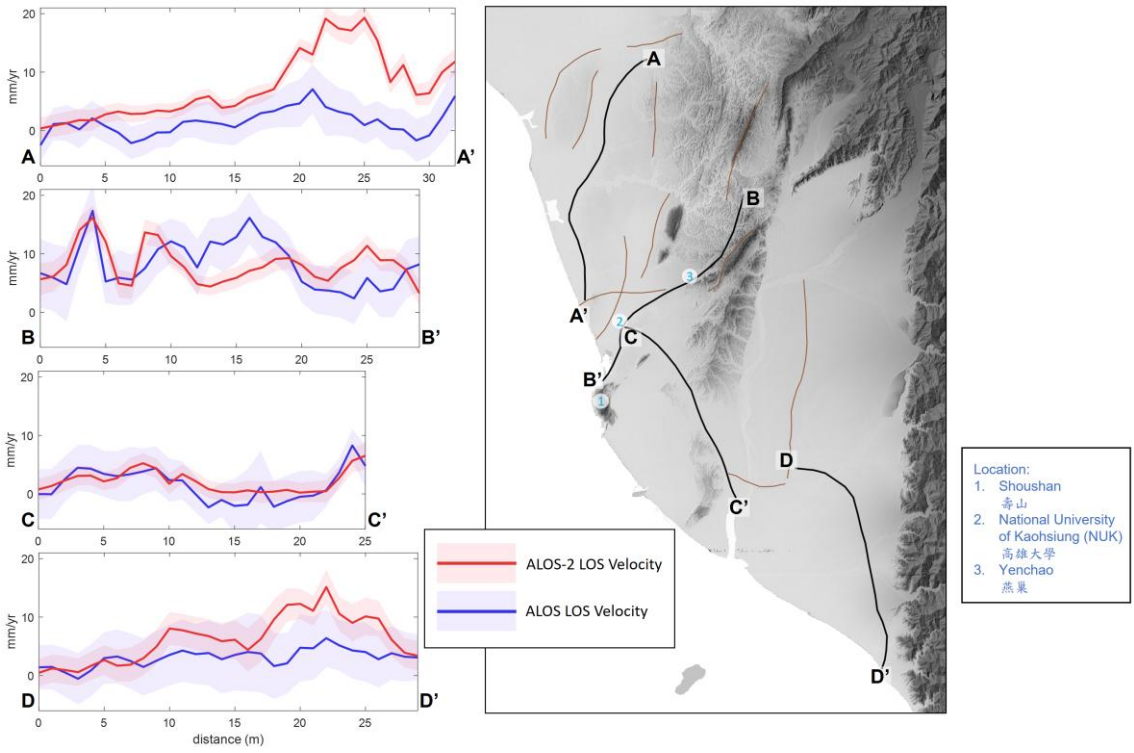

Figure 60. The velocity difference between the Chungchou (A-A'), Youchang-Chekualin Boundary (B-B'), Fengshan Boundary (C-C'), and Fangliao Boundary (D-D') in two different periods. The shaded buffer along the profiles represents the velocity uncertainty.

doi: 10.6342/NTU202500538

6.5. Contributions to Hazard Assessment

This study identifies 15 velocity boundaries in the Southwestern Taiwan using high-resolution InSAR data, which are likely indicative of shallow creeping faults. These creeping behaviors pose direct threats to critical infrastructure and emphasize the need for a dynamic approach to seismic hazard assessment. Subtle or episodic fault movements, such as those observed along the Chekualin-Youchang Boundary, Pingtung Boundary, and Fangliao Boundary, can redistribute strain, reduce slip deficits on major faults, and influence future earthquakes.

Taiwan High-Speed Rail systems, with their strict track stability requirements, are particularly vulnerable to the impacts of creeping faults. As shown in Figure 61, LOS measurements from ALOS-2 data indicate interseismic deformation rates of 4.3 mm/yr, 2.5 mm/yr, and 6.2 mm/yr across the Hsinhua Boundary, Hsiaokangshan Boundary, and Chekualin Boundary, respectively, over a 1-kilometer span. Notably, Lu et al. (2025) constructed a three-dimensional velocity field for Southwestern Taiwan from 2016 to 2018 using Sentinel-1 data and identified areas of significant deformation along railway routes near these same faults. They attributed this high hazard potential to post-seismic deformation following the 2016 Meinong earthquake, which aligns with the ALOS-2 observations presented in this study. Similarly, the Chekualin-Youchang Boundary threatens the Ciaotou Science Park, where profiles in Figure 61 show interseismic creeping rates of 5–8 mm/yr, posing risks to critical facilities and their economic contributions.

This study highlights two critical impacts of shallow creeping faults. First, the identification of these creeping faults challenges traditional slip deficit models, which are essential for assessing seismic potential. Second, the active creeping behaviors of these faults present immediate risks to critical infrastructure in Southwestern Taiwan, including

doi: 10.6342/NTU202500538

densely populated areas with cultural landmarks, industrial hubs, and science parks. InSAR has proven indispensable for uncovering and monitoring these subtle fault movements. Future research integrating InSAR with other geophysical and geological methods will be essential for refining seismic hazard models and enhancing infrastructure resilience in this tectonically active region.

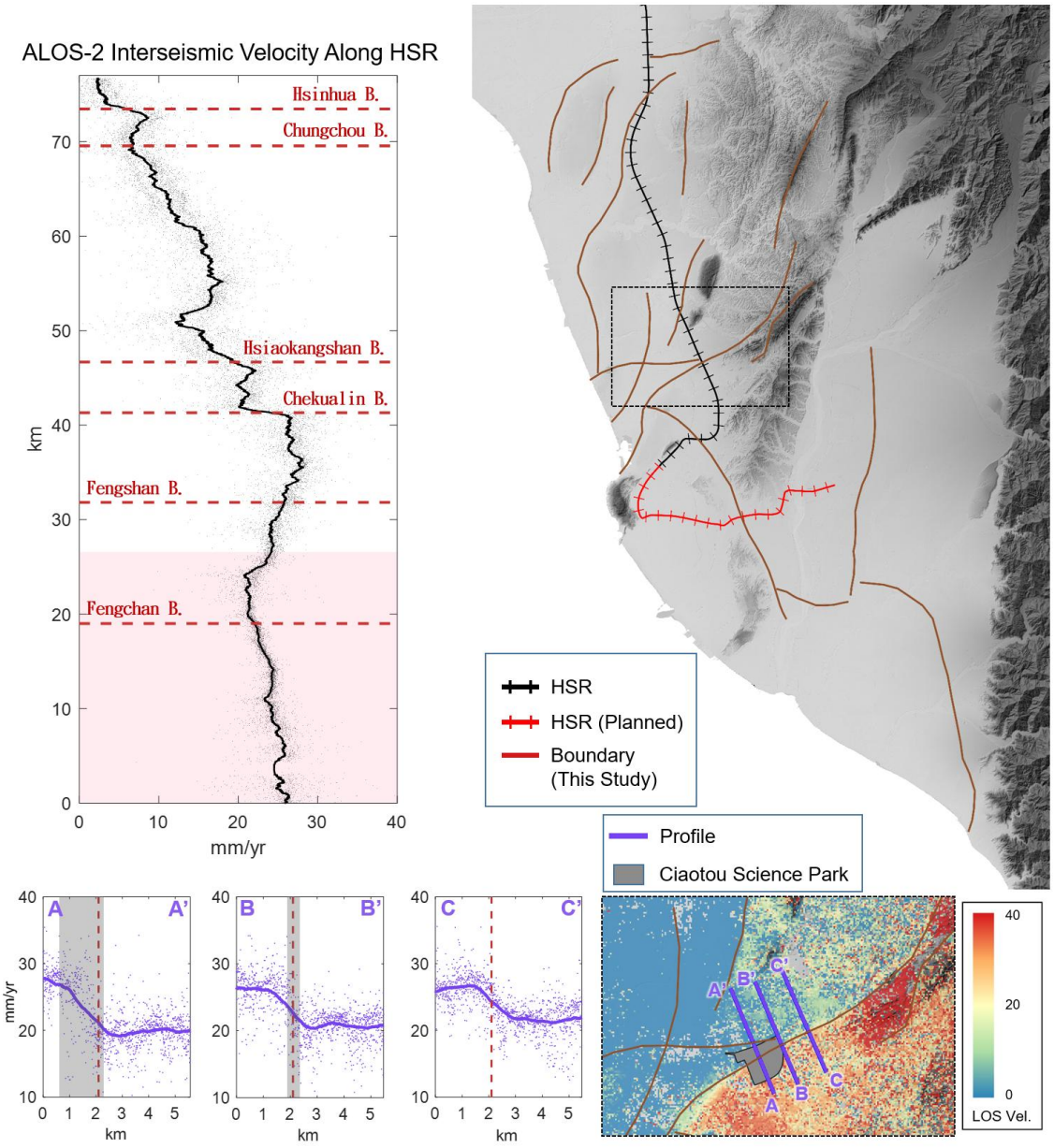

Figure 61. ALOS-2 LOS velocity profiles along the Taiwan High Speed Rail (HSR), and across the Ciaotou Science Park.

doi: 10.6342/NTU202500538

Chapter 7 Conclusion

- Using the SBAS-InSAR algorithm, I successfully integrated images from 2 different SAR satellites to generate a high-resolution deformation map for Southwestern Taiwan from 2007 to 2022, showing strong correlation with ground-based GNSS stations.
- By comparing interseismic deformation rates from ALOS (2007-2010) and ALOS-2 (2015-2022) and the coseismic deformation field from the 2016 Meinong earthquake, 15 velocity boundaries exhibiting clear velocity contrasts were identified in the study region between the Hsinhua Fault and the Pingtung Plain. These contrasts likely indicate shallow creeping behavior of active structures.
- Profiles of InSAR and leveling measurements reveal variations in creep rates along several active structures. Notably, the Chungchou, Gangshan, Tadishan, Pingtung, Daliao, and Fangliao boundaries exhibit clear signs of activity, although they have not been well-documented as shallow active structures in previous studies.
- The identified boundaries and their activity patterns provide valuable insights into the creeping behavior of shallow faults, emphasizing the need for continuous monitoring to assess their potential impact on seismic hazards in Southwestern Taiwan.

doi: 10.6342/NTU202500538

Reference

Angelier, J., Chang, T. Y., Hu, J. C., Chang, C. P., Siame, L., Lee, J. C., ... & Lu, C. Y. (2009). Does extrusion occur at both tips of the Taiwan collision belt? Insights from active deformation studies in the Ilan Plain and Pingtung Plain regions. Tectonophysics, 466(3-4), 356-376.

Angelier, J., Barrier, E., & Chu, H. T. (1986). Plate collision and paleostress trajectories in a fold-thrust belt: the foothills of Taiwan. Tectonophysics, 125(1-3), 161-178.

Barbot, S., Fialko, Y., & Bock, Y. (2009). Postseismic deformation due to the Mw 6.0 2004 Parkfield earthquake: Stress-driven creep on a fault with spatially variable rate-and-state friction parameters. Journal of Geophysical Research: Solid Earth, 114(B7).

Bekaert, D. P. S., Hooper, A., & Wright, T. J. (2015). A spatially variable power law tropospheric correction technique for InSAR data. Journal of Geophysical Research: Solid Earth, 120(2), 1345-1356.

Berardino, P., Fornaro, G., Lanari, R., & Sansosti, E. (2002). A new algorithm for surface deformation monitoring based on small baseline differential SAR interferograms. IEEE Transactions on geoscience and remote sensing, 40(11), 2375-2383.

Blanpied, M. L., Lockner, D. A., & Byerlee, J. D. (1995). Frictional slip of granite at hydrothermal conditions. Journal of Geophysical Research: Solid Earth, 100(B7), 13045-13064.

Bonilla, M. G. (1977). Summary of Quaternary faulting and elevation changes in Taiwan. Memoir of the Geological Society of China, 2, 43-55.

Brcic, R., Parizzi, A., Eineder, M., Bamler, R., & Meyer, F. (2010, July). Estimation and compensation of ionospheric delay for SAR interferometry. In 2010 IEEE International Geoscience and Remote Sensing Symposium (pp. 2908-2911). IEEE.

doi: 10.6342/NTU202500538

Bürgmann, R., Hilley, G., Ferretti, A., & Novali, F. (2006). Resolving vertical tectonics in the San Francisco Bay Area from permanent scatterer InSAR and GPS analysis. Geology, 34(3), 221-224.

Carena, S., Suppe, J., & Kao, H. (2002). Active detachment of Taiwan illuminated by small earthquakes and its control of first-order topography. Geology, 30(10), 935-938.

Cavalié, O., Doin, M. P., Lasserre, C., & Briole, P. (2007). Ground motion measurement in the Lake Mead area, Nevada, by differential synthetic aperture radar interferometry time series analysis: Probing the lithosphere rheological structure. Journal of Geophysical Research: Solid Earth, 112(B3).

Chang, L.-S., Chow, M., & Chen, P.-Y. (1947). The Tainan Earthquake Of December 5, 1946. Bulletin of the Geological Survey of Taiwan, 1(1), 11-18. (In Chinese)

Chang-Lee C. (2014). Behavior analysis of the LCNF-CHNF fault system using geodetic measurements. Master's thesis, Department of Earth Sciences, National Cheng Kung University, 110 pages. (In Chinese)

Chao, C. M. (2016). Surface Creeping Analysis of the Fengshan Fault in SW Taiwan from GPS observations and PSInSAR. Master's thesis, Department of Earth Sciences, National Cheng Kung University, 89 pages.

Chen, Y. G., & Liu, T. K. (2000). Holocene uplift and subsidence along an active tectonic margin southwestern Taiwan. Quaternary Science Reviews, 19(9), 923-930.

Chen, W. S., & Yu, N. T. (2007). 地震地質與地變動潛勢分析計畫—斷層長期滑移速率與再現週期研究(1/4). Central Geological Survey, Ministry of Economic Affairs, Report No. 96-10, 86 pages. (In Chinese)

doi: 10.6342/NTU202500538

Chen, C. W., & Zebker, H. A. (2002). Phase unwrapping for large SAR interferograms: Statistical segmentation and generalized network models. IEEE Transactions on Geoscience and Remote Sensing, 40(8), 1709-1719.

Chen, W. S., Matsuda, N., Shih, R. C., Yang, C. C., Yu, N.-T., Chu, Y. G., Chen, C. H., Lin, C. W., Liu, H. C., Lu, S. T., Liu, Y. C., Lin, Y. H., & Chen, P. T. (2010). Concealed Active Structures beneath the Holocene Marine Sediments in the Western Coastal Plain Using Taiwan as an Example for the Hsiaokangshan Fault. Special Publication of the Central Geological Survey, Ministry of Economic Affairs, No. 24, pp. 75-91. (In Chinese)

Chen, W. S., Yu, N. T., & Yang, H. C. (2011). Study of the Near Surface Structure of Active Fault (1/4). Central Geological Survey, Ministry of Economic Affairs, Report No. 100-9, 118 pp. (In Chinese)

Chen, W. S., Wu, Y. M., Yang, K. M., Yeh, P. Y., Hung, C. C., Yang, C. Y., Ke, M. C., & Ke, S. S. (2024). 臺灣地震帶. National Science and Technology Center for Disaster Reduction. (In Chinese)

Chen, P. T. (2005). A Study on the southern part of Chishan fault. Master's thesis, Department of Earth Sciences, National Cheng Kung University, 109 pages. (In Chinese)

Chen, Y. S. (2015). Interseismic deformation of the Longchuan and Chishan faults using geodetic measurements. Master's thesis, Department of Geomatics, National Cheng Kung University, 79 pages. (In Chinese)

Chen, J. Y. (2022). Using InSAR and Numerical Method to Characterize the Active Deformation and Structural Evolution in Southwestern Taiwan. Master's thesis, National Taiwan University, 101 pages. (In Chinese)

doi: 10.6342/NTU202500538

Ching, K. E., Rau, R. J., Lee, J. C., & Hu, J. C. (2007). Contemporary deformation of tectonic escape in SW Taiwan from GPS observations, 1995–2005. Earth and Planetary Science Letters, 262(3-4), 601-619.

Ching, K. E., Johnson, K. M., Rau, R. J., Chuang, R. Y., Kuo, L. C., & Leu, P. L. (2011). Inferred fault geometry and slip distribution of the 2010 Jiashian, Taiwan, earthquake is consistent with a thick-skinned deformation model. Earth and Planetary Science Letters, 301(1-2), 78-86.

Ching, K.E. (2017). 台灣及鄰近地區地體動力學研究 II (GOTTA II)-探討台灣西南部、菲律賓中部與印度東北部主要都會區之震間期地表變形特性及其地震潛能. MOST Research Project Grant, 24 pages. (In Chinese)

Chiu, Y. W., Lin, Y. C., Huang, W. J., Yen, Y. C., Bo, M. L., Lee, Y. H. (2019). Characteristics of the Chishan Fault Zone Exposed around the North End of Zhongliao Tunnel, Southwestern Taiwan. Special Publication of the Central Geological Survey, No. 34, 83-100. (In Chinese)

Chou, J. T. (1971). A Preliminary Study Of The Stratigraphy And Sedimentation Of The Mudstone Formations In The Tainan Area, Southern Taiwan. Petrol Geol Taiwan, 8, 187-219.

Copley, A. (2014). Postseismic afterslip 30 years after the 1978 Tabas-e-Golshan (Iran) earthquake: observations and implications for the geological evolution of thrust belts. Geophysical Journal International, 197(2), 665-679.

Davis, D., Suppe, J., & Dahlen, F. A. (1983). Mechanics of fold-and-thrust belts and accretionary wedges. Journal of Geophysical Research: Solid Earth, 88(B2), 1153-1172.

Di Toro, G., Mittempergher, S., Ferri, F., Mitchell, T. M., & Pennacchioni, G. (2012). The contribution of structural geology, experimental rock deformation and numerical

doi: 10.6342/NTU202500538

modelling to an improved understanding of the seismic cycle: Preface to the Special Volume 'Physico-chemical processes in seismic faults'. Journal of Structural Geology, 38, 3-10.

Dieterich, J. H. (1978). Time-dependent friction and the mechanics of stick-slip. Rock friction and earthquake prediction, 790-806.

Dieterich, J. H. (1979). Modeling of rock friction: 1. Experimental results and constitutive equations. Journal of Geophysical Research: Solid Earth, 84(B5), 2161-2168.

Doin, M. P., Lasserre, C., Peltzer, G., Cavalié, O., & Doubre, C. (2009). Corrections of stratified tropospheric delays in SAR interferometry: Validation with global atmospheric models. Journal of Applied Geophysics, 69(1), 35-50.

Dragert, H., Wang, K., & James, T. S. (2001). A silent slip event on the deeper Cascadia subduction interface. Science, 292(5521), 1525-1528.

Esri. (n.d.). World Imagery [Basemap]. Retrieved from https://services.arcgisonline.com/ArcGIS/rest/services/World_Imagery/MapServer

Fattahi, H., Simons, M., & Agram, P. (2017). InSAR time-series estimation of the ionospheric phase delay: An extension of the split range-spectrum technique. IEEE Transactions on Geoscience and Remote Sensing, 55(10), 5984-5996.

Ferretti, A., Prati, C., & Rocca, F. (2001). Permanent scatterers in SAR interferometry. IEEE Transactions on geoscience and remote sensing, 39(1), 8-20.

Floyd, M. A., Walters, R. J., Elliott, J. R., Funning, G. J., Svarc, J. L., Murray, J. R., ... & Wright, T. J. (2016). Spatial variations in fault friction related to lithology from rupture and afterslip of the 2014 South Napa, California, earthquake. Geophysical Research Letters, 43(13), 6808-6816.

doi: 10.6342/NTU202500538

Franklin, K. R., & Huang, M. H. (2022). Revealing crustal deformation and strain rate in Taiwan using InSAR and GNSS. Geophysical Research Letters, 49(21), e2022GL101306.

Freeman, A., & Saatchi, S. S. (2004). On the detection of Faraday rotation in linearly polarized L-band SAR backscatter signatures. IEEE Transactions on Geoscience and Remote Sensing, 42(8), 1607-1616.

Fruneau, B., Pathier, E., Raymond, D., Deffontaines, B., Lee, C. T., Wang, H. T., ... & Chang, C. P. (2001). Uplift of Tainan Tableland (SW Taiwan) revealed by SAR interferometry. Geophysical Research Letters, 28(16), 3071-3074.

Gomba, G., Parizzi, A., De Zan, F., Eineder, M., & Bamler, R. (2015). Toward operational compensation of ionospheric effects in SAR interferograms: The split-spectrum method. IEEE Transactions on Geoscience and Remote Sensing, 54(3), 1446-1461.

Graham, L. C. (1974). Synthetic interferometer radar for topographic mapping. Proceedings of the IEEE, 62(6), 763-768.

Harris, R. A. (2017). Large earthquakes and creeping faults. Reviews of Geophysics, 55(1), 169-198.

Harris, R. A., & Segall, P. (1987). Detection of a locked zone at depth on the Parkfield, California, segment of the San Andreas fault. Journal of Geophysical Research: Solid Earth, 92(B8), 7945-7962.

Hersbach, H., Bell, B., Berrisford, P., Hirahara, S., Horányi, A., Muñoz-Sabater, J., ... & Thépaut, J. N. (2020). The ERA5 global reanalysis. Quarterly Journal of the Royal Meteorological Society, 146(730), 1999-2049.

Hooper, A., Zebker, H., Segall, P., & Kampes, B. (2004). A new method for measuring deformation on volcanoes and other natural terrains using InSAR persistent scatterers. Geophysical research letters, 31(23).

doi: 10.6342/NTU202500538

Hooper, A., Segall, P., & Zebker, H. (2007). Persistent scatterer interferometric synthetic aperture radar for crustal deformation analysis, with application to Volcán Alcedo, Galápagos. Journal of Geophysical Research: Solid Earth, 112(B7).

Hsieh, S. H. (1972). Subsurface geology and gravity anomalies of the Tainan and Chungchou structures of the coastal plain of southwestern Taiwan. Petrol Geol Taiwan, 10, 323-338.

Hsu, T. L., & Chang, H. C. (1979). Quaternary faulting in Taiwan. Memoir of the Geological Society of China, 3, 155–165.

Hsu, Y. J., Yu, S. B., Kuo, L. C., Tsai, Y. C., & Chen, H. Y. (2011). Coseismic deformation of the 2010 Jiashian, Taiwan earthquake and implications for fault activities in southwestern Taiwan. Tectonophysics, 502(3-4), 328-335.

Hu, J. C., Hou, C. S., Shen, L. C., Chan, Y. C., Chen, R. F., Huang, C., ... & Nien, P. F. (2007). Fault activity and lateral extrusion inferred from velocity field revealed by GPS measurements in the Pingtung area of southwestern Taiwan. Journal of Asian Earth Sciences, 31(3), 287-302.

Hu, L. F. (2025). Reassessment of the Chungchou structure and related seismogenic structures in its vicinity in the Western Foothills, Tainan-Kaohsiung area, Taiwan. Department of Geosciences, National Taiwan University. Unpublished study.

Huang, C. Y., Wu, W. Y., Chang, C. P., Tsao, S., Yuan, P. B., Lin, C. W., & Xia, K. Y. (1997). Tectonic evolution of accretionary prism in the arc-continent collision terrane of Taiwan. Tectonophysics, 281(1-2), 31-51.

Huang, S. T., Yang, K. M., Hung, J. H., Wu, J. C., Ting, H. H., Mei, W. W., ... & Lee, M. (2004). Deformation front development at the northeast margin of the Tainan basin, Tainan–Kaohsiung area, Taiwan. Marine Geophysical Researches, 25, 139-156.

doi: 10.6342/NTU202500538

Huang, H. H., Yih-Min, W., Ting-Li, L., Wei-An, C., Shyu, J. B. H., Chung-Han, C., & Chang, C. H. (2011). The preliminary study of the 4 March 2010 Mw 6.3 Jiasian, Taiwan earthquake sequence. TAO: Terrestrial, Atmospheric and Oceanic Sciences, 22(3), 2.

Huang, M. H., Hu, J. C., Hsieh, C. S., Ching, K. E., Rau, R. J., Pathier, E., ... & Deffontaines, B. (2006). A growing structure near the deformation front in SW Taiwan as deduced from SAR interferometry and geodetic observation. Geophysical Research Letters, 33(12).

Huang, M. H., Hu, J. C., Ching, K. E., Rau, R. J., Hsieh, C. S., Pathier, E., Fruneau, B. & Deffontaines, B. (2009). Active deformation of Tainan tableland of southwestern Taiwan based on geodetic measurements and SAR interferometry. Tectonophysics, 466(3-4), 322-334.

Huang, M. H., Dreger, D., Bürgmann, R., Yoo, S. H., & Hashimoto, M. (2013). Joint inversion of seismic and geodetic data for the source of the 2010 March 4, M w 6.3 Jia-Shian, SW Taiwan, earthquake. Geophysical Journal International, 193(3), 1608-1626.

Huang, M. H., Tung, H., Fielding, E. J., Huang, H. H., Liang, C., Huang, C., & Hu, J. C. (2016). Multiple fault slip triggered above the 2016 Mw 6.4 MeiNong earthquake in Taiwan. Geophysical Research Letters, 43(14), 7459-7467.

Hung, J.H., Wiltschko, D.V., Lin, H.C., Hichman, J.B., Fang, P. & Bock, Y. (1999). Structure and motion of the Southwestern Taiwan Fold and Thrust Belt. Tao 10, 543–68.

Jiang, Y. W. (2024). Using PSInSAR to monitor the surface deformation of critical infrastructure in SW Taiwan. Master's thesis, Department of Geography, National Taiwan University, 119 pages.

doi: 10.6342/NTU202500538

Jolivet, R., Agram, P. S., Lin, N. Y., Simons, M., Doin, M. P., Peltzer, G., & Li, Z. (2014). Improving InSAR geodesy using global atmospheric models. Journal of Geophysical Research: Solid Earth, 119(3), 2324-2341.

Jung, H. S., Lee, D. T., Lu, Z., & Won, J. S. (2012). Ionospheric correction of SAR interferograms by multiple-aperture interferometry. IEEE Transactions on Geoscience and Remote Sensing, 51(5), 3191-3199.

Kaneko, Y., Fialko, Y., Sandwell, D. T., Tong, X., & Furuya, M. (2013). Interseismic deformation and creep along the central section of the North Anatolian Fault (Turkey): InSAR observations and implications for rate-and-state friction properties. Journal of Geophysical Research: Solid Earth, 118(1), 316-331.

Kim, J. S. (2013). Development of ionosphere estimation techniques for the correction of SAR data (Doctoral dissertation, ETH Zurich).

Kirui, P. K. E., Reinosch, E., Isya, N., Riedel, B., & Gerke, M. (2021). Mitigation of atmospheric artefacts in multi temporal InSAR: a review. PFG–Journal of Photogrammetry, Remote Sensing and Geoinformation Science, 89, 251-272.

Lacombe, O., Mouthereau, F., Deffontaines, B., Angelier, J., Chu, H. T., & Lee, C. T. (1999). Geometry and Quaternary kinematics of fold-and-thrust units of southwestern Taiwan. Tectonics, 18(6), 1198-1223.

Lacombe, O., Mouthereau, F., Angelier, J., & Deffontaines, B. (2001). Structural, geodetic and seismological evidence for tectonic escape in SW Taiwan. Tectonophysics, 333(1-2), 323-345.

Lawson, A. C., & Reid, H. F. (1910). The California Earthquake of April 18, 1906: Report of the State Earthquake Investigation Commission.. (No. 87). Carnegie institution of Washington.

doi: 10.6342/NTU202500538

Le Béon, M., Huang, M. H., Suppe, J., Huang, S. T., Pathier, E., Huang, W. J., ... & Hu, J. C. (2017). Shallow geological structures triggered during the Mw 6.4 Meinong earthquake, southwestern Taiwan. Terrestrial, Atmospheric and Oceanic Sciences, 28(5), 663-681.

Le Béon, M., Marc, O., Suppe, J., Huang, M. H., Huang, S. T., & Chen, W. S. (2019). Structure and deformation history of the rapidly growing Tainan anticline at the deformation front of the Taiwan mountain belt. Tectonics, 38(9), 3311-3334.

Lee, Y. H. (2024). InSAR-based Multidecadal Coastal Land Subsidence Analysis and Future Inundation Scenarios inWestern Taiwan. Master thesis, Department of Geography, National Taiwan University. 174 pages.

Liang, C., & Fielding, E. J. (2017). Measuring azimuth deformation with L-band ALOS-2 ScanSAR interferometry. IEEE Transactions on Geoscience and Remote Sensing, 55(5), 2725-2738.

Lin, C. W., Lu, S. T., Shih, T. S., Liu, Y. C. Lin, W. H., Lin, Y. H. (2007). Active Faults Of Southwestern Taiwan: Explanatory Text For The Strip Maps Of Active Faults SCALE 1:25,000. Special Publication of the Central Geological Survey, 17, 95-108. (In Chinese)

Lin, C. W., Chen, W. S., Liu, Y. C., Chen, P. T. (2009). Active Faults of Eastern and Southern Taiwan: Explanatory Text for the Strip Maps of Active Faults SCALE 1:25000. Special Publication of the Central Geological Survey, 23, 111-132. (In Chinese)

Lin, C. W., Lu, S. T., & Chen, W. S. (2012). Active Fault Map of Taiwan: An Explanatory Text (2012 Edition). Special Publication of the Central Geological Survey, 26, 1-30. (In Chinese)

doi: 10.6342/NTU202500538

Lin, K. C., Delouis, B., Hu, J. C., Nocquet, J. M., & Mozziconacci, L. (2016). Reassessing the complexity of the rupture of the 2010 Jia-Shian earthquake (Mw 6.2) in Southwestern Taiwan by inverting jointly teleseismic, strong-motion and CGPS data. Tectonophysics, 692, 278-294.

Lin, Q. W., Liu, Y. C., Chou, P. S., & Lin, Y. H. (2021). Recent development of active fault investigations of Taiwan. Bulletin of the Central Geological Survey, (34), 1–40. (In Chinese).

Lin, C.-C. (1957). 地形（土地志・地理篇・第一冊）. Historical Records Committee of Taiwan Provincial Government, 424 pages. (In Chinese)

Lin, G. P. (2012). Crustal Deformation of Tainan Region from Persistent Scatterer Interferometry. Master's thesis, Institute of Geophysics, National Central University, 81 pages.

Lu, C. H., Chuang, R. C., Chiang, P. C., Yen, J. Y., Ching, K. E., & Chen, Y. G. (2025). Detecting infrastructure hazard potential change by SAR techniques on postseismic surface deformation: A case study of 2016 Meinong earthquake in southwestern Taiwan. Engineering Geology, 344, 107827.

Lu, C. Y., & Malavieille, J. (1994). Oblique convergence, indentation and rotation tectonics in the Taiwan Mountain Belt: Insights from experimental modelling. Earth and Planetary Science Letters, 121(3-4), 477-494.

Lu C.Y. (1994). Neotectonics in the forland thrust belt of Taiwan. Petrol. Geol. Taiwan, vol.29, p. 1-26.

Malavieille, J., Dominguez, S., Lu, C. Y., Chen, C. T., & Konstantinovskaya, E. (2021). Deformation partitioning in mountain belts: insights from analogue modelling experiments and the Taiwan collisional orogen. Geological Magazine, 158(1), 84-103.

doi: 10.6342/NTU202500538

Marone, C. J., Scholtz, C. H., & Bilham, R. (1991). On the mechanics of earthquake afterslip. Journal of Geophysical Research: Solid Earth, 96(B5), 8441-8452.

Massonnet, D., Rossi, M., Carmona, C., Adragna, F., Peltzer, G., Feigl, K., & Rabaute, T. (1993). The displacement field of the Landers earthquake mapped by radar interferometry. nature, 364(6433), 138-142.

Mattar, K., & Gray, A. (2002). Reducing ionospheric electron density errors in satellite radar interferometry applications. Canadian Journal of Remote Sensing, 28(4), 593–600. https://doi.org/10.5589/m02-051

Murray, J., & Langbein, J. (2006). Slip on the San Andreas Fault at Parkfield, California, over two earthquake cycles, and the implications for seismic hazard. Bulletin of the Seismological Society of America, 96(4B), S283-S303.

Murray, J., & Segall, P. (2002). Testing time-predictable earthquake recurrence by direct measurement of strain accumulation and release. Nature, 419(6904), 287-291.

Murray, J. R., Segall, P., Cervelli, P., Prescott, W., & Svarc, J. (2001). Inversion of GPS data for spatially variable slip-rate on the San Andreas Fault near Parkfield, CA. Geophysical research letters, 28(2), 359-362.

Neely, W. R., Borsa, A. A., & Silverii, F. (2019). GInSAR: A cGPS correction for enhanced InSAR time series. IEEE Transactions on Geoscience and Remote Sensing, 58(1), 136-146.

Nishimura, T., Hiramatsu, Y., & Ohta, Y. (2023). Episodic transient deformation revealed by the analysis of multiple GNSS networks in the Noto Peninsula, central Japan. Scientific Reports, 13(1), 8381.

Ota, Y., Chen, C. Y., & Lee, P. N. (2024). The Chaochou Active Fault in Southern Taiwan: Characteristics and Geomorphological Significance as a Reverse Fault. Journal of Structural Geology, 105191.

doi: 10.6342/NTU202500538

Pan, Y. S. (1968). Interpretation and seismic cooedination of the Bouguer gravity anomalies obtained in southtern Taiwan. Petroleum Geology of Taiwan, 5, 259-311.

Pelletier, B., & Stephan, J. F. (1986). Middle miocene deduction and late miocene beginning of collision registered in the hengchun peninsula: Geodynamic implications for the evolution of Taiwan. Tectonophysics, 125(1-3), 133-160.

Pepe, A., & Lanari, R. (2006). On the extension of the minimum cost flow algorithm for phase unwrapping of multitemporal differential SAR interferograms. IEEE Transactions on Geoscience and remote sensing, 44(9), 2374-2383.

Perfettini, H., & Avouac, J. P. (2004). Postseismic relaxation driven by brittle creep: A possible mechanism to reconcile geodetic measurements and the decay rate of aftershocks, application to the Chi-Chi earthquake, Taiwan. Journal of Geophysical Research: Solid Earth, 109(B2).

Rau, R. J., Lee, Y, H., Hu, J. C. (2010). 地震地質與地變動潛勢分析─地變動監測分析（4/4）. Central Geological Survey, Ministry of Economic Affairs, Report No. 99-10, 400 pages. (In Chinese)

Rau, R. J., Lee, J. C., Ching, K. E., Lee, Y. H., Byrne, T. B., & Chen, R. Y. (2012). Subduction-continent collision in southwestern Taiwan and the 2010 Jiashian earthquake sequence. Tectonophysics, 578, 107-116.

Raucoules, D., & De Michele, M. (2009). Assessing ionospheric influence on L-band SAR data: Implications on coseismic displacement measurements of the 2008 Sichuan earthquake. IEEE Geoscience and Remote Sensing Letters, 7(2), 286-290.

Rice, J. R., Lapusta, N., & Ranjith, K. (2001). Rate and state dependent friction and the stability of sliding between elastically deformable solids. Journal of the Mechanics and Physics of Solids, 49(9), 1865-1898.

doi: 10.6342/NTU202500538

Rosen, P. A., Hensley, S., & Chen, C. (2010, May). Measurement and mitigation of the ionosphere in L-band interferometric SAR data. In 2010 IEEE radar conference (pp. 1459-1463). IEEE.

Rosen, P. A., Gurrola, E., Sacco, G. F., & Zebker, H. (2012, April). The InSAR scientific computing environment. In EUSAR 2012; 9th European conference on synthetic aperture radar (pp. 730-733). VDE.

Rousset, B., Jolivet, R., Simons, M., Lasserre, C., Riel, B., Milillo, P., ... & Renard, F. (2016). An aseismic slip transient on the North Anatolian Fault. Geophysical Research Letters, 43(7), 3254-3262.

Scholz, C. H. (1998). Earthquakes and friction laws. Nature, 391(6662), 37-42.

Shen, S. M., Chang, J. C., Yang, G. S. (2005). 地震地質調查及活動斷層資料庫建置計畫:活動構造地形判釋及資料庫建置分析(1/2). Central Geological Survey, Ministry of Economic Affairs, Report No. 95-13, 174 pages. (In Chinese)

Shyu, J. B. H., Sieh, K., Chen, Y. G., & Liu, C. S. (2005). Neotectonic architecture of Taiwan and its implications for future large earthquakes. Journal of Geophysical Research: Solid Earth, 110(B8).

Shyu, J. B. H. (2006). A neotectonic model of Taiwan, with a focus on the Longitudinal Valley Suture (Doctoral dissertation, California Institute of Technology).

Shyu, J. B. H., Chuang, Y. R., Chen, Y. L., Lee, Y. R., & Cheng, C. T. (2016). A New On-Land Seismogenic Structure Source Database from the Taiwan Earthquake Model (TEM) Project for Seismic Hazard Analysis of Taiwan. Terrestrial, Atmospheric & Oceanic Sciences, 27(3).

Shyu, J. B. H., Yin, Y. H., Chen, C. H., Chuang, Y. R., & Liu, S. C. (2020). Updates to the on-land seismogenic structure source database by the Taiwan Earthquake Model

doi: 10.6342/NTU202500538

(TEM) project for seismic hazard analysis of Taiwan. Terr Atmos Ocean Sci, 31(4), 469.

Song, K. C., Chen, L., & Chen, Y. C. (2005). 有關旗山斷層的一些新觀察. Ti Chi, 23(3), 31-40. (In Chinese)

Sun, S. C. (1963) The reef limestones and the geologic structures in the vicinity of Kaohsiung city, Taiwan. Petroleum Geology of Taiwan, 2, 47-64.

Sun, S. C. (1964). Photogeological study of the Tainan-Kaohsiung coastal plain area, Taiwan. Petrol Geol Taiwan, 3, 39-51.

Suppe, J. (1984). Kinematics of arc-continent collision, flipping of subduction, and back-arc spreading near Taiwan. Geological Society of China Mem.

Thatcher, W. (1983). Nonlinear strain buildup and the earthquake cycle on the San Andreas fault. Journal of Geophysical Research: Solid Earth, 88(B7), 5893-5902.

Thomas, M. Y., Avouac, J. P., Champenois, J., Lee, J. C., & Kuo, L. C. (2014). Spatiotemporal evolution of seismic and aseismic slip on the Longitudinal Valley Fault, Taiwan. Journal of Geophysical Research: Solid Earth, 119(6), 5114-5139.

Titus, S. J., DeMets, C., & Tikoff, B. (2006). Thirty-five-year creep rates for the creeping segment of the San Andreas fault and the effects of the 2004 Parkfield earthquake: Constraints from alignment arrays, continuous global positioning system, and creepmeters. Bulletin of the Seismological Society of America, 96(4B), S250-S268.

Tizzani, P., Berardino, P., Casu, F., Euillades, P., Manzo, M., Ricciardi, G. P., ... & Lanari, R. (2007). Surface deformation of Long Valley caldera and Mono Basin, California, investigated with the SBAS-InSAR approach. Remote Sensing of Environment, 108(3), 277-289.

doi: 10.6342/NTU202500538

Tolomei, C., Salvi, S., Boncori, J. M., & Pezzo, G. (2015). InSAR measurement of crustal deformation transients during the earthquake preparation processes: A review. Boll. Geofis. Teor. Appl, 56, 151-166.

Torii, K. (1932a). 台南州新化油田調查報告. Bureau of Productive Industries, Government-General of Taiwan, No. 609, 29 pages. (In Japanese)

Torii, K. (1932b). 高雄州旗山油田調查報告及旗山油田地質圖（三萬分之一）. Bureau of Productive Industries, Government-General of Taiwan, No. 633, 36 pages. (In Japanese)

Tsai, M. C., Yu, S. B., Shin, T. C., Kuo, K. W., Leu, P. L., Chang, C. H., & Ho, M. Y. (2015). Velocity Field Derived from Taiwan Continuous GPS Array (2007-2013). Terrestrial, Atmospheric & Oceanic Sciences, 26(5).

Tse, S. T., & Rice, J. R. (1986). Crustal earthquake instability in relation to the depth variation of frictional slip properties. Journal of Geophysical Research: Solid Earth, 91(B9), 9452-9472.

Tsukahara, K., & Takada, Y. (2018). Aseismic fold growth in southwestern Taiwan detected by InSAR and GNSS. Earth, Planets and Space, 70, 1-7.

Tung, H. (2008). Analysis of surface deformation based on PS-InSAR technique: Case studies in coastal plain, SW Taiwan. Master's thesis, National Taiwan University, 112 pages.

Tung, C. M. (2021). Morphotectonics of the Houjing Tableland Area, Kaohsiung, Taiwan. Master's thesis, Department of Geosciences, National Taiwan University, 99 pages. (In Chinese)

Wang, K. (2007). Elastic and viscoelastic models of crustal deformation in subduction earthquake cycles. In The seismogenic zone of subduction thrust faults (pp. 540-575). Columbia University Press.

doi: 10.6342/NTU202500538

Wen, S., Hsu, H. J., Chang, W. Y., & Chen, C. H. (2012). A study of the seismogenic process beneath the south-western foothills in Taiwan in relation with the 2010 Jiasian earthquake. Tectonophysics, 570, 57-64.

Wu, Y. Y., Hu, J. C., Lin, G. P., Chang, C. P., Tung, H., & Lu, C. H. (2013). Transient active deformation in Tainan tableland using persistent scatterers SAR interferometry. Bulletin de la Société Géologique de France, 184(4-5), 441-450.

Yan, Y., Doin, M. P., Lopez-Quiroz, P., Tupin, F., Fruneau, B., Pinel, V., & Trouvé, E. (2012). Mexico City subsidence measured by InSAR time series: Joint analysis using PS and SBAS approaches. IEEE Journal of Selected Topics in Applied Earth Observations and Remote Sensing, 5(4), 1312-1326.

Yang, M., Ching, K. E., Chang-Lee, C., Chen, Y. S., & Cheng, S. C. (2015, April). Monitoring and predicting the behavior of the Lungchuan and Chishan faults with GNSS. In Proceedings of the ION 2015 Pacific PNT Meeting (pp. 536-541).

Yang, C. Y. (2024). GPS Time Series Analysis via Kalman Filter. Master's thesis, Institute of Geophysics, National Central University, 94 pages.

Yi, D. C., Chuang, R. Y., Chung, L. H., Lin, C. W., & Rau, R. J. (2023). Surface deformation induced by the 2016 Meinong earthquake and its implications to active folds. Terrestrial, Atmospheric and Oceanic Sciences, 34(1), 21.

Yoshida, K. (1932). 高雄州旗山南西部油田調查報告及旗山南西部油田地質圖（三萬分之一）. Bureau of Productive Industries, Government-General of Taiwan, 610, 162. (In Japanese)

Yu, S. B., Chen, H. Y., & Kuo, L. C. (1997). Velocity field of GPS stations in the Taiwan area. Tectonophysics, 274(1-3), 41-59.

doi: 10.6342/NTU202500538

Yu, C., Li, Z., Penna, N. T., & Crippa, P. (2018). Generic atmospheric correction model for interferometric synthetic aperture radar observations. Journal of Geophysical Research: Solid Earth, 123(10), 9202-9222.

Yunjun, Z., Fattahi, H., & Amelung, F. (2019). Small baseline InSAR time series analysis: Unwrapping error correction and noise reduction. Computers & Geosciences, 133, 104331.

Zhang, B., Zhu, W., Ding, X., Wang, C., Wu, S., & Zhang, Q. (2022). A review of methods for mitigating ionospheric artifacts in differential SAR interferometry. Geodesy and Geodynamics, 13(2), 160-169.

Zhang, K., Gan, W., Liang, S., Xiao, G., Dai, C., Liu, Z., & Zhang, L. (2024). Shallow creep on the Laohushan Segment of the Haiyuan fault, northeastern Tibetan plateau, detected with dense near-field GPS measurements. Geophysical Research Letters, 51(17), e2024GL108764.

Zhou, Y., Thomas, M. Y., Parsons, B., & Walker, R. T. (2018). Time-dependent postseismic slip following the 1978 Mw 7.3 Tabas-e-Golshan, Iran earthquake revealed by over 20 years of ESA InSAR observations. Earth and Planetary Science Letters, 483, 64-75.

Zhu, W., Zhang, W. T., He, Y. F., & Qu, W. (2017). Performance evaluation of azimuth offset method for mitigating the ionospheric effect on SAR interferometry. Journal of Sensors, 2017(1), 4587475.

doi: 10.6342/NTU202500538